Hyperons in Dense Matter

Vom Fachbereich Physik
der Technischen Universität Darmstadt

zur Erlangung des Grades
eines Doktors der Naturwissenschaften
(Dr. rer. nat.)

genehmigte Dissertation von
Dipl.-Phys. Haris Đapo
aus Trebinje, Bosnia-Herzegovinia

Darmstadt 2009
D17

Abstract

The hyperon-nucleon (YN) low momentum effective interaction ($V_{\text{low k}}$) allows for an extensive study of the behavior of hyperons in dense matter, together with an investigation of effects of the presence of hyperons on dense matter. The first step towards this goal is the construction of the matrix elements for the hyperon-nucleon low momentum potential. In contrast to the nucleon-nucleon interaction, the available experimental data for the YN interaction are scarce. As a consequence, no unique YN low-momentum potential $V_{\text{low k}}$ can be constructed from the various bare potentials. Nevertheless we can still use these low-momentum YN potentials to find out what these differences mean for the properties of dense matter.

In order to assess the different properties of hyperons within these potentials we calculate the hyperon single-particle potentials in the Hartree-Fock approximation for all of the interactions. Their dependence on both momentum and density, is studied. The single-particle potentials are then used to determine the chemical potential of hyperons in neutron stars.

For nucleonic properties, the nucleon-nucleon $V_{\text{low k}}$ can be used with the caveat that the calculation of the ground-state energy of symmetric nuclear matter does not correctly reproduce the properties of matter at saturation. Even when combined with the appropriate three-nucleon forces the results are still not satisfactory. Additionally, with the nucleon-nucleon $V_{\text{low k}}$ one is unable to reach the densities needed for the calculation of neutron star masses. To circumvent this problem we use two approaches: in the first one, we parametrize the entire nucleonic sector. In the second one, we replace only the three-body force. The former will enable us to study neutron star masses, and the latter for studying the medium's response to the external probe. In this thesis we take the external probe to be the neutrino.

By combining this parametrization with the YN $V_{\text{low k}}$ potential, we calculate the equation of state of equilibrated matter. Performing the calculation in the Hartree-Fock approximation at zero temperature, the concentrations of all particles are calculated. From these we can ascertain at which densities hyperons appear for a wide range of parameters. Finally, we calculate the masses of neutron stars with these concentrations.

For the calculation of the medium's response to an external probe, we replace the three-body force with a density-dependent interaction. This density-dependent interaction is fitted to the saturation properties of nuclear matter and

used together with the $V_{\text{low k}}$ potential. The study of in-medium properties with these interactions is accomplished with a combination of Fermi liquid theory and random phase approximation(RPA). The Fermi liquid theory is then used to obtain the strength of the particle-hole interactions. The medium's response to neutrinos is represented via changes of the polarization function in the random phase approximation.

The properties of neutrinos in dense matter are studied in both, Hartree-Fock and random phase, approximation. To understand how the changes in the mediums response alter the behavior of neutrinos in dense matter, we calculate the neutrino cross section and the neutrino mean free path. The neutrinos interact with baryons and leptons through the weak interaction, hence we calculate these for both neutral and charged currents. The comparison between the Hartree-Fock approximation and RPA plays a central role in this work.

Zusammenfassung

Eine effektive Hyperon-Nukleon-(YN)-Wechselwirkung im Bereich kleiner Impulse, bekannt als $V_{\text{low-k}}$, ermöglicht eine ausgiebige Studie des Hyperon-Verhaltens in dichter Materie, sowie der Auswirkungen, die die Präsenz der Hyperonen auf die Eigenschaften dichter Materie hat. Dazu ist es zunächst notwendig, die Matrixelemente der effektiven Hyperon-Nukleon-Wechselwirkung zu konstruieren. Im Gegensatz zur Nukleon-Nukleon-Wechselwirkung ist die YN-Wechselwirkung durch die geringen experimentellen Daten kaum eingeschränkt, so dass selbst mit Hilfe des Renormierungsgruppenzugangs von $V_{\text{low-k}}$ keine universelle Wechselwirkung aus den verschiedenen 'nackten' an die Streudaten angepassten YN-Potentialen extrahiert werden kann. Trotzdem lohnt sich ein Vergleich der Vorhersagen der unterschiedlichen effektiven Wechselwirkungen zu den Eigenschaften dichter Materie.

Um die Eigenschaften der Hyperonen für die verschiedenen Wechselwirkungen zu studieren, berechnen wir die Hyperon-Einteilchenpotentiale im Rahmen der Hartree-Fock-Näherung und untersuchen ihre Impuls- und Dichteabhängigkeiten. Anhand der Einteilchenpotentiale kann anschließend das chemische Potential der Hyperonen in einem Neutronenstern ermittelt werden.

Da die Rechnungen stark vom Nukleonen-Sektor beeinflusst werden, muss auch für nukleonische Wechselwirkung eine angemessene Wahl getroffen werden. In diesem Zusammenhang liefert das universelle Nukleon-Nukleon-$V_{\text{low-k}}$ unglücklicherweise kein physikalisch sinnvolles Sättigungverhalten für Kernmaterie. Selbst bei zusätzlicher Verwendung einer Drei-Nukleon-Wechselwirkung werden die Saturationseigenschaften der Kernmaterie nicht völlig korrekt beschrieben. Ein weiteres Problem besteht darin, dass $V_{\text{low-k}}$ per Konstruktion nicht bei den hohen Dichten angewandt werden kann, welche zur Berechnung der Massen von Neutronensternen erforderlich sind. Als Alternativen verwenden wir daher zwei Ansätze: eine angepasste Parametrisierung des gesamten nukleonischen Sektors, bzw. eine Anpassung der Parameter der $3N$-Wechselwirkung. Der erstgenannte Zugang erlaubt die Untersuchung von Neutronenstern-Massen, während die zweite Methode zur Untersuchung der Antwort des Mediums auf externe Sonden — in unserem Fall Neutrinos — verwendet werden kann.

Die vollständige Parametrisierung der nukleonischen Wechselwirkung wird zusammen mit den $YN - V_{\text{low-k}}$ zur Berechnung der Zustandsgleichung von Materie im Gleichgewicht verwendet. Die Rechnungen werden in der Hartree-Fock-Näherung bei verschwindender Temperatur ausgeführt. Als Ergebnis erhalten wir

die Konzentrationen der verschiedenen Teilchenspezies und können bestimmen, bei welchen Dichten Hyperonen auftreten. Die ermittelten Konzentrationen werden anschließend zur Berechnugn der Neutronenstern-Masse eingesetzt.

Zur Untersuchung der Antwort des Mediums auf externe Sonden verwenden wir eine NN-Wechselwirkung zusammen mit einer angepassten dichteabhägigen Näherung für die $3N$-Wechselwirkung. Als Hyperon-Nukleon-Wechselwirkung kommt wiederum das $YN - V_{\text{low-k}}$ zum Einsatz. Auf dieser Grundlage berechnen wir die In-Medium-Eigenschaften mit Hilfe einer Kombination aus Fermi-Liquid-Theorie und Random Phase Approximation (RPA). Die Fermi-Liquid-Theorie liefert die Stärke der Teilchen-Loch-Wechselwirkungen, während sich die Antwort des Mediums auf Neutrinos anhand von Änderungen der Polarisationsfunktion in der RPA bemerkbar macht.

Die Neutrino-Eigenschaften in dichter Materie werden sowohl in der Hartree-Fock-Näherung als auch der RPA studiert. Um zu verstehen, wie sich Änderungen des Mediums auf das Verhalten der Neutrinos auswirken, berechnen wir Wirkungsquerschnitte und mittlere freie Weglänge. Da Neutrinos mit Baryonen und Leptonen schwach wechselwirken, betrachten wir in unseren Rechnungen sowohl den neutralen als auch den geladenen Strom. Der Vergleich von Hartree-Fock-Näherung und RPA nimmt eine zentrale Rolle bei der Untersuchung ein.

Contents

Introduction

The core collapse supernovae are some of the most spectacular events in the Universe. These events have been studied for more than three decades mainly through numerical simulations. Despite the huge amount of physics involved and great uncertainties, a kind of "standard model" exists: the inner iron core of a massive star overcomes its hydrodynamical stability limit (the Chandrasekhar mass) and collapses, increasing the density inside up to many times nuclear saturation density; the stiffness of nuclear matter then results in an elastic bounce of the core, creating a shock-wave. This wave propagates through the star, while losing energy by the dissociation of nuclei and production of neutrinos. If this wave had enough energy to reach the star's surface and to cause an explosion one would refer to this as a "prompt" explosion mechanism. Unfortunately in simulations this wave stalls at ~ 200 km and does not lead to an explosion.

In addition to the neutrinos produced by the shock-wave there is also a copious amount of neutrinos produced deeper in the star behind the shock-wave front. These neutrinos are initially trapped in this proto-neutron star because their mean free path is smaller than the radius of the proto-neutron star. This is a unique situation for neutrinos as they are usually free to leave the system in which they are created without obstacle due to their very weak interaction with all forms of matter.

Modern-day simulations of core collapse supernovae rely on these neutrinos for a successful explosion. Once the neutrinos are no longer trapped they start to stream out of the proto-neutron star in enormous quantities. Even if only a tiny fraction of them deposits some of their energy in the shock-wave, this could be sufficient to revive the shock-wave and enable it to reach the surface of the star, thus causing an explosion. Such a mechanism of explosion is then referred to as "delayed" because of the time lapse between the start of the shock-wave and the time at which neutrinos cease to be trapped. For recent reviews of core collapse supernova simulations see [1, 2] and references therein.

This makes the properties of neutrino interactions in hot and dense matter a fundamental part of understanding supernova events. It is important both to understand how neutrinos behave inside a proto-neutron star as well as how effectively they transfer their energy to the shock-wave. In order to have an answer

to these questions one should thus determine what are the neutrino cross section and mean free path in such dense environments.

Of particular interest, from a nuclear physics point of view, is the behavior of neutrinos at densities above the saturation density of nuclear matter. It is obvious, if one considers the scales involved, that the strong interaction will play an important role in this case since the properties of baryons are changed when they are in-medium. These in-medium modifications can be studied with mean-field or Fermi liquid theories and the random-phase approximation (RPA) [3, 4, 5]; in this thesis we will use a combination of Fermi liquid theories and RPA. In addition to the description of neutrino transport properties, numerical simulations of the supernova evolution require knowledge of the equation of state of dense matter. These two aspects of nuclear physics play an important role in understanding the physics of the core collapse supernova.

Another intriguing aspect of dense matter is then the influence of more exotic forms of matter, other than nucleons. Among such exotica, which one expects to appear at such high densities, are the hyperons. Other possibilities include pion and kaon condensates, superfluidity, and also quarks, cf. [6]. Since hyperons are the lightest baryons after nucleons they are considered as prime candidates for appearance in neutron stars. It is expected that they appear at around twice the nuclear saturation density and form sizable concentrations in the inner core of neutron stars. Once they appear, hyperons introduce a host of new possible processes between them and the neutrinos in addition to the ones which already exist between neutrinos and nucleons. These new processes can play a significant role in the neutrino cross section because some of the nucleonic processes might be forbidden due to Pauli blocking.

In order to understand how hyperons, and strangeness in general, behaves in dense matter, the understanding of the hyperon-nucleon (YN) interaction is essential. Unfortunately, the details of the YN interaction are determined very poorly by experiment and there are several different potentials available. This then poses a challenge to see what results these different potentials give. Our approach to this is the construction of an effective low momentum interaction known as $V_{\text{low k}}$ from these different potentials. In this case $V_{\text{low k}}$ offers a unique possibility to study all of these potentials since it is relatively easy to perform a Hartree-Fock calculation with them. This then allows for an extensive comparison of the different results involving these interactions as well as for a robust study of all possibilities that can arise.

The formalism of the Fermi liquid theory in combination with RPA can be easily extended to the case of hyperons. With this extension we will include hyperons into the medium's response to the neutrino probe. Such derived cross sections and mean free paths will then tell us how the presence of hyperons in the medium alters the medium's response compared to the response of pure nuclear

matter.

Additionally, the baryonic equation of state (EoS) is the fundamental input for the calculation of neutron star properties. It is particularly important to know how the EoS behaves at densities above saturation density since this will play the most important role in determining the maximum allowed mass of a neutron star. At about twice the saturation density one expects strange baryons to appear as new hadronic degrees of freedom. Unfortunately the nucleon-nucleon (NN) $V_{\text{low k}}$ is not well suited for the study of neutron star masses. The reason for this lies in the introduction of a scale that separates the low and high momenta. This scale imposes a limit on the densities which can be studied with NN $V_{\text{low k}}$ and these are too low for the study of neutron star masses. However YN $V_{\text{low k}}$, thanks to the higher masses and lower concentrations of hyperons, can reach the densities of interest in neutrons stars. Hence we will replace the nucleonic part of the EoS with a parameterization and use it in combination with YN $V_{\text{low k}}$ to study the masses of neutron stars.

It is interesting to point out that many of the features mentioned in connection with neutrinos coming from neutron stars can be measured practically any given day, with a bit of luck. Should an occurrence similar to that of the supernova explosion SN1987A repeat itself, present day detectors would collect a sizable amount of data. It is not unreasonable to assume this will happen in the near future as it is known from galaxy surveys that on average there are $3-4$ supernova per 100 years in galaxies similar to our own. Even back in 1987 enough data was collected to discern some of the properties of supernova neutrinos. Today, after three decades of building ever larger neutrino detectors, a supernova explosion in our galaxy would provide enough information to discriminate between many model predictions.

The structure of this thesis is as follows. Chapter 1 is devoted to the construction of the low momentum effective hyperon-nucleon interactions and the discussion of the resulting matrix elements. We also show and discuss some of the low-energy observables directly calculated from the interaction.

In chapter 2 we introduce the concept of infinite nuclear matter and use it in combination with a Hartree-Fock approximation to calculate the ground-state energy. To achieve this goal we define and investigate the single-particle potential. This will enable us to describe the in-medium properties of baryons. The failure to reproduce the properties of nuclear matter by pure two-body forces leads to the introduction of three-body forces.

Chapter 3 discusses the equation of state for equilibrated matter. In this context we use the parametrization of the nucleonic part of equation of state to investigate the influence of changes in parameters on the hyperon sector. We conclude this chapter by calculating the properties of neutron stars with hyperons.

Properties of particle-hole excitations are examined in chapter 4. There we

use the Landau Fermi liquid theory in order to calculate the Landau-Migdal parameters. In this chapter we also introduce the density-dependent force aimed at replacing the three-body force which did not produce the correct values for saturation density.

Chapter 5 is devoted to the calculation of neutrino properties in dense matter. Results for the cross section and mean free path in symmetric and equilibrated matter are shown.

In chapter 6 we summarize the results and offer an outlook of possible extensions of this work.

The appendices are devoted to the details of the expressions used. In Appendix A we explain the details of the construction of the $V_{\text{low k}}$ potential, including the transition from the plane-wave basis to the partial-wave basis. In Appendix B we present the calculation of the Hartree-Fock ground-state energy in infinite nuclear matter. Neutrino cross sections are calculated in Appendix C. Additionally, we use Appendix C to show the calculation of the RPA polarization matrix in the medium containing both nucleons and hyperons.

1 Hyperon-Nucleon interaction

One of the greatest issues of nuclear theory is that from a numerical point of view the bare nuclear forces are ill behaved. This comes from the inability of many-body techniques to treat in a straightforward way the hard-core that bare nuclear potentials have. This hard core is too strong to be treated perturbatively and makes a direct self-consistent approach impossible. However the nucleon in nuclei or nuclear matter do not feel this bare interaction but an effective interaction which arises when one considers all many-body effects present. This effective interaction is much better behaved and allows for the application of standard many-body methods.

One such effective interaction which has appeared recently is the $V_{\text{low k}}$ [7]. By requirement of phase shift equivalence $V_{\text{low k}}$ creates, from several different starting potentials, a practically unique NN interaction. This gives the impression of universality of the effective interactions.

We extend this idea of constructing an effective potential to the case of the hyperon-nucleon (YN) interaction. The motivation is twofold: if the NN $V_{\text{low k}}$ is so universal then so should the YN $V_{\text{low k}}$ be and the standard many-body methods can then be applied to the YN interaction. Unfortunately, there exist only a very limited amount of scattering and phase shift data for the case of the YN. This data is not sufficient to uniquely constrain the YN potentials. Thus different bare potentials, for the YN $V_{\text{low k}}$ construction, exhibit different phase shift results. It is then not unexpected that at present it is not possible to construct a unique YN low-momentum effective interaction.

However forthcoming experiments at the planned J-PARC and FAIR facilities are expected to add new data to the existing ones. This would then allow for a better treatment of the YN interaction. Additionally, first lattice QCD simulations of the YN interaction have been performed [8]. This, combined with the motivation to use many-body methods, has inspired us to develop the YN $V_{\text{low k}}$ in spite of the large uncertainties present today. Because once there is sufficient data to construct a high-quality YN potential the method for constructing the $V_{\text{low k}}$ from it will be readily available. This thesis is thus mainly devoted to the construction and comparison of various $V_{\text{low k}}$ YN interactions in the dense environment found in neutron stars.

The outline of this chapter is as follows. The NN low-momentum effective interaction is presented in Sec. 1.1 as an introduction for the construction of the YN $V_{\mathrm{low\ k}}$ which is done in Sec. 1.1.1. Sec. 1.1.2 discuses the bare potentials used while Sec. 1.1.3 presents the results of the matrix elements of the YN $V_{\mathrm{low\ k}}$ in several partial wave channels. In Sec. 1.2 we show some of the low-energy observables directly calculated from the matrix elements of the potentials.

1.1   Low-momentum interaction

$V_{\mathrm{low\ k}}$ is supposed to represent a "universal" low-momentum effective interaction. It is derived by performing the renormalization group(RG) decimation starting from a "bare" interaction. In the case of the nucleon-nucleon(NN) interaction, as shown in [9], this is indeed the case. This agreement is shown in Fig. 1.1. By using several different modern NN interactions a low momentum interaction was constructed and the agreement is obvious. For all partial waves the resulting $V_{\mathrm{low\ k}}$ potentials show excellent agreement.
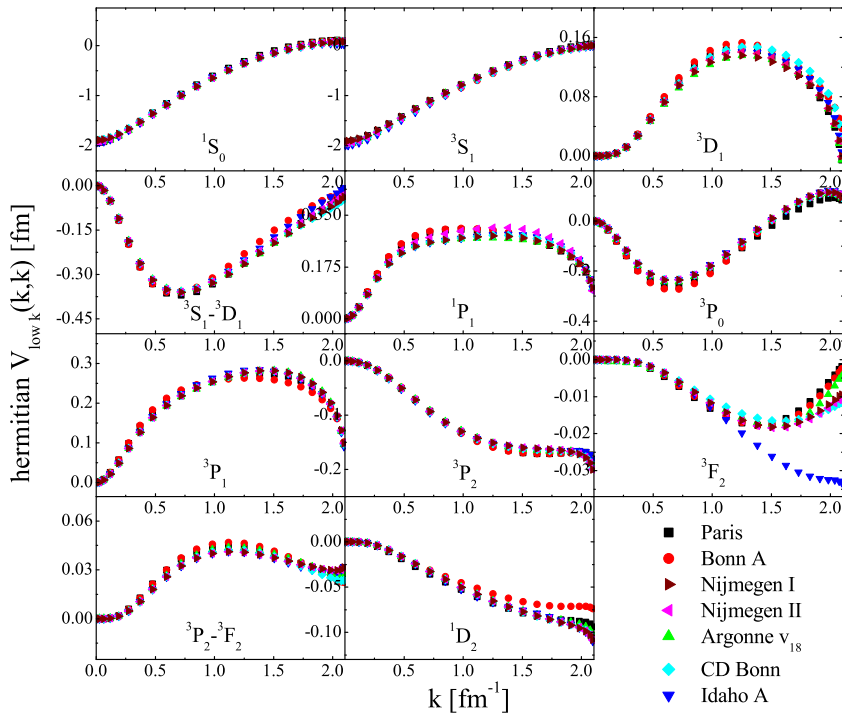

Figure 1.1: Diagonal momentum-space matrix elements of the hermitian $V_{\mathrm{low\ k}}$ obtained from the different potential models for a cut-off $\Lambda = 2.1\,\mathrm{fm}^{-1}$. Results are shown for the partial waves $J < 2$ [9].

The basic idea behind the $V_{\text{low k}}$ is that the short-range physics which is represented by a hard core can be integrated out. The advantage is twofold. Firstly, since this part of the interaction is not well constrained by phase shifts, removing it will reduce the uncertainty. Secondly, any effect that the hard core has on long-range (low-momentum) physics will be preserved. A further advantage is that once created, such an interaction simplifies many nuclear structure calculations by virtue of the significantly smaller momentum range that needs to be taken into account.

In this chapter we generalize the construction of the $V_{\text{low k}}$ to the YN interaction. Ideally such a potential would retain all of the advantages which the NN $V_{\text{low k}}$ has. As we shall show, however, while the short range effects and the simplification remain as bonuses, the "universality" of the YN $V_{\text{low k}}$ simply does not exist. The reasons for this lack of agreement between various YN $V_{\text{low k}}$ potentials shall be discussed in detail later.

1.1.1 Construction of $V_{\text{low k}}$

The starting point for the construction of the $V_{\text{low k}}$ is the half-on-shell T-matrix, $T(q', q; q^2)$, which is determined by the nonrelativistic Lippmann-Schwinger equation Eq. (A.6) in momentum space. The on-shell energy is denoted by q^2 and q', where q are the relative momenta between a hyperon and a nucleon. An effective low-momentum $T_{\text{low k}}$-matrix is then obtained by introducing a cut-off Λ in the Lippmann-Schwinger kernel, thus integrating the intermediate state momenta up to this cut-off. At the same time, the bare potential in the coupled-channel partial wave Lippmann-Schwinger equation is replaced with the corresponding low-momentum potential $V_{\text{low k}}$. Thus from the usual Lippmann-Schwinger equation Eq. (A.22) we get:

$$T_{\text{low }k,y'y}^{\alpha'\alpha}(q', q; q^2) = V_{\text{low }k,y'y}^{\alpha'\alpha}(q', q) +$$

$$\frac{2}{\pi} \sum_{\beta,z} P \int_0^{\Lambda} dl\, l^2 \frac{V_{\text{low }k,y'z}^{\alpha'\beta}(q', l) T_{\text{low }k,zy}^{\beta\alpha}(l, q; q^2)}{E_y(q) - E_z(l)} . \tag{1.1}$$

The effective low-momentum $V_{\text{low k}}$ is then defined by the requirement that the T-matrices are equivalent for all momenta below this cut-off

$$T^{\alpha'\alpha}(q', q; q^2) = T_{\text{low }k}^{\alpha'\alpha}(q', q; q^2), \qquad q', q \leq \Lambda . \tag{1.2}$$

Thus the obtained $V_{\text{low k}}$ is non-hermitian, nevertheless a phase-shift equivalent hermitian low-momentum YN interactions can be obtained. Since the low-momentum T-matrix $T_{\text{low k}}$ must be cut-off-independent, i.e. $dT_{\text{low k}}/d\Lambda = 0$, an

RG flow equation for the $V_{\text{low k}}$ can immediately be derived:

$$\frac{dV_{\text{low k}}\,(k',k)}{d\Lambda} = \frac{2}{\pi}\frac{V_{\text{low k}}\,(k',\Lambda)T(\Lambda,k;\Lambda^2)}{1 - k^2/\Lambda^2}\,. \qquad (1.3)$$

Instead of solving this flow equation with standard numerical methods (e.g. Runge-Kutta) directly, the so-called ALS iteration method, pioneered by Andreozzi, Lee and Suzuki, is used [10, 11, 12]. This iteration method is based on a similarity transformation and its solution corresponds to solving the flow equation. Details about the convergence of the ALS iteration method, applied to the coupled channel YN interaction, can be found in [13, 14]. For the hyperon-nucleon interaction with strangeness $S = -1$ two different bases, the isospin and the particle basis of the bare potentials, are available.

While in the NN case the only coupling which appears is that of angular momentum arising due to the tensor force, in the YN case we have a more complicated situation. One difference is that there exists a singlet-triplet coupling between different spin states Eq. (A.24). However, this is practically identical to the tensor couplings. So the increase in complexity is not significant. A much bigger difference arises when we consider the isospin space. In the case of the construction of the YN $V_{\text{low k}}$ there is an additional level of complexity, as compared to the NN case, because now we have a coupling which we did not encounter in the NN case. Eq. (A.25) describes the situation if we consider all particles separately. This is the particle basis which we use. The biggest consequence of this difference is that when searching for the solution of the Lippmann-Schwinger equation Eq. (1.1) we have to keep in mind that this entire matrix has to be on-shell.

1.1.2 Bare potentials

In order to solve the flow equation Eq.(1.3) a bare potential as initial condition for the flow must be chosen. In this work several initial YN potentials, the original Nijmegen soft core model NSC89 [15], the series of models NSC97a-f [16] also by the Nijmegen group and a recent model proposed by the Jülich group [17], labeled as J04 in the following, are used. All above mentioned models are formulated in the conventional meson-exchange (OBE) framework. They involve a set of parameters which have to be determined from the available scattering data. These are the coupling constants of the corresponding baryon-baryon-meson vertices and cut-off parameters for the vertex form factors. Due to the limited YN scattering data these parameters cannot be precisely fixed as opposed to the NN interaction where a lot of scattering data is available. In order to consistently construct conventional OBE models for the YN interaction, one usually assumes flavor $SU(3)$ constraints or G-parity arguments on the coupling constants, and

in some cases even the $SU(6)$ symmetry of the quark model and adjusts their size by fits to NN data. The major conceptual difference between the various conventional OBE models consists in the treatment of the scalar-meson sector, which plays an important role in any baryon-baryon interaction at intermediate ranges. In contrast to the pseudoscalar and vector meson sectors, it is still an open issue which are the actual members of the lowest lying scalar-meson $SU(3)$ multiplet, what are the masses of the exchange particles and how, if at all, the relations for the coupling constant, obtained by $SU(3)$ flavor symmetry, should be applied. For example, in the older versions of the YN models by the Jülich group [18, 19] a fictitious σ meson with a mass of roughly 550 MeV arising from correlated $\pi\pi$ exchange was introduced. The coupling strength of this meson to the baryons was treated as a free parameter and finally fitted to the rare data. However, in the novel Jülich YN potential [17] a microscopic model of the correlated $\pi\pi$ and $K\bar{K}$ exchange is established in order to fix the contributions in the scalar σ- and vector ρ-channel. This new model incorporates also the common one-boson exchange parts of the lowest pseudoscalar and vector meson multiplets. The corresponding coupling constants are determined by $SU(3)$ flavor symmetry and the so-called $F/(F+D)$ ratios are fixed to the pseudoscalar and vector meson multiplets by invoking $SU(6)$ symmetry.

In the Nijmegen YN models, NSC89 [15], NSC97 [16] and in the recently extended soft core model for strangeness $S = -2$ ESC04 [20, 21] this interaction is generated by a genuine scalar $SU(3)$ nonet meson exchange. Besides this scalar meson nonet two additional nonets, the pseudoscalar and vector $SU(3)$ flavor nonets, are considered in all Nijmegen models. Additionally, the Pomeron exchange is also included which provides an additional short-range repulsion. Nevertheless, there are a few conceptual differences in the various mentioned models. In the NSC97 models the strength parameter for the spin-spin interaction, the magnetic $F/(F+D)$ ratio is left as an open parameter and takes six different values in a range of 0.4447 to 0.3647 for the six different models NSC97a-f. In the original Nijmegen SC89 model this parameter is constrained by weak decay data. Furthermore, the NSC97 models include additional $SU(3)$ flavor breaking which is based on the so-called ${}^3\text{P}_0$ model [22].

The predictions of the above mentioned models are compared with another approach, the so-called chiral effective field theory (χEFT) of nuclear interactions which is based on chiral perturbation theory. For recent reviews see e.g. [23, 24, 25]. The major benefit of the χEFT is the underlying power counting scheme, proposed by Weinberg [26, 27], that allows one to improve the calculations systematically by going to higher orders in the expansion. Additionally, higher two- and three-body forces can be derived consistently in this framework. Furthermore, the effective potential is explicitly energy-independent in contrast to the original Weinberg scheme.

Within χEFT the NN interaction has been analyzed recently to a high precision (N³LO) [28]. To leading order (LO) the NN potential is composed of pion exchanges and a series of contact interactions with an increasing number of derivatives which parameterize the singular short-range part of the NN force. In order to remove the high-energy components of the baryonic and pseudoscalar meson fields a cut-off Λ dependent regulator function in the Lippmann-Schwinger (LS) equation is introduced. Then with this regularized LS equation observable quantities can be calculated. The cut-off range is restricted from below by the mass of the pseudoscalar exchange mesons. Note that in conventional meson-exchange models the LS equation is not regularized and convergence is achieved by introducing form factors with corresponding cut-off masses for each meson-baryon-baryon vertex.

So far, the YN interaction has not been investigated in the context of the χEFT as extensively as the NN interaction. A recent application to the YN interaction by the Jülich group can be found e.g. in [29]. Analogous to the NN case, the YN potential, obtained in LO χEFT , consists of four-baryon contact terms and pseudoscalar meson (Goldstone boson) exchanges which are all related by $SU(3)_f$ symmetry. For the YN interaction typical values for the cut-off lie in the range between 550 and 700 MeV (see e.g. [28]). At LO χEFT and for a fixed cut-off Λ and pseudoscalar $F/(F + D)$ ratio there are five free parameters. The remaining interaction in the other YN channels are then determined by $SU(3)_f$ symmetry. A next-to-leading order (NLO) χEFT analysis of the YN scattering and of the hyperon mass shifts in nuclear matter was performed in [30]. However, in this analysis the pseudoscalar meson exchange contributions were not taken into account explicitly but the YN scattering data could be described successfully for laboratory momenta below 200 MeV using 12 free parameters. One ambiguity in this approach for the YN interaction is the value of the η coupling which is identified with the octet η_8 meson coupling and not with the physical η meson. The influence of this ambiguity on the data description can be disregarded [31].

Since data on YN scattering is scarce, it has not been possible yet to determine uniquely the spin structure of the YN interaction. Nevertheless, all of the above mentioned OBE models are consistent with the measured YN scattering observables. Additionally, all of these potentials include the $\Lambda N - \Sigma N$ conversion process.

1.1.3   Results of the potential

Here we will present the result of the construction of the $V_{\text{low k}}$. The hyperon nucleon scattering of the form, $Y + N \rightarrow Y' + N'$, will be shown in the partial wave basis for several of the most dominant and representative cases. In general we have used the Lippman-Schwinger equation to construct waves up to $L = 5$,

but as can be seen in the following figures the S-wave is the most dominant one and already the D-wave is almost an order of magnitude weaker.

For all cases shown here we have used the cut-off $\Lambda = 500$ MeV. We have chosen this particular cut-off, because it is expected that the $V_{\text{low k}}$ is only weakly dependent on the cut-off in the range from ~ 200 MeV to ~ 600 MeV. Essentially at this value the short range (high momentum) effects have already been integrated out while at the same time the pion contribution remains largely unchanged in this interval.

In all figures of the potential we show both, the bare potential and the resulting $V_{\text{low k}}$ potential. The bare potentials are shown with points while the $V_{\text{low k}}$ are indicated by lines.
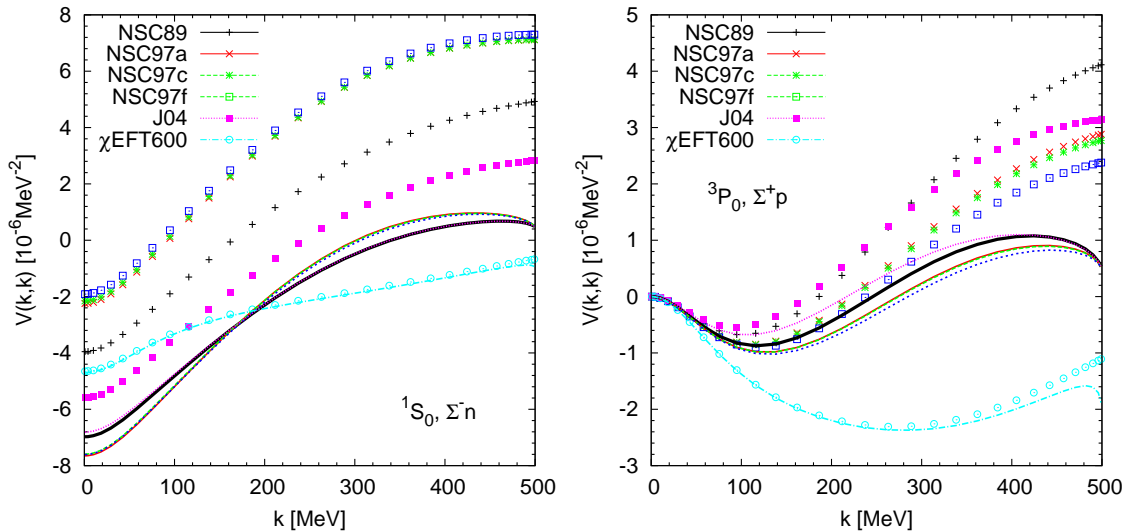

Figure 1.2: Bare and $V_{\text{low k}}$ potentials for $^1S_0, \Sigma^- n$ (left) and $^3P_0, \Sigma^+ p$ (right).

Fig. 1.2 shows the bare and $V_{\text{low k}}$ potentials for the $^1S_0, \Sigma^- n$ channel on the left hand side and the $^3P_0, \Sigma^+ p$ channel on the right-hand side. The potentials for the $V_{\Sigma^- n \Sigma^- n}$ and $V_{\Sigma^+ p \Sigma^+ p}$ are almost the same in all partial wave channels, the only small difference comes from the different reduced masses of these systems. As one can see, most of the $V_{\text{low k}}$ potentials are the same in these channels showing that $V_{\text{low k}}$ can produce a unique potential for the hyperons. This implies that the ambiguous situation which we will meet later on in the other channels is not the failing of the $V_{\text{low k}}$ method. Essentially as soon as there are enough constraints on the phase shifts, $V_{\text{low k}}$ works well in calculating the correct low-momentum potential.

The only exception to the good behavior of this channel is the χEFT600 which

by itself is not a realistic potential but a theoretically constructed potential. As a result, information regarding phase shifts cannot be used as directly as for the other potentials. Thus for the χEFT600, though some degree of improvement can be made on the theoretical side, ultimately it is also fitted, so increased data quality would bring improvements. However since χEFT is also a low-momentum potential, applying the $V_{\text{low k}}$ does not change it by much. This can be observed in Fig. 1.2. The points of the bare χEFT600 and the lines of the $V_{\text{low k}}$ are seen to be very close. A very simple explanation for this is that the cut-off of the χEFT is 600 MeV while the cut-off of the $V_{\text{low k}}$ is 500 MeV so there are not so many "high" momentum effects which can be transferred to the low momenta in the RG decimation procedure.
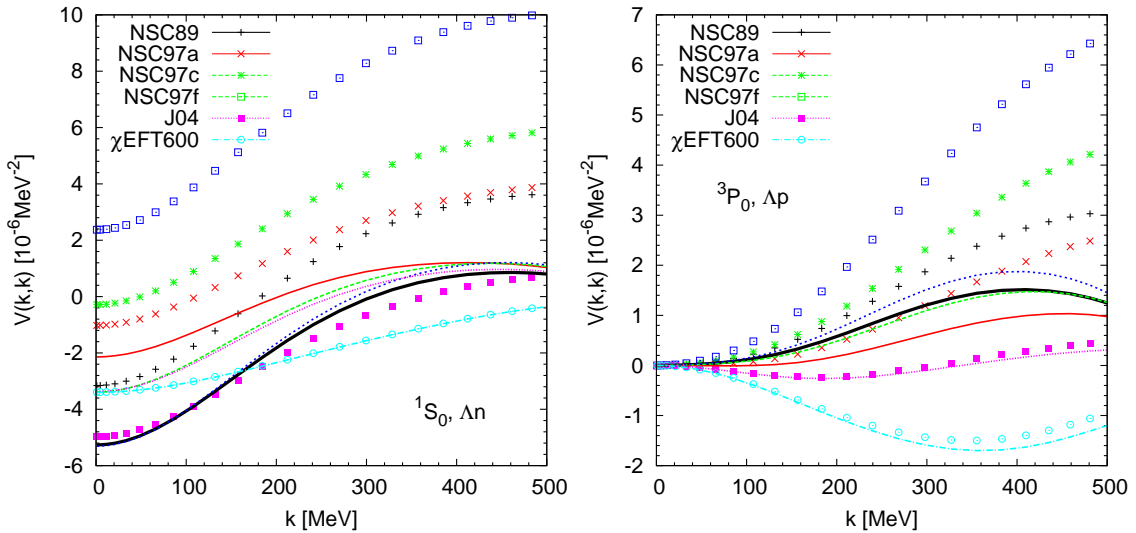
Figure 1.3: Bare and $V_{\text{low k}}$ potentials for $^1S_0, \Lambda n$ (left) and $^3P_0, \Lambda p$ (right).

Fig. 1.2 also shows that in both channels the $V_{\text{low k}}$ is more attractive than the corresponding bare potential. This serves to show that in the bare potential some of the attraction would be provided by the momentum states above the $V_{\text{low k}}$ cut-off. It should also be said that these two figures show the simplest channel in the YN sector since there is no coupling to any other channel. In general this would not be the case since most channels are coupled, either in the isospin space or in the angular momentum space.

In Fig. 1.3 we show the bare and $V_{\text{low k}}$ potentials for the $^1S_0, \Lambda n$ channel on the left-hand side and the $^3P_0, \Lambda p$ channel on the right-hand side. As can be seen here, the resulting $V_{\text{low k}}$ do not show agreement with one another, although the differences are not as large as for the bare potentials. As mentioned before this is

because of the lack of data on phase shifts with which one could construct a high quality YN potential. In this case as well, isospin symmetry gives us a practically identical potential for Λp and Λn for all partial waves.

Figure 1.4: Bare and $V_{\text{low k}}$ potentials for $^1S_0, \Sigma^- p$ (left) and $^3D_1, \Sigma^0 n$ (right).

These channels are coupled in the isospin, but not in the angular momentum space. What is interesting to note is that since this is a coupled channel, greater attraction which we can observe in the case of the $V_{\text{low k}}$ compared to the bare potentials, can also come from the off diagonal elements such as the $V_{\Lambda p \Sigma^+ n}$. This gives us a much more complicated situation to interpret, since the statement that changes in the $V_{\text{low k}}$ of the $V_{\Lambda p \Lambda p}$ come only from higher momentum contributions in this channel is no longer true. Most obviously for the NSC97f, this complex connection between the diagonal and non-diagonal elements for the $^1S_0, \Lambda n$ channel will give rise to an attractive $V_{\text{low k}}$ potential from a repulsive bare potential.

Fig. 1.4 shows the bare and $V_{\text{low k}}$ potentials for the $^1S_0, \Sigma^- p$ channel on the left-hand side and the $^3P_0, \Sigma^0 n$ channel on the right-hand side. In this channel we have both coupling of the isospin as well as coupling of the angular momentum. We can see that the cut-off effects are more pronounced here than they are in the other channels. One interesting feature of the $^3D_1$ channel is the non-zero value for the $J04$ and χEFT600 potentials at zero momentum. This can be interpreted as the presence of a bound state in these potentials in this channel which is not present in the other channels. The repulsion of the $^3S_1$ channel which can be seen for χEFT600, whereas the other potentials are attractive, will later lead to a profound difference in the value of the Σ single-particle potential.
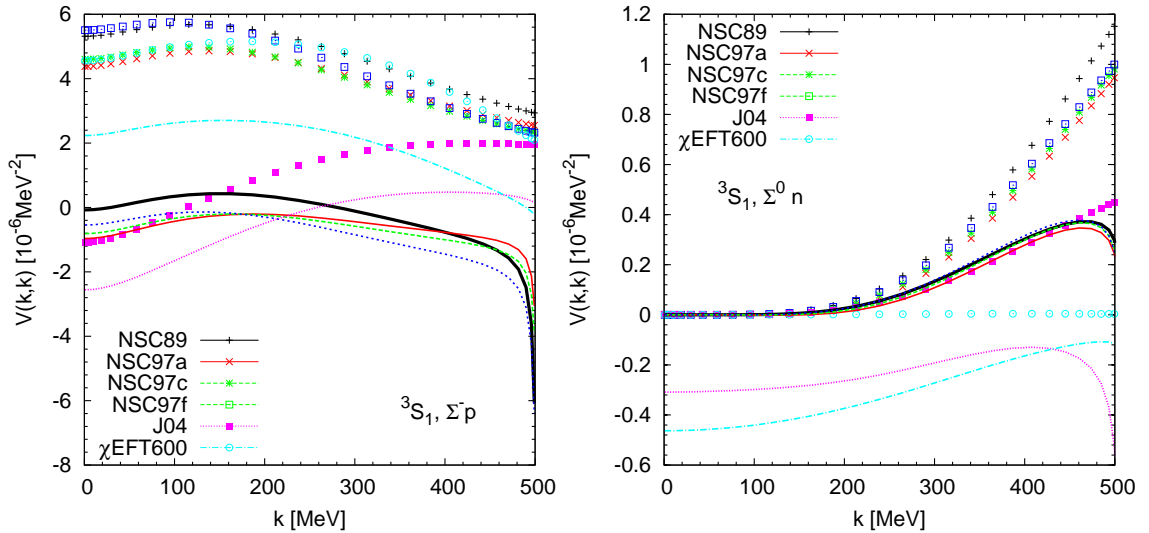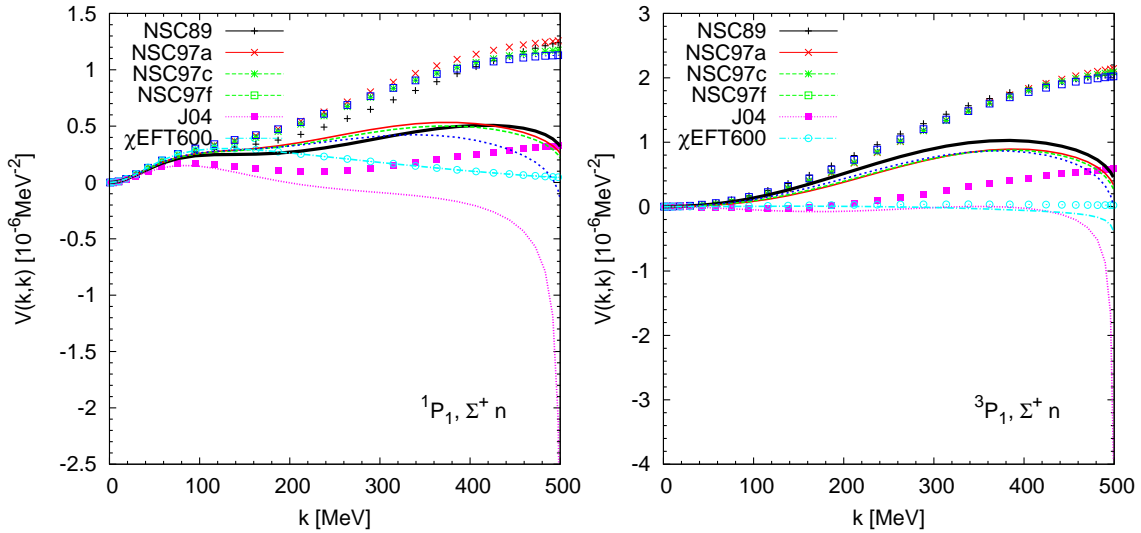
Figure 1.5: Bare and $V_{\text{low k}}$ potentials for $^1P_1, \Sigma^+ n$ (left) and $^3P_1, \Sigma^0 p$ (right).

Fig. 1.5 shows the bare and $V_{\text{low k}}$ potentials for the $^1P_1, \Sigma^+ n$ channel on the left-hand side and the $^3P_1, \Sigma^0 p$ channel on the right-hand side. Like the previous case this is a fully coupled case, but now in addition to the isospin coupling we have a spin coupling. This channel is than particularly interesting because such a coupling cannot exist in the nucleon-nucleon case. What we notice here in this partial wave, and which forms a trend that applies also to the higher waves, is that the differences between the bare potential and the $V_{\text{low k}}$ potential are smaller compared to the S-wave. This is understandable because relative to the S-waves, these waves will have a smaller magnitude. So there will be less effects at higher momentum which would lead to differences between bare and $V_{\text{low k}}$ potentials due to RG decimation.

Overall these results show how the construction of the $V_{\text{low k}}$ changes the YN potential compared to the bare case on producing an effective low-momentum potential. The results themselves are only as good as the starting bare potentials and they are heavily dependant on the quality and quantity of phase shift data available for their construction. The few cases where we see agreement between different models show that given a high-quality potential, the $V_{\text{low k}}$ procedure could produce the same uniqueness of the potential in the YN sector as in the NN sector. Unfortunately, with the situation being what it is, we will have to contend with the disagreement between models throughout this work.

1.2 Low-energy observables

In order to obtain further insight into the separation of scales for the evolution of the low-momentum $V_{\text{low k}}$ we investigate its cut-off dependence. A common feature of all YN potentials is the long-range one-pion exchange (OPE) tail. In general, the RG decimation eliminates the short-distance part of the bare potential and preserves the model-independent impact of the high-momentum components on low-momentum observables. In this sense, the ambiguities associated with the unresolved short-distance parts of the interaction disappear and a universal low-momentum YN interaction $V_{\text{low k}}$ can be constructed from phase shift equivalent bare YN potentials.

The mentioned hierarchy of scales can be seen e.g. in the $\Sigma^- n$ channel, see Fig. 1.6. The $V_{\text{low k}}$ matrix elements for vanishing momenta are shown as functions of the cut-off Λ for the $^1S_0$ partial wave. When Λ is decreased, the resulting $V_{\text{low k}}$ becomes more and more attractive. For $^1S_0$ and a cut-off $\Lambda \sim 500 - 250$ MeV the $V_{\text{low k}}$ becomes cut-off independent. Decreasing the cut-off further below the 2π exchange threshold, which corresponds to a momentum $k \approx 280$ MeV, the cut-off insensitivity disappears since the pion contributions are finally integrated out.
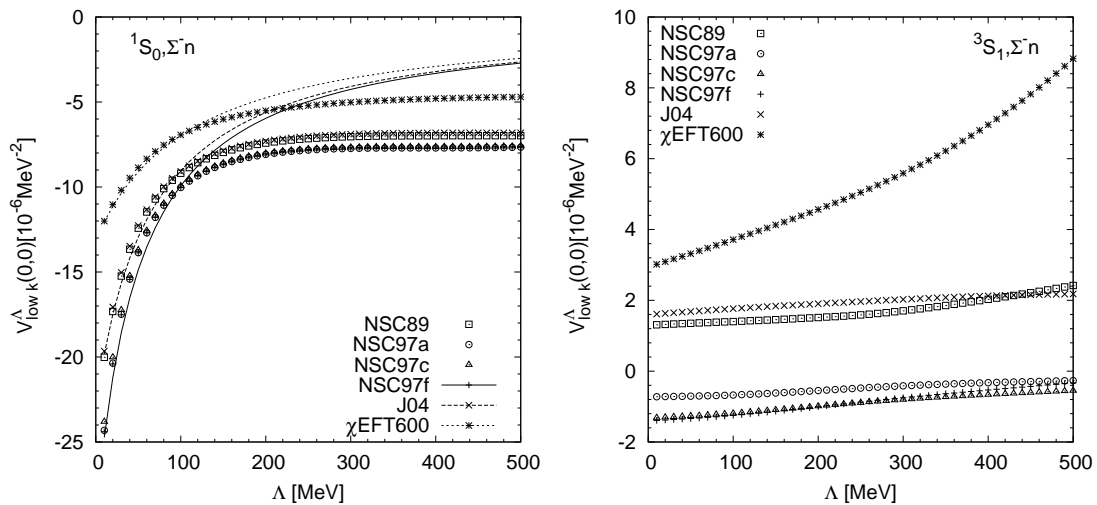
Figure 1.6: Left:$V_{\text{low k}}{}^\Lambda(0)$ in $^1S_0$ partial wave for various bare potentials as a function of the cut-off Λ in the $\Sigma^- n$ channel. Prediction from effective range theory (lines) are added. Right:$V_{\text{low k}}{}^\Lambda(0)$ for the $^3S_1$ channel.

In the opposite direction, i.e. for $\Lambda \to \infty$ no fluctuations have been integrated and the $V_{\text{low k}}$ tends to the bare potential.

The limit $\Lambda \to 0$ should yield the scattering length. In the limit of small cut-offs an analytic solution obtained in the framework of the effective theory, see

[32], is given by

$$V_y(0) = \left[2\frac{\mu_y}{a_0} - 2\frac{\Lambda}{\pi} \right]^{-1} \qquad \text{for} \qquad \Lambda \to 0 \,, \qquad (1.4)$$

where we have simplified our notation in an obvious manner. Here, the scattering length a_0 is needed as an input which we have calculated in the standard effective range approximation directly from the T-matrix for the $^1S_0$ channel from the $V_{\text{low k}}$ potential. In this approximation the T-matrix for $q \leq \Lambda$ can be expanded as

$$q \cot \delta_0 = -\frac{1}{2\mu_y T_y(q, q; q^2)} = -\frac{1}{a_0} + \frac{1}{2} r_0 q^2 \,, \qquad (1.5)$$

where r_0 is the effective range. The results for the different YN flavor channels and for all potentials used in this work (bare OBE potentials and χEFT potentials with cut-offs between 550 and 700 MeV) are listed in Tab. 1.1 for the scattering length a_0 in units of fm and in Tab. 1.2 for the effective range r_0 also in fm.

	Λp	Λn	$\Sigma^0 p$	$\Sigma^0 n$	$\Sigma^+ p$	$\Sigma^+ n$	$\Sigma^- p$	$\Sigma^- n$
NSC97a	-0.71	-0.76	-2.46	-1.74	-6.06	-0.04	0.41	-6.13
NSC97b	-0.90	-0.96	-2.47	-1.72	-5.98	-0.04	0.41	-6.06
NSC97c	-1.20	-1.28	-2.41	-1.70	-5.90	-0.03	0.41	-5.98
NSC97d	-1.70	-1.82	-2.38	-1.68	-5.82	-0.03	0.41	-5.89
NSC97e	-2.10	-2.24	-2.38	-1.68	-5.82	-0.03	0.41	-5.90
NSC97f	-2.51	-2.68	-2.45	-1.74	-6.07	-0.05	0.42	-6.16
NSC89	-2.70	-2.72	-2.12	-1.57	-4.79	-0.09	0.23	-4.85
J04	-2.14	-2.11	-2.24	-1.63	-4.68	-0.18	0.04	-4.75
χEFT550	-1.80	-1.79	-1.76	-1.15	-3.82	0.12	0.31	-3.88
χEFT600	-1.80	-1.80	-1.25	-0.92	-2.70	0.10	0.20	-2.72
χEFT650	-1.80	-1.80	-1.43	-1.02	-3.06	0.09	0.21	-3.10
χEFT700	-1.80	-1.80	-1.50	-1.07	-3.19	0.06	0.20	-3.24

Table 1.1: Scattering lengths a_0 of $V_{\text{low k}}$ for different flavor channels in fm for the $^1S_0$ partial wave.

As is visible in Fig. 1.6 for small cut-offs Λ there is good agreement between the analytical expansion and the full $V_{\text{low k}}$ solution obtained from the flow equation.

Unfortunately, no general quantitative conclusion can be drawn from Tab. 1.1 and Tab. 1.2 due to the bad experimental situation for the YN data. The YN interaction is yet largely unknown. However, agreement of the scattering lengths of all NSC97 potentials except for the Λp and Λn channels is found. The latter

	Λp	Λn	$\Sigma^0 p$	$\Sigma^0 n$	$\Sigma^+ p$	$\Sigma^+ n$	$\Sigma^- p$	$\Sigma^- n$
NSC97a	5.87	6.12	4.58	0.60	3.28	-6602	24.8	3.27
NSC97b	4.93	5.10	4.68	0.59	3.29	-8491	25.0	3.28
NSC97c	4.11	4.23	4.79	0.57	3.30	-10670	25.4	3.29
NSC97d	3.46	3.53	4.91	0.54	3.30	-17115	25.4	3.29
NSC97e	3.19	3.24	4.90	0.52	3.29	-17326	25.2	3.29
NSC97f	3.03	3.09	4.60	0.51	3.25	-6341	24.1	3.24
NSC89	2.86	2.98	5.76	0.74	3.35	-1478	58.0	3.33
J04	2.93	3.09	3.76	1.04	3.32	-329	1232.0	3.30
χEFT550	1.73	1.84	6.10	-2.96	2.70	-825	34.1	2.68
χEFT600	1.77	1.88	5.32	-2.12	3.40	-780	10.2	3.39
χEFT650	1.75	1.86	5.10	-2.28	3.08	-1210	27.6	3.05
χEFT700	1.74	1.86	4.91	-2.17	2.97	-2450	34.8	2.95

Table 1.2: Effective range r_0 of $V_{\text{low k}}$ for different flavor channels in fm for the $^1S_0$ partial wave.

deviation is related to the different fits of the magnetic $F/(F + D)$ ratio in the Nijmegen potentials [16]. The remaining two potentials, NSC89 and J04, have different but comparable values to those of the NSC97 ones. Unfortunately, the difference between these potentials and the χEFT is large.

The right part of Fig. 1.6 shows the same as the left panel for the $^3S_1$ partial wave. Unlike the $^1S_0$ channel, $V_{\text{low k}}$ for the $^3S_1$ channel remains cut-off dependent. On the one hand, in the $^1S_0$ channel, the potential has a strongly repulsive core and on the other hand, in the $^3S_1$ channel, it has a strongly attractive core. Hence, during the RG decimation towards smaller cut-offs the potential gets more and more attractive (or less repulsive).

2 Infinite nuclear matter

Infinite nuclear matter represents a hypothetical system without surface effects and Coulomb interaction, whose relevant degrees of freedom are nucleons, or more generally baryons. It is a system that cannot be studied experimentally in a laboratory, but it is nevertheless a very useful and broadly used concept because of its simplicity and its connection with the inner part of atomic nuclei and neutron stars. Neutron stars support themselves against the gravitational collapse mainly by the degeneracy pressure of neutrons. However, as the density of the system increases one must consider the influence of the nuclear interaction as well as the appearance of other degrees of freedom like hyperons, or eventually even quarks.

If we wish to examine the properties of infinite nuclear matter it is appropriate to consider the single-particle wave functions as plane waves. This is convenient since they are already the solutions in the Hartree-Fock approximation. This is another motivation for using infinite nuclear matter, because the starting wave functions are known and simple.

In the following, in Sec. 2.1, we will first present the Hartree-Fock approximation which is used to calculate the ground state of dense matter. The calculation itself and the results for the single-particle potential as well as several other related quantities is presented in Sec. 2.2. The results follow in Sec. 2.2.2. At the end we will consider the inclusion of three-body forces in Sec. 2.3.

2.1 Hartree-Fock approximation

The main feature of the Hartree-Fock method is that the interactions among the baryons can be represented by an average potential felt by each of the baryons due to the presence of all other baryons. In the Hartree-Fock approximation the ground state is represented by a Slater determinant which is built from the single-particle wave functions of all particles. Thus, instead of a complicated correlated set of many-body states we have a simple product of the states.

We now consider an interacting system of particles described by a Hamiltonian

$$\hat{H} = \hat{M} + \hat{T} + \hat{V} \,, \tag{2.1}$$

where $\hat{M}$ is the mass operator, $\hat{T}$ the kinetic energy operator and $\hat{V}$ the two-body interaction. The total energy E of this system is then obtained as the expectation value of the Hamiltonian with respect to the ground state:

$$E = \langle\Phi|\,\hat{H}\,|\Phi\rangle = \langle\Phi|\,\hat{M}\,|\Phi\rangle + \langle\Phi|\,\hat{T}\,|\Phi\rangle + \langle\Phi|\,\hat{V}\,|\Phi\rangle \; . \tag{2.2}$$

In the case of a homogenous infinite system, the appropriate single-particle states are plane-wave states, cf. Eq. (B.3). This property is the main appeal of this approximation. The starting single-particle wave functions are known and simple, which is not the case otherwise, such as for nuclei or atoms.

If we assume that the temperature of the system is equal to zero we can use these states to derive the usual connection between the density of the states and the Fermi momentum of the particles:

$$\rho_{sm_s tm_t} = \frac{1}{6\pi^2} p_{F sm_s tm_t}^3 \; . \tag{2.3}$$

In this expression spin is $sm_s = \uparrow, \downarrow$ and isospin is $tm_t = p, n, \Lambda, \Sigma^-, \Sigma^0, \Sigma^+$. The total baryonic density of the system is defined as the sum over all states.

$$\rho_B = \sum_{sm_s tm_t} \rho_{sm_s tm_t} \; . \tag{2.4}$$

We note that in this thesis we will not deal with polarized matter, hence all densities and momenta of particles with different spins will be equal. This yields

$$\rho_{tm_t} = \frac{1}{3\pi^2} p_{F tm_t}^3 \; , \tag{2.5}$$

$$\rho_B = \sum_{tm_t} \rho_{tm_t} \; . \tag{2.6}$$

We can use the states defined by Eq. (B.3) directly to calculate the mass (Eq. (B.7)) and the kinetic (Eq. (B.8)) part of Eq. (2.2). As for the potential part, we cannot use the plane wave states directly since the potential is usually given in partial waves. Thus, we need to change our basis first, which is done in Appendix B.1.2. This will then give the potential part (Eq. (B.26)), and the

resulting Hartree-Fock ground-state energy is finally given by

$$
\begin{aligned}
E =& \frac{\Omega}{\pi^2} \left(M_\Lambda \frac{p_{F_\Lambda}^3}{3} + \sum_N M_N \frac{p_{F_N}^3}{3} \sum_\Sigma M_\Sigma \frac{p_{F_\Sigma}^3}{3} \right) \\
&+ \frac{\Omega}{2\pi^2} \left(\frac{p_{F_\Lambda}^5}{5M_\Lambda} + \sum_N \frac{p_{F_N}^5}{5M_N} + \sum_\Sigma \frac{p_{F_\Sigma}^5}{5M_\Sigma} \right) \\
&+ \frac{\Omega}{\pi^2} \sum_{t_1 m_{t_1}} \sum_{t_2 m_{t_2}} \left(\frac{M}{m_{t_1 m_{t_1}}} \right)^3 \int_0^{p_{F_{t_1 m_{t_1}}}} dp_1 p_1^2 \int_{-1}^{1} dt \int_{q_{min}}^{q_{max}} dq q^2 \sum_{SM_S} \sum_{LM_L} \sum_J \\
&\frac{2L+1}{4\pi} \frac{(L-M_L)!}{(L+M_L)!} \left(\begin{array}{cc|c} L & S & J \\ M_L & M_S & M_L+M_S \end{array} \right)^2 (P_L^{M_L}(t))^2 \\
&\left[V_{(LS)Jt_1 m_{t_1} t_2 m_{t_2}}^{\text{di}}(q) - (-1)^{1-S+L} V_{(LS)Jt_1 m_{t_1} t_2 m_{t_2}}^{\text{xc}}(q) \right] , \quad (2.7)
\end{aligned}
$$

with the integration limits derived in Appendix B.

When using the $V_{\text{low k}}$ potential in Eq. (2.7), we need to keep in mind that it is limited to the maximal momentum value of $q = 500$ MeV or slightly more in the case of heavier channels, by the sharp cutoff. This puts a restriction on the values of the densities we can have when using the $V_{\text{low k}}$. In pure neutron matter this limit will be around $\sim 3\rho_0$ while for symmetric nuclear matter it would be $\sim 6\rho_0$. These restrictions come from considering the Fermi momentum of the neutron which is usually the highest. We also need to keep in mind that the effects of a sharp cut-off show up before the relative momentum q reaches the value of cut-off. Thus it is best to keep the relative momentum somewhat lower.

2.2 Single-particle potential

Generally, the single-particle potential is defined as the diagonal part in spin and isospin space of the proper self-energy for the single-particle Green's function in the Hartree-Fock approximation. It represents to first-order the interaction energy of a particle with incoming momentum p and given spin and isospin with the filled Fermi sea. For an interaction V the single-particle potential $U_{t_1 m_{t_1}}(p)$ describes the behavior of the incoming particle with momentum p in the dense medium, i.e. its interaction with a filled Fermi sea of all other particles. Pictorially, the single-particle potential is represented by Goldstone diagrams as shown in Fig. 2.1.
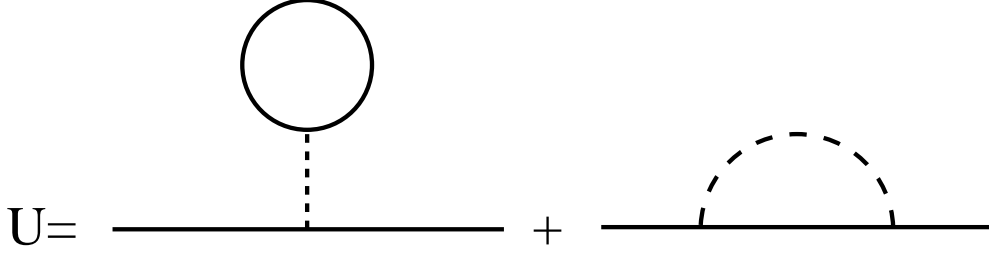
Figure 2.1: Goldstone diagrams for single-particle potential.

In the Hartree-Fock approximation the single-particle potential is defined as

$$U_{t_1 m_{t_1}}(\vec{p}_1) = \frac{1}{2} \sum_{s_1 m_{s_1}} \sum_{s_2 m_{s_2} t_2 m_{t_2}} \int d^3 \vec{p}_2$$

$$(\vec{p}_1, s_1 m_{s_1}, t_1 m_{t_1}; \vec{p}_2, s_2 m_{s_2}, t_2 m_{t_2} | V | \vec{p}_1, s_1 m_{s_1}, t_1 m_{t_1}; \vec{p}_2, s_2 m_{s_2}, t_2 m_{t_2}) , \quad (2.8)$$

where the spin-averaging was performed to remove the spin-dependence of the single-particle potential. We have done this since we will not be dealing with spin-polarized matter and the contributions from the spin-up ↑ and spin-down ↓ states are the same.

Just as in the case of the potential part of the ground-state energy in Eq. (2.8), we need to make a basis transformation from plane waves to partial waves. The single-particle potential $U_{t_1 m_{t_1}}(p_1)$ for a particle with momentum $p_1 = |\vec{p}_1|$ is obtained from the diagonal elements of the potential matrix, where, as before for the ground-state energy, we have two contributions the (direct) Hartree- and the (exchange) Fock-term [33]

$$U_{t_1 m_{t_1}}(p_1) = \sum_{t_2 m_{t_2}} \int_{-1}^{1} dt \int_{q_{min}}^{q_{max}} dq q^2 \sum_{S M_S} \sum_{L M_L} \sum_{J}$$

$$\frac{2L+1}{2\pi} \frac{(L-M_L)!}{(L+M_L)!} \left(\begin{array}{cc|c} L & S & J \\ M_L & M_S & M_L + M_S \end{array} \right)^2 (P_L^{M_L}(t))^2$$

$$\left[V_{(LS)J t_1 m_{t_1} t_2 m_{t_2}}^{\mathrm{di}}(q) - (-1)^{1-S+L} V_{(LS)J t_1 m_{t_1} t_2 m_{t_2}}^{\mathrm{xc}}(q) \right] , \quad (2.9)$$

with the integration limits being the same as for the ground-state energy.

2.2.1 Single-particle energy and the effective mass

The single-particle energy for the states defined by Eq. (B.2) is

$$\epsilon_{s m_s t m_t}(\vec{p}) = M_{s m_s t m_t} + \frac{p^2}{2 M_{s m_s t m_t}} + U_{s m_s t m_t}(\vec{p}) . \quad (2.10)$$
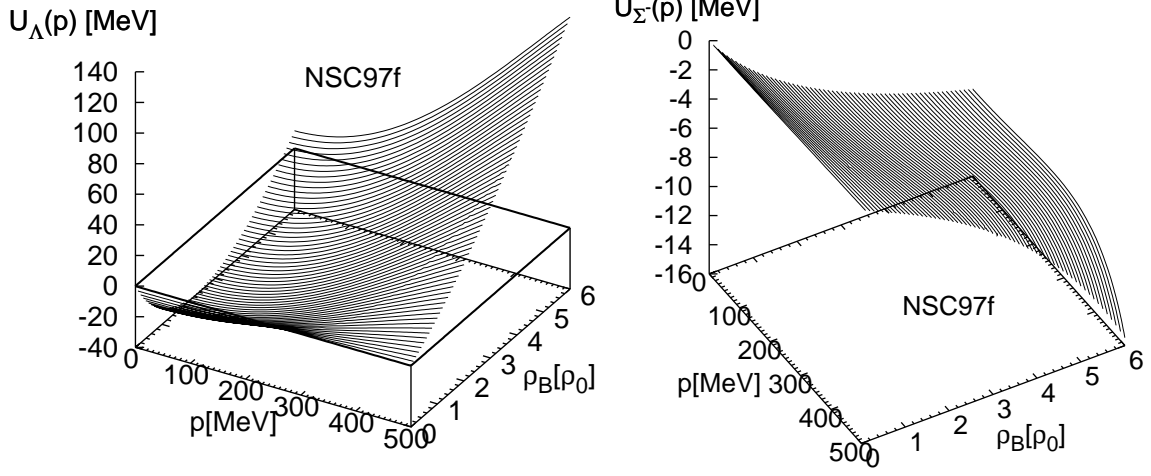
Figure 2.2: Momentum and density dependence of $U_\Lambda(p)$ (left), and for $U_{\Sigma^-}(p)$ (right), for symmetric nuclear matter. The NSC97f has been used as the bare potential.

Mostly we will perform our nuclear matter calculations at zero or very low temperatures, at least compared to the Fermi energy, hence the potential will be influenced most by the momenta at and around Fermi momentum. This gives rise to the quadratic approximation of the single-particle energy:

$$\epsilon_{sm_s tm_t}(\vec{p}) = M_{sm_s tm_t} + \frac{p^2}{2M^*_{sm_s tm_t}} + \tilde{U}_{sm_s tm_t}(p_{F_{sm_s tm_t}}) \,, \qquad (2.11)$$

where $M^*_{sm_s tm_t}$ is the effective mass. The advantage of such an approximation is twofold. It retains the shape of the free single-particle energy spectrum and $\tilde{U}$ is independent of the momentum p. This will enable us to perform some of the later calculations analytically without losing much accuracy.

The effective mass can than be calculated as

$$\frac{1}{M^*_{sm_s tm_t}} = \frac{1}{p_{F_{sm_s tm_t}}} \left. \frac{\partial \epsilon_{sm_s tm_t}(\vec{p})}{\partial p} \right|_{p=p_{F_{sm_s tm_t}}} = \left. \frac{\partial^2 \epsilon_{sm_s tm_t}(\vec{p})}{\partial p^2} \right|_{p=p_{F_{sm_s tm_t}}} , \quad (2.12)$$

and $\tilde{U}$ is

$$\tilde{U}_{sm_s tm_t}(p_{F_{sm_s tm_t}}) = \frac{p^2_{F_{sm_s tm_t}}}{2} \left(\frac{1}{M_{sm_s tm_t}} - \frac{1}{M^*_{sm_s tm_t}} \right) + U(p_{F_{sm_s tm_t}}). \qquad (2.13)$$

2.2.2 Symmetric nuclear matter

As an example, the numerical solution of Eq. (2.9) for the full momentum and density dependent single-particle potential of the Λ hyperon with momenta up to 500 MeV and nuclear densities up to $6\rho_0$ is shown on the left-hand side of Fig. 2.2, where the NSC97f YN potential of the Nijmegen group has been used as the bare potential for the underlying $V_{\text{low k}}$ calculation, cf. [34]. One sees that with increasing density, the momentum dependence becomes stronger, indicating a decrease of the effective mass as the density increases.

Similarly, the right-hand side of Fig. 2.2, shows the full momentum and density dependence of the Σ^- single-particle potential for symmetric nuclear matter, based on the NSC97f YN potential. Here, the slope of the momentum dependence is less pronounced which leads to a weaker density-dependent effective mass. However, unlike in the Λ case, the curvature becomes negative at higher densities, leading to an effective mass which is larger than the bare mass.
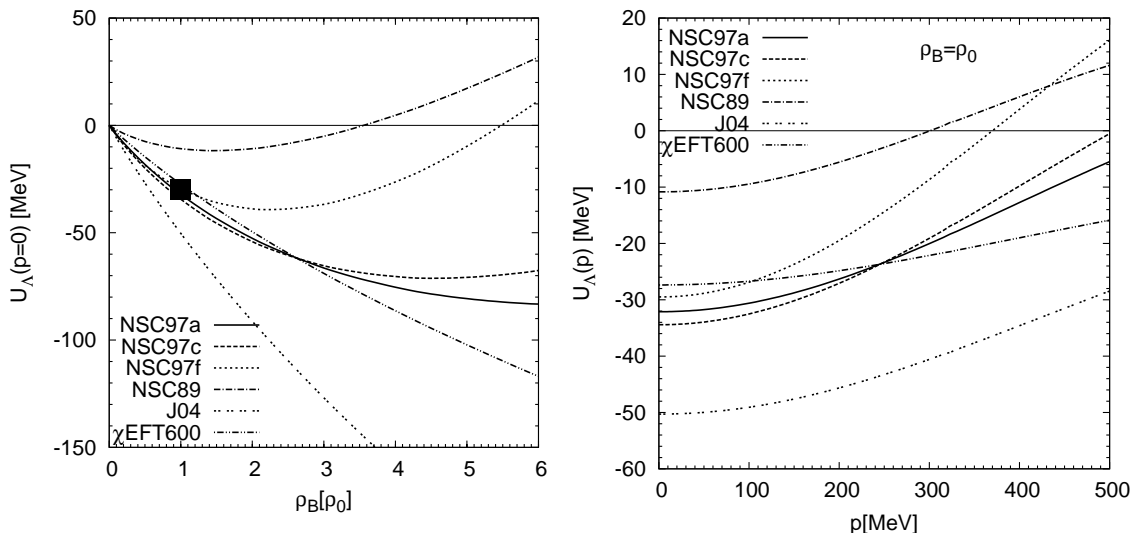

Figure 2.3: $U_\Lambda(p = 0)$ as a function of density in symmetric nuclear matter is shown in the left panel. The square represents the empirical point $U_\Lambda(p = 0) \approx -30$ MeV [35]. The momentum dependence of $U_\Lambda(p)$ at saturation density in symmetric nuclear matter is shown in the right panel.

The density dependence for several Λ single-particle potentials at rest (i.e. $p = 0$) in symmetric nuclear matter is compared in the left panel of Fig. 2.3. The square represents the generally accepted empirical potential depth of $U_\Lambda(p = 0) \approx -30$ MeV. This value has been confirmed recently by an analysis of the (π^-, K^+) inclusive spectra on various target nuclei as best fits in a framework of a distorted-wave approximation [35]. While most potentials can reproduce this

value, the Jülich potential (J04) yields a stronger binding and the old Nijmegen potential (NSC89) underestimates the binding.

With the exception of the J04 and NSC89 potentials, all interactions yield identical single-particle potentials up to the saturation density. However, with increasing density, the differences between these potentials grow, leading to different bindings at rest. This will have consequences for the predictions of the Λ hyperon concentration in dense nuclear matter. In particular, this will affect the maximum mass of neutron stars. It is interesting to observe that even the Nijmegen potentials NSC97a-f differ at higher densities. The only difference between these potentials is the magnetic $F/(F+D)$ ratio.

In the past, the potentials NSC89, NSC97a and NSC97f have also been used as a basis for a single-particle potential calculation in the G-matrix formalism [36, 37]. These G-matrix calculations yield a more attractive Λ single-particle potential. For example, at saturation density a potential depth of -29.8 MeV is found for the NSC89 potential, the NSC97a gives -39.7 MeV, and the NSC97f -36.6 MeV. On the other hand, a comparison with another G-matrix calculation [16], which uses a different prescription for the intermediate spectra, yields similar results to ours.

In Fig. 2.3, on the right-hand side, the momentum dependence of the Λ single-particle potential at saturation density is shown for various YN potentials. While all potentials increase with increasing momentum, the slopes deviate from each other. Similar differences in the momentum behavior of the single-particle potential are also seen in other works, cf. e.g. [36, 38].

	$^1S_0$	$^3S_1$	$^1P_1$	$^3P_0$	$^3P_1$	$^3P_2$	$^3D_1$	U_Λ
NSC97a	-4.86	-27.79	1.70	-0.10	2.10	-2.03	-0.09	-32.12
NSC97b	-6.69	-27.40	1.86	0.05	2.53	-1.87	-0.09	-32.72
NSC97c	-9.06	-27.54	1.96	0.36	2.84	-1.72	-0.09	-34.42
NSC97d	-12.14	-26.05	2.22	0.64	3.54	-1.33	-0.08	-34.46
NSC97e	-13.92	-24.43	2.43	0.75	4.09	-1.03	-0.07	-33.50
NSC97f	-15.37	-20.85	2.85	0.68	5.09	-0.47	-0.05	-29.49
NSC89	-15.73	4.52	2.00	0.52	2.55	-3.46	-0.07	-10.84
J04	-9.55	-35.18	-0.15	-0.70	0.58	-3.17	-1.31	-50.28
χEFT550	-11.11	-15.46	1.50	-1.69	3.17	-0.07	-3.14	-27.14
χEFT600	-12.29	-11.39	1.50	-1.73	3.17	-0.07	-6.14	-27.37
χEFT650	-11.99	-6.70	1.50	-1.77	3.17	-0.07	-9.90	-26.27
χEFT700	-11.91	-1.77	1.50	-1.81	3.17	-0.08	-13.84	-25.35

Table 2.1: Partial wave contributions to the Λ single-particle potential $U_\Lambda(p=0)$ at $\rho_B = \rho_0$ in symmetric nuclear matter.

Additionally, Eq. (2.9) cannot only be used for the calculation of the single-particle potential, but also to extract the individual partial wave contributions to the total single-particle potential. These contributions are obtained by neglecting the summation over the LSJ quantum numbers in Eq. (2.9), and will be labeled $U_Y\left(^{2S+1}L_J\right)$ in the following.

In Tab. 2.1 and Tab. 2.2 the resulting partial wave contributions to the U_Λ and U_{Σ^-} single-particle potentials for zero momenta at saturation density are listed for several YN interactions.

	$^1S_0$	$^3S_1$	$^1P_1$	$^3P_0$	$^3P_1$	$^3P_2$	$^3D_1$	U_{Σ^-}
NSC97a	3.51	-4.87	-2.16	0.59	1.46	-2.41	-0.01	-4.73
NSC97b	3.58	-5.37	-2.14	0.63	1.54	-2.31	-0.01	-4.91
NSC97c	3.48	-6.50	-2.12	0.68	1.59	-2.18	0.00	-5.86
NSC97d	3.50	-6.08	-2.02	0.71	1.70	-1.92	0.01	-4.88
NSC97e	3.50	-5.24	-1.94	0.72	1.78	-1.75	0.02	-3.65
NSC97f	3.51	-5.11	-1.85	0.71	1.90	-1.60	0.02	-3.14
NSC89	-4.32	11.46	-0.77	0.93	2.27	-1.49	0.28	7.61
J04	-7.63	1.84	-0.15	0.52	-0.70	-3.37	-3.65	-15.13
χEFT550	2.28	14.69	1.50	-0.20	0.09	-0.01	-2.73	14.11
χEFT600	-3.70	66.26	1.50	-0.28	0.06	-0.01	-5.36	56.89
χEFT650	-2.72	42.41	1.50	-0.35	0.01	-0.01	-8.60	30.38
χEFT700	-2.93	39.93	1.50	-0.41	-0.04	-0.02	-11.60	24.68

Table 2.2: Partial wave contributions to the Σ^- single-particle potential $U_{\Sigma^-}(p = 0)$ at $\rho_B = \rho_0$.

In these tables the partial waves up to $L = 2$ are shown and the last column contains the sum up to $L = 5$. As expected, the influence of the S-wave is most dominant. One can see that the combination of the coupled $^3S_1$ and $^3D_1$ channels provides most of the attraction in the majority of the Λ single-particle potentials.

These tables also illustrate the different contributions to the hyperon single-particle potential originating from the central, spin-spin and spin-orbit parts of the YN interaction. Furthermore, one recognizes from the different bare NSC97a-f potentials that a change in the $F/(F + D)$ ratio affects the single-particle potential for the Λ stronger than for the Σ. Another interesting feature is that χEFT successfully reproduces the potential depth at saturation density. For this density, χEFT agrees well with the Nijmegen NSC97a-f potentials.

On the left-hand side Fig. 2.4 shows a comparison of the $U_\Lambda(p = 0)$ density dependence obtained from χEFT , with results from Ref. [39]. Perfect agreement for the $U_\Lambda(p = 0)$ is evident and the independence of the χEFT single-particle po-

tential on the regulator cutoff is also seen. This suggests that the two approaches, [39] and [40], to construct an χEFT are closely related. Furthermore, χEFT in leading order can already produce a reasonable ΛN potential.
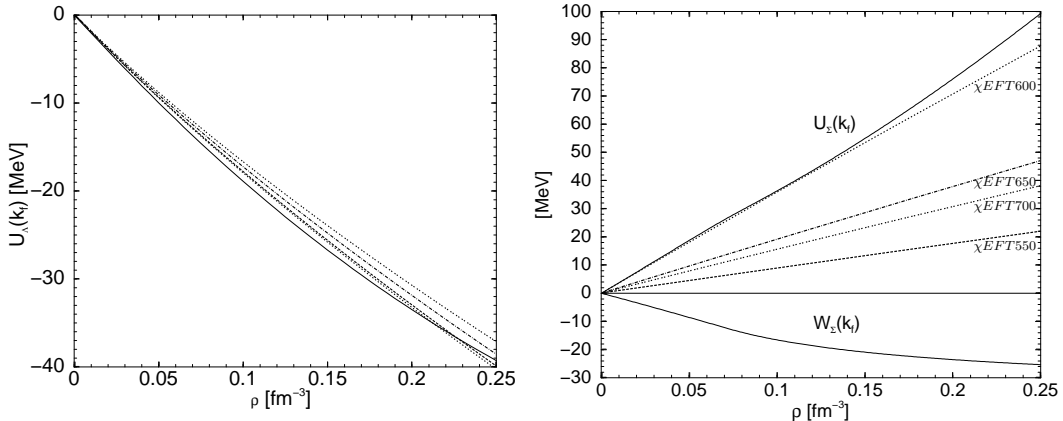

Figure 2.4: Left: Density dependence of $U_\Lambda(p=0)$ for symmetric nuclear matter. The full line is from [39] and the dashed lines represent χEFT for various regulator cutoffs. Right: Density dependence of $U_\Sigma(p=0)$ for symmetric nuclear matter. The full line is from [41] and the dashed lines represent χEFT for various values of regulator cutoff.

The left panel of Fig. 2.5 shows the density dependence for several Σ^- potentials at rest in symmetric nuclear matter like in Fig. 2.3 for Λ. The other members of the Σ triplet, Σ^+ and Σ^0, exhibit an almost identical behavior. A small difference compared to the Σ^- case is seen due to a small difference in their masses. Therefore, we will discuss only the Σ^- single-particle potential. For the Σ^- potential no density range is found where all, or even most, potentials agree. However, the difference between the NSC97a-f potentials is not significant and is the same over the entire density range shown. This confirms that the influence of the magnetic $F/(F+D)$ ratio on the ΣN interaction is less important than on the ΛN interaction. Due to experimental uncertainties in the case of the Σ^- potential, no generally accepted empirical point can be used as a reference. On the whole, the experimental situation concerning the Σ^- case is confusing: on the one hand, recent results [35] based on a distorted wave impulse approximation, yield a repulsive potential of the order of 100 MeV; on the other hand, the analysis of the same data by Kohno et al. [42] in a semiclassical distorted-wave model and an analysis by Maekawa et al. [43] within a distorted-wave impulse approximation with a local optimal Fermi-averaging T-matrix find a clearly less repulsive potential. Additionally, there also exists a bound state of $^4_\Sigma He$ [44], which definitely requires an attractive potential. Thus, neither theory nor experiment give a conclusive scenario in this case.
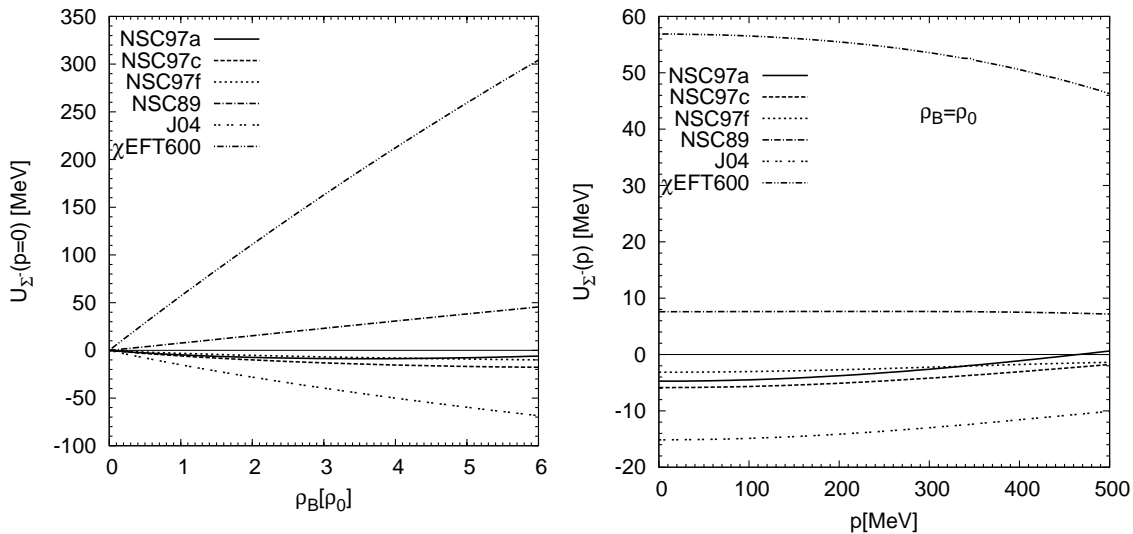
Figure 2.5: $U_{\Sigma}^-(p = 0)$ as a function of density in symmetric nuclear matter is shown in the left panel. The momentum dependence of $U_{\Sigma}^-(p)$ at saturation density in symmetric nuclear matter is shown in the right panel.

Compared to the G-matrix calculation a stronger binding of the Σ^- single-particle potential is found. In particular, the NSC89 potential yields a binding energy of -15.3 MeV [36], while -29.7 MeV and -25.5 MeV are found for the NSC97a and the NSC97f potential, respectively [37]. In order to understand the origin of such a significant difference, the single partial wave contributions to the single-particle potential of Ref. [36] are compared to each other. The $^1S_0$ channel contributions are approximately the same while those for the $^3S_1$ channel are significantly different. This difference in the $^3S_1$ channel is present for both, the Λ and Σ^- potentials, and is the result of a difference in the treatment of the $^3S_1$ $\Lambda N - \Sigma N$ channel. Since both, the $V_{\text{low k}}$ and the G-matrix formalisms, construct the effective interaction out of the same bare interaction, the difference comes from the treatment of the attractive part of the bare potentials which is found above the cutoff. Essentially the difference is in how much "attraction" is transferred when constructing the effective interaction. This is similar to the case shown in Fig. 1.6 (right), where a cutoff dependence is visible: for each lower cutoff more "attraction" is effectively added to the interaction.

However, it is interesting to note that the effective potentials constructed in the G-matrix calculations for the NSC89, NSC97a and NSC97f potentials depend on the underlying bare potentials in a similar way as the potentials shown here. This is another sign that the uncertainties are inherent in the underlying potentials.

Going back to Fig. 2.5 once more, the momentum dependence of the Σ^- single-particle potential at saturation density for various YN potentials is displayed on

the right-hand side. This figure illustrates how strong the parameterization of the YN interaction deviates. The potentials at zero momentum as well as their momentum dependence are very different. This demonstrates how poorly the ΣN interaction is constrained.

The right panel of Fig. 2.4 shows the density dependence of the real part $U_\Sigma(p = 0)$ and the imaginary part $W_\Sigma(p = 0)$ of the single-particle potential in an optical potential calculation [41] together with the results obtained from χEFT . The most interesting feature here is that all single-particle potentials are positive and grow with increasing density in contrast to the other potentials. However, unlike in the case of the Λ potential, the Σ^- single-particle potential depends on the regulator cutoff and only χEFT with a cutoff of 600 MeV agrees with the results of Ref. [41] quantitatively. As already mentioned, the repulsive Σ^- single-particle potential, which grows with density, has been suggested by Saha et al. [35] by means of an analysis of (π^-, K^+) inclusive spectra.

Recently, a calculation of the binding energy of the Λ hyperon in nuclear matter within a Dirac-Brueckner-Hartree-Fock framework was performed using the most recent Jülich meson exchange YN potential [45]. The reported values of the Λ single-particle potential, -51.27 MeV (-47.4 MeV) in the Brueckner-Hartree-Fock (Dirac-Brueckner-Hartree-Fock) framework agree well with our prediction of -50.28 MeV.

2.3 Three-nucleon force

It has long been known that soft nucleon-nucleon potentials without a hard core do not reproduce the saturation properties of nuclear matter correctly [46]. From the perspective of an effective potential this is not a failure but an expected feature which suggests that to obtain saturation in nuclear matter three or higher many-nucleon forces are required. Unfortunately, an RG based approach for the combined two- and three-body potential is not yet available, but an approximation can be made in which the three-body contributions are replaced by leading-order three-nucleon force from chiral effective field theory [47].

Thus we add the three-nucleon force from [47] to our $V_{\text{low k}}$ potential. This three-nucleon force contains a long-range 2π-exchange part V_c, an intermediate-range 1π-exchange part V_D and a short-range contact part V_E. The 2π-exchange interaction is given by

$$V_c = \frac{1}{2} \left(\frac{g_A}{2f_\pi} \right)^2 \sum_{i \neq j \neq k} \frac{(\vec{\sigma}_i \cdot \vec{q}_i)(\vec{\sigma}_j \cdot \vec{q}_j)}{(q_i^2 + m_\pi^2)(q_j^2 + m_\pi^2)} F_{ijk}^{\alpha\beta} \tau_i^\alpha \tau_j^\beta \ , \qquad (2.14)$$

where $\vec{q}_i = \vec{k}_i' - \vec{k}$ denotes the difference of initial and final nucleon momentum

and

$$F_{ijk}^{\alpha\beta} = \delta^{\alpha\beta} \left[-\frac{4c_1 m_\pi^2}{f_\pi^2} + \frac{2c_3}{f_\pi^2} \vec{q}_i \cdot \vec{q}_j \right] + \sum_\gamma \frac{c_4}{f_\pi^2} \epsilon^{\alpha\beta\gamma} \tau_k^\gamma \cdot (\vec{q}_i \times \vec{q}_j) \,, \qquad (2.15)$$

while the 1π-exchange and the contact interaction are given respectively by

$$V_D = -\frac{g_A}{8f_\pi^2} \frac{c_D}{f_\pi^2} \Lambda_\chi \sum_{i \neq j \neq k} \frac{\vec{\sigma}_j \cdot \vec{q}_j}{q_j^2 + m_\pi^2} (\vec{\tau}_i \cdot \vec{\tau}_j)(\vec{\sigma}_i \vec{q}_j) \,, \qquad (2.16)$$

$$V_E = \frac{c_E}{2f_\pi^4 \Lambda_\chi} \sum_{i \neq j \neq k} (\vec{\tau}_j \cdot \vec{\tau}_k) \,, \qquad (2.17)$$

where $g_A = 1.29$, $f_\pi = 92.4$ MeV and $m_\pi = 138.04$ MeV. The low-energy constants are $c_1 = -0.76$ GeV^{-1}, $c_3 = -4.78$ GeV^{-1} and $c_4 = 3.96$ MeV^{-1}. For Λ_χ a value of 700 MeV has been chosen [48]. In addition, all three contributions need to be multiplied with the square of the regulator used in three-nucleon force fits:

$$f_R(p,q) = \exp\left[-\left(\frac{p^2 + 3q^2/4}{\Lambda_R^2} \right)^4 \right] \,, \qquad (2.18)$$

where p and q are the Jacobi momenta and Λ_R is the regulator cutoff.

The low-energy constants c_D and c_E need to be fitted to some experimental data. The fit in Ref. [47] is to the experimental binding energies of ^3H and ^4He, but we also attempted a fit to the nuclear saturation energy and incompressibility. We refer to the first fit as "nuclei fit" while we label the second one with the value of incompressibility used to fit it. The values of the low-energy constants c_D and c_E at $\Lambda_R = 500$ MeV $= 2.534$ fm^{-1} are for the "nuclei fit" $c_D = -3.9268$ and $c_E = -1.1288$ [47], while for the nuclear fit with $K_0 = 220$ MeV we have $c_D = 54.9241$ and $c_E = 16.343$. However, since it is expected that both constants c_D and c_E are of "natural" size, i.e. of order one, the "nuclei fit" should be considered somewhat superior.

Since the three-nucleon force is given in operator form, there is no need to transform it to the partial wave basis. Thus, the three-body force contribution to the total energy is

$$\langle \Phi | V_{3NF} | \Phi \rangle = \frac{\Omega}{6(2\pi)^9} \sum_{s_1 m_{s_1}} \sum_{s_2 m_{s_2}} \sum_{s_3 m_{s_3}} \sum_{t_1 m_{t_1}} \sum_{t_2 m_{t_2}} \sum_{t_3 m_{t_3}} \int d^3\vec{p}_1 \int d^3\vec{p}_2 \int d^3\vec{p}_3$$

$$(\vec{p}_1, s_1 m_{s_1}, t_1 m_{t_1}; \vec{p}_2, s_2 m_{s_2}, t_2 m_{t_2}; \vec{p}_3, s_3 m_{s_3}, t_3 m_{t_3} | V_{3NF}$$

$$|\vec{p}_1, s_1 m_{s_1}, t_1 m_{t_1}; \vec{p}_2, s_2 m_{s_2}, t_2 m_{t_2}; \vec{p}_3, s_3 m_{s_3}, t_3 m_{t_3}) \,, \qquad (2.19)$$

where the states have been fully antisymmetrized as in the case of two body force, and are thus:

$$|\vec{p}_1, s_1 m_{s_1}, t_1 m_{t_1}; \vec{p}_2, s_2 m_{s_2}, t_2 m_{t_2}; \vec{p}_3, s_3 m_{s_3}, t_3 m_{t_3})$$
$$= \frac{1}{\sqrt{6}} \mathcal{A}_{123} |\vec{p}_1, s_1 m_{s_1}, t_1 m_{t_1}\rangle |\vec{p}_2, s_2 m_{s_2}, t_2 m_{t_2}\rangle |\vec{p}_3, s_3 m_{s_3}, t_3 m_{t_3}\rangle \ , \qquad (2.20)$$

where $\mathcal{A}_{123} = 1 - P_{12} - P_{13} - P_{23} + P_{12}P_{23} + P_{13}P_{23}$ is defined with the standard exchange operators introduced in Appendix B.1.2.
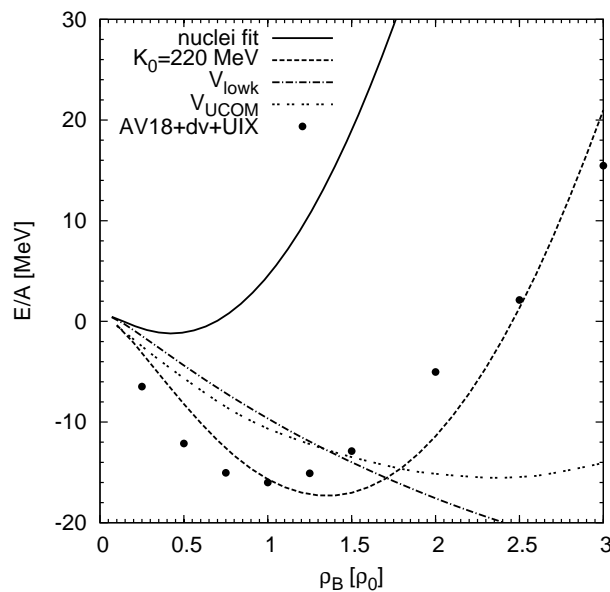
Figure 2.6: Energy per particle as a function of density in symmetric nuclear matter.

Fig. 2.6 shows the energy per particle for symmetric nuclear matter for several microscopic nucleon potentials. For comparison we also show the result for $AV18+ dv + UIX$ from Ref. [49] which reproduces the properties of nuclear matter at saturation nicely and is currently accepted as the most accurate nucleonic potential. If we compare its values, represented by points, and those of $V_{\text{low k}}$, our statement from the beginning of this section about the lack of saturation and the need for a three body force becomes clear. As is evident $V_{\text{low k}}$ shows no saturation in the density range shown here, but as noted before, this is not unexpected.

In addition, we also compare the results with the V_{UCOM} nucleon-nucleon potential from [50]. The V_{UCOM} makes use of unitary correlation operators to decouple the energy scales and thus transfers the high momentum effects to the low momenta. This property and the fact that both, $V_{\text{low k}}$ and V_{UCOM}, preserve

the phase shifts makes these two effective NN potentials similar, but differences in the construction lead to sufficient differences for these potentials to consider them distinct from one another. As visible in Fig. 2.6 they produce different results for nuclear matter, the biggest difference being that V_{UCOM} exhibits saturation at higher densities, but interestingly has almost the correct binding energy.

As for the combinations of the $V_{\text{low k}}$ with a three-nucleon force it is clear that for both, the nuclei fit as well as the nuclear fit, there is saturation, but it is not at the correct point. The fit to finite nuclei is especially bad for the calculations of nuclear matter because of its enormous stiffness. The nuclear matter fit has a more appropriate stiffness, but the asymmetry energy is much too large, $a_t = 42.46$ MeV and as mentioned before the values of c_D and c_E are too large. Unfortunately at this time there still does not exist a microscopic three-body force which can be used in combination with V_{UCOM} in nuclear matter calculations.

What we have seen here is that two-body interactions such as the $V_{\text{low k}}$ and V_{UCOM} alone are clearly not useful for standard many-body theory calculations of nuclear matter. While they improve the situation, the three-body forces coming from chiral perturbation theory do not reproduce the saturation properties of nuclear matter correctly. Since we are interested in investigating the properties of hyperons in nuclear matter we have to be sure that our nucleonic sector is as good as possible so that any conclusions made in the hyperonic sector are independent of it. This leads to the conclusion that we have to replace either the nucleonic sector with a suitable parameterization or to replace the three-body force with another one which in combination with two-body forces is capable of accurately reproducing the properties of nuclear matter.

We will explore both options in the following. In the next chapter we will replace the nucleonic part with a corresponding parameterization of the energy per particle. In the remaining chapters we will use a density-dependent Yukawa-like force to mimic the effect of the three-body force. Both of these substitutions have parameters which are fitted to the properties of nuclear matter. This makes them as reliable as possible for further calculations regarding the hyperons. The reason for using both is that they offer different insights into nuclear matter with hyperons.

3 EOS and β-equilibrium

An important application of infinite nuclear systems introduced in the previous chapter is the study of dense baryonic systems which can be found in astrophysical contexts such as the interior of neutron stars. Like all stars, a neutron star is a "battle" between the pull exerted by gravitation and a pressure generated inside the star. In the case of a neutron star, this pressure comes from the degeneracy pressure of the baryons. This makes a neutron star a unique structure where gravitational and nuclear forces are both of equal interest. While the low-density surface of a neutron star is explained in terms of nuclei and neutrons, the interior of it remains largely a mystery with many possibilities. These possibilities range from almost pure neutron matter with a few electrons and protons, through inclusion of exotic states such as hyperons, pions, kaons as well as various condensates, all the way to the possible realization of pure quark matter.

Inside a neutron star at densities above the "neutron drip line" we first expect to find the form of matter in which neutrons, protons and electrons exist in an equilibrium regulated by the weak force. This equilibrium is referred to as β-equilibrium because the β-decay and similar processes dominate. However, since the density increases as we go deeper into the star we expect other particles such as the hyperons to appear. It is reasonable to expect hyperons to appear first since they are the lightest baryons after the nucleons. Other possibilities include various condensates and quarks.

This chapter is organized as follows: Sec. 3.1 presents the formalism of the equation of state and other related quantities. In Sec. 3.2 we introduce and show results for the parametric equation of state. Sec. 3.3 is devoted to the calculation of β-equilibrium and the stellar composition. The resulting composition and threshold densities of hyperons are shown in Sec. 3.3.1 and Sec. 3.3.2, respectively. Finally, in Sec. 3.4, we show results and discus the consequences of hyperon emergence on the maximum mass of neutrons stars.

3.1   Equation of state

The equation of state (EoS) of nuclear matter relates pressure or energy with density and temperature for equilibrated nuclear matter. The quantity which one needs is the energy per particle, given by Eq. (2.7). Additional information which is needed is the composition which is determined by β-equilibrium. This will be explained later. The total energy can then be written as [1]

$$E/A = \frac{2}{\rho_B} \sum_b \int_0^{p_{F_b}} \frac{d^3p}{(2\pi)^3} \left(M_b + \frac{p^2}{2M_b} + \frac{1}{2}U_b(p) \right) , \qquad (3.1)$$

where we have used the single-particle potential.

With the help of the baryon density fraction, $x_b = \rho_b/\rho_B$, which relates to the Fermi momentum as

$$p_{F_b}^3 = 3\pi^2 x_b \rho_B , \qquad (3.2)$$

we can then express the EoS as

$$E/A = \sum_b \left(M_b x_b + \frac{3}{5}\frac{p_{F_b}^2}{2M_b}x_b + \frac{1}{\rho_B}\int_0^{p_{F_b}} \frac{p^2 dp}{2\pi^2}U_b(p) \right) . \qquad (3.3)$$

In symmetric nuclear matter the lowest energy is obtained by minimizing $\mathcal{E} = E/A$. This quantity then defines the saturation density ρ_0 (equivalently, p_{F_0}) and the energy $\mathcal{E}_0$ via

$$\left.\frac{\partial \mathcal{E}}{\partial \rho_B}\right|_{sat.} = 0 . \qquad (3.4)$$

The curvature at the saturation point with respect to ρ_B is proportional to the incompressibility,

$$K_0 = p_F^2 \left.\frac{\partial^2 \mathcal{E}}{\partial p_F^2}\right|_{sat.} = 9\rho_B^2 \left.\frac{\partial^2 \mathcal{E}}{\partial \rho_B^2}\right|_{sat.} , \qquad (3.5)$$

where we have defined the Fermi momentum p_F of nuclear matter composed of an equal number of protons and neutrons as $p_F = 3\pi^2 \rho_B/2$.

The volume symmetry energy corresponds to the curvature of $\mathcal{E}$ with respect to η_t,

$$a_t = \frac{1}{2}\left.\frac{\partial^2 \mathcal{E}}{\partial \eta_t^2}\right|_{sat.} = \frac{1}{8}\left.\frac{\partial^2 \mathcal{E}}{\partial x_p^2}\right|_{sat.} , \qquad (3.6)$$

---

[1] For the sake of clarity and brevity we have changed the notation somewhat. Now instead of explicit isospin indices tm_t we use an abbreviation b ($b \equiv tm_t$)

where $\eta_t^2 = (\rho_p - \rho_n)/\rho_B$.

For the experimental values of these quantities one can find the following values in the literature, cf. [51, 52]. For the saturation density one finds

$$\rho_0 = 0.16 \pm 0.02 \text{ fm}^{-3}. \tag{3.7}$$

The value of the energy per nucleon at saturation density, which in symmetric matter represents the lowest energy, is

$$\mathcal{E} = \frac{E}{A} = -15.6 \pm 0.2 \text{ MeV}, \tag{3.8}$$

the incompressibility at the same density is

$$K \approx 220 \pm 30 \text{ MeV}, \tag{3.9}$$

and the symmetry energy is

$$a_t \approx 30 \text{ MeV}. \tag{3.10}$$

3.1.1 Chemical potential

The chemical potential of a fermion at zero temperature is equal to its Fermi energy. Depending on the approximations we use there are two cases of interest, that of nonrelativistic interacting particles, baryons:

$$\mu_b = M_b + \frac{p_{F_b}^2}{2M_b} + U_b(p_{F_b}). \tag{3.11}$$

and that of relativistic noninteracting particles, in the form of leptons:

$$\mu_l = \sqrt{m_l^2 + (3\pi^2 \rho_l)^{\frac{1}{3}}}, \tag{3.12}$$

where ρ_l is the lepton density.

At finite temperature the chemical potential of fermions for a given density is found as a solution of the equation

$$\rho_i = \frac{1}{\pi^2} \int_0^\infty p^2 dp \frac{1}{1 + \exp\left((\epsilon_i - \mu_i)/T\right)}, \tag{3.13}$$

where ϵ_i is the single-particle energy of either leptons or baryons.

3.2   Parametric NN equation of state

It is well known that non-relativistic many-body calculations, based purely on two-body forces, fail to reproduce the empirical saturation point for symmetric nuclear matter. The usual solution to this problem is the introduction of three-body forces. However a three-body force which would complement the $V_{\text{low k}}$, while providing the correct binding properties of light nuclei, does not reproduce the properties of nuclear matter at saturation density [47], cf. Fig. 2.6. Because of this we will first attempt to include the higher-order effects by replacing the purely nucleonic contribution to the energy per particle

$$E_{NN}/A_N = \frac{2}{\rho_N} \sum_N \int_0^{p_{F_N}} \frac{d^3p}{(2\pi)^3} \left(M_N + \frac{p^2}{2M_N} + \frac{1}{2} U_N^N(p) \right), \qquad (3.14)$$

by an analytic parameterization developed by Heiselberg and Hjort-Jensen [6]

$$E_{NN}/A_N = M_N - E_0 u \frac{u - 2 - \delta}{1 + u\delta} + S_0 u^\gamma (1 - 2x_p)^2, \qquad (3.15)$$

where $u = \rho_N/\rho_0$ is the ratio of the total nucleonic density $\rho_N = (x_p + x_n)\rho_B$ to the nuclear saturation density.

In Eq. (3.14) we have separated the potential contribution of nucleons into one coming from the interaction with other nucleons, $U_N^N(p)$, and one coming from the interaction with hyperons, $U_N^Y(p)$. The separation can be written as

$$U_b(p) = U_b^N(p) + U_b^Y(p), \qquad (3.16)$$

where we define the nucleonic contribution from Eq. (2.9), with the isospin substitution $(b \equiv tm_t)$. The latter part, $U_N^Y(p)$, does not contribute to the pure nucleonic EoS and was thus not includes in the replacement.

$$U_b^N(p) = \sum_{b'=p,n} \int_{-1}^1 dt \int_{q_{min}}^{q_{max}} dq q^2 \sum_{SM_S} \sum_{LM_L} \sum_J$$
$$\frac{2L+1}{2\pi} \frac{(L-M_L)!}{(L+M_L)!} \left(\begin{array}{cc|c} L & S & J \\ M_L & M_S & M_L + M_S \end{array} \right)^2 (P_L^{M_L}(t))^2$$
$$\left[V_{(LS)Jbb'}^{di}(q) - (-1)^{1-S+L} V_{(LS)Jbb'}^{xc}(q) \right]. \qquad (3.17)$$

An analogous definition can be introduced for the hyperonic contribution. We also note that due to the lack of the YY interaction the single-particle potential contributions of the form $U_Y^Y(p)$ will be neglected throughout this work.

The used parameterization was fitted to the energy per particle obtained from variational calculations using the Argonne V_{18} nucleon-nucleon interaction with three-body forces and relativistic boost corrections. The best fit parameters are $E_0 = -15.8$ MeV, $S_0 = 32$ MeV, $\gamma = 0.6$ and $\delta = 0.2$ [49].

The advantage of using this parameterization is that, since we are primarily interested in the behavior of the hyperons, we want our nucleonic part of the EoS to be as reliable as possible. Since the EoS from [49] is considered as one of the most reliable ones avaliable, the usage of it removes as much as possible uncertainties coming from the nucleonic EoS. Thus we can be reasonably sure that any conclusion we make about the hyperons is not subject to effects coming from the nucleonic part.

Additionally this approximation will allow us to use the density range well above the range of validity of the NN $V_{\text{low k}}$, which is limited by the cut-off. In the case of symmetric matter at zero temperature the limit is $\sim 6\rho_0$ while for pure neutron matter that limit is $\sim 3\rho_0$. The extension of the density range will enable us to study the masses of neutrons stars with hyperons, since the maximum mass is usually reached at densities $\sim 7 - 10\rho_0$. The cut-off of the YN $V_{\text{low k}}$ will not pose a problem, since the concentrations of hyperons in neutron stars are not very large. The drawback is that our approach is no longer microscopic and not applicable for a Landau Fermi liquid calculation that we want to perform later on. For this reason in the next chapter we will go back to a more microscopic approach.

The parameters E_0, δ, S_0 are related to properties of nuclear matter at saturation density, i.e. E_0 is the binding energy per nucleon at saturation density while S_0 and δ are connected to the symmetry energy and the incompressibility, respectively. Since there are no hyperons at saturation density we can use Eq. (3.15) directly to find $a_t = S_0$ and $K_0 = -18E_0/(1 + \delta)$.

This parameterization should then enable us to study the effects of the hyperons without having to question the validity of the NN interaction. It also affords us the opportunity to change the incompressibility and symmetry energy in a generally accepted range of values. From experimental constraints an accepted range of values for K_0 is 200 MeV to 300 MeV and for a_t it is 28 MeV to 36 MeV, see [53] and references therein. We aim to use the parameterization and modify K_0 and a_t within this range. The goal is to study the effect of these two parameters on the appearance and concentrations of hyperons in dense matter. While these two parameters do not influence directly the concentration of particles, they do change the composition of the matter indirectly by changing the energy available, thus regulating the point at which the hyperons will appear.

In Fig. 3.1 the total energy per particle as a function of density is shown for symmetric nuclear matter, where only the result of the pure nucleonic part of the EoS from the parameterization Eq. (3.15) is used. In symmetric matter the
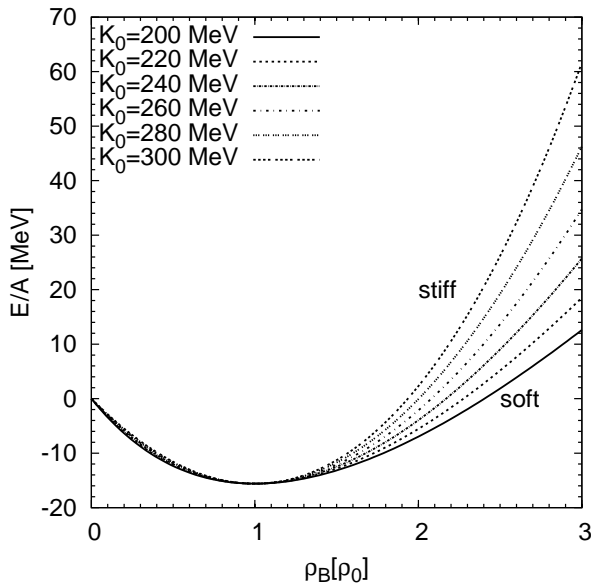
Figure 3.1: Parametric EoS in symmetric nuclear matter.

energy per particle is only sensitive to the incompressibility, which can be seen in the figure for values between $K_0 = 200$ MeV and $K_0 = 300$ MeV. The various EoS reproduce the saturation point at $E/A = -16$ MeV. The parameter K_0 allows us to classify the EoS as a stiffer ($K_0 = 300$ MeV) or a softer ($K_0 = 200$ MeV) one.

Additionally, the incompressibility will directly control the maximum allowed mass of a neutron star which is supported by the corresponding EoS. However, if hyperons are present this conclusion is no longer straightforward. The reason is that by increasing the incompressibility the energy of the system is also increased and as a consequence, more hyperons can be produced. This in turn will decrease the allowed maximum mass of a neutron star. However such a nontrivial connection creates a conundrum: if we use a stiffer EoS by increasing the incompressibility we then allow for higher hyperon concentrations which immediately softens the EoS again.

With the help of Eq. (3.14) we have separated the energy per particle in Eq. (3.1) into a purely nucleonic part and a remainder as

$$E/A = \frac{\rho_N}{\rho_B} E_{NN}/A + E'/A \, , \tag{3.18}$$

where the remainder is given by

$$E'/A = \frac{2}{\rho} \sum_N \int_0^{p_{F_N}} \frac{d^3p}{(2\pi)^3} \frac{1}{2} U_N^Y(p)$$

$$+ \frac{2}{\rho} \sum_Y \int_0^{p_{F_Y}} \frac{d^3p}{(2\pi)^3} \left(M_Y + \frac{p^2}{2M_Y} \right.$$

$$\left. + \frac{1}{2} U_Y^N(p) + \frac{1}{2} U_Y^Y(p) \right) . \tag{3.19}$$

In symmetric matter composed only of nucleons the E'/A will be equal to zero, but with this separation we are now able to calculate E/A with an arbitrary concentration of hyperons. In the following section, after we have determined the concentrations through the requirement of equilibrium, we will use it to calculate the equation of state with hyperons.

3.3 β-equilibrium
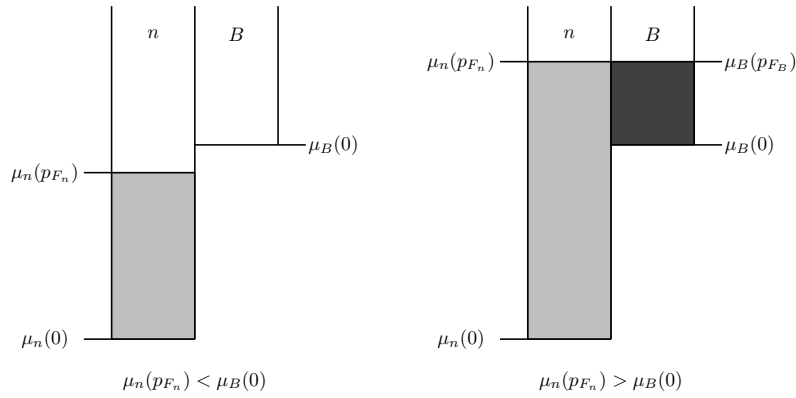
Figure 3.2: Schematic chemical equilibrium.

The concentrations of different constituents in stars are determined by the requirements of electric charge neutrality and equilibrium under weak and strong interaction processes. If we consider a general process with baryons B_2 and B_4, a lepton l and its corresponding neutrino ν_l, we have [54]

$$B_2 \rightarrow B_4 + l + \bar{\nu}_l; \quad B_4 + l \rightarrow B_2 + \nu_l , \tag{3.20}$$

where $l \in \{e^-, \mu^-, \tau^-\}$ are the negatively charged leptons and $\bar{\nu}_l$ the corresponding antineutrinos. For the condition of charge neutrality we require that

$$\sum_b \rho_b^{(+)} + \sum_l \rho_l^{(+)} = \sum_b \rho_b^{(-)} + \sum_l \rho_l^{(-)} \,, \qquad (3.21)$$

where the densities of positively and negatively charged baryons and leptons are denoted by $\rho_b^{(\pm)}$ and $\rho_l^{(\pm)}$, respectively. For the equivalence of chemical potentials we require

$$\mu_b = b_b \mu_n - q_b(\mu_l - \mu_{\nu_l}) \,, \qquad (3.22)$$

where the chemical potentials μ are labeled by the corresponding particle and b_b is its baryon number and q_b is its charge.

In the case of a medium composed of nucleons, hyperon and leptons where the neutrinos have left the system ($\mu_\nu = 0$) all lepton and all antilepton chemical potentials are equal. The β-equilibrium condition can then be written as explicitly:

$$\mu_{\Sigma^-} = \mu_n + \mu_e \,, \qquad (3.23)$$

$$\mu_\Lambda = \mu_{\Sigma^0} = \mu_n \,, \qquad (3.24)$$

$$\mu_{\Sigma^+} = \mu_p = \mu_n - \mu_e \,. \qquad (3.25)$$

For a given total baryon density ρ_B Eq. (3.21) and Eq. (3.22) govern the composition of the matter, i.e. the baryonic and leptonic concentrations. The corresponding solution is referred to as β-stable matter.

Fig. 3.3 shows the neutron chemical potential in β-equilibrated matter for all models. The hyperons start to appear at the point at which the lines representing the models with hyperons deviate from the pure NN line. As can be seen, once the hyperons appear, the slope of the curves changes, and the increase of the neutron chemical potential slows down. The second inflection point, which can be most clearly seen in the curve for NSC89 on the right-hand side, is a signature of the appearance of the second hyperon.

3.3.1   Composition of matter

For the sake of consistency we now have to treat the nucleonic part of the chemical potential μ_N in the same way as the corresponding energy per particle. Since the chemical potential can be obtained as a derivative of the energy density ϵ and is related to the energy per particle via $\epsilon = \rho_B E/A$, we use the definition

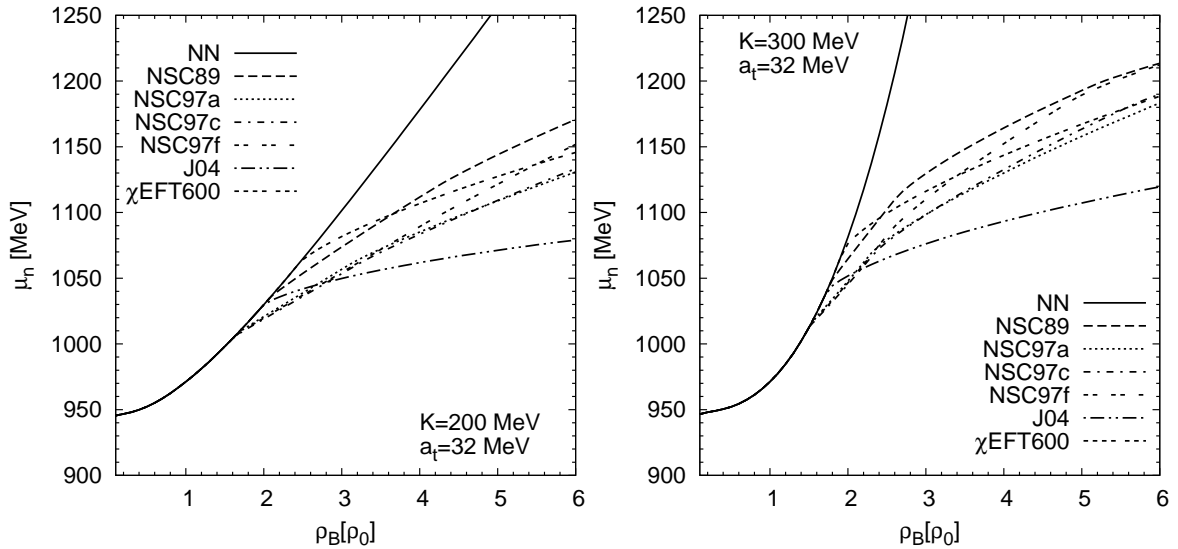$$\mu_b = \frac{\partial \epsilon}{\partial \rho_b} \,, \qquad (3.26)$$

Figure 3.3: Neutron chemical potential in β-equilibrated matter for all models with two different values for the incompressibility. On the left-hand side $K_0 = 200$ MeV, on the right-hand side $K_0 = 300$ MeV and for both $a_t = 32$ MeV.

to yield the appropriate replacement in the nucleonic chemical potential. Finally, we arrive at the expression

$$\mu_N = \frac{\partial \epsilon_{NN}}{\partial \rho_N} + U_N^Y(k_{F_Y}), \qquad (3.27)$$

where we have effectively replaced $M_N + \frac{k_{F_N}^2}{2M_N} + U_N^N(k_{F_N})$ of Eq. (3.11) with the derivative $\partial \epsilon_{NN}/\partial \rho_N$. In this way the parameterization Eq. (3.15) enters into the nucleonic part of the chemical potential.

Since we are only parameterizing the nucleonic sector, no such replacement is necessary for the hyperons. However, since we have neglected the YY interaction, $U_Y^Y(k_{F_Y})$ is zero and Eq. (3.11) reduces to

$$\mu_Y = M_Y + \frac{k_{F_Y}^2}{2M_Y} + U_Y^N(k_{F_Y}) . \qquad (3.28)$$

As an indicator for the densities at which hyperons start to appear we show the concentrations of all particles for two different values of K_0. The results are presented in Figs. 3.4 and 3.5. In Fig. 3.4 a "soft" EoS is used, while in Fig. 3.5 a "stiff" EoS is used. The point of the hyperon appearance can easily
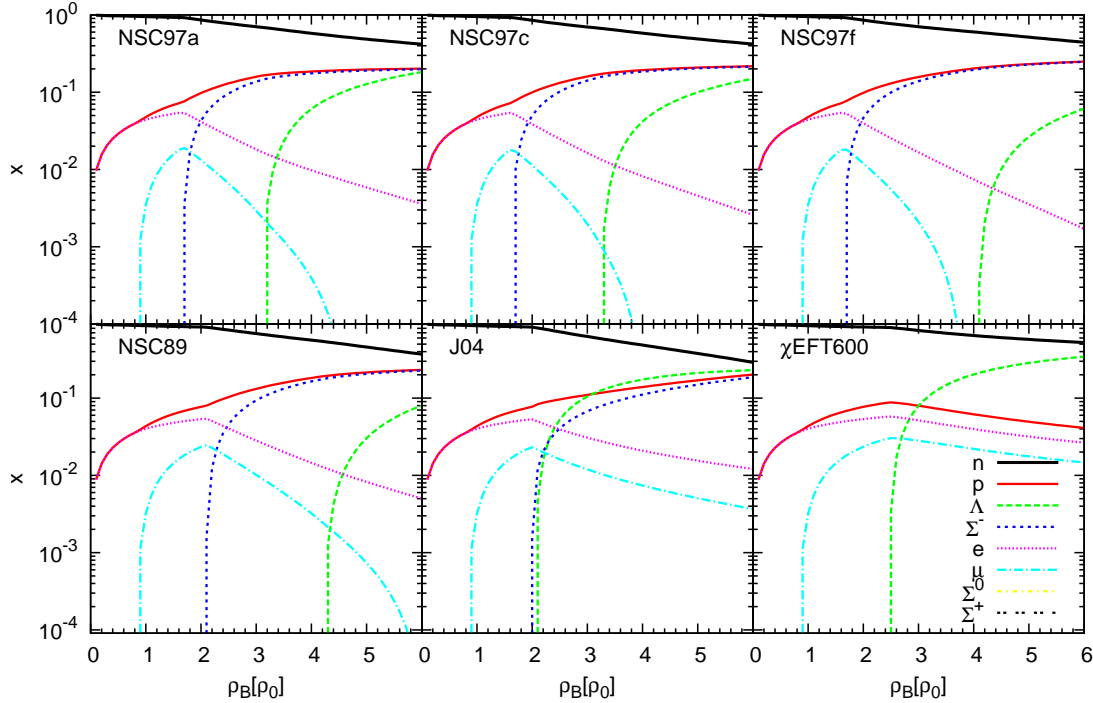
Figure 3.4: Particle fraction for a "soft" EoS with all YN interactions.

be estimated from these figures. Since the logarithmic scale begins at rather low concentrations all we need to do is to take the intersection of the density-axis with the appropriate curve describing the hyperon concentration and we get the hyperon threshold density. In all of the figures we can see how at the onset of the hyperon appearance their concentration rises quickly and then reaches a plateau after which the concentration changes very slowly.

It is notable that with the appearance of the Σ^- hyperon the density of the negatively charged leptons starts to drop immediately. This is because their role in the charge neutrality condition, Eq. (3.21), is now being taken over by the Σ^-. Similarly, the appearance of the Λ hyperon will accelerate the disappearance of neutrons since both are neutral particles.

Once the composition of matter has been determined by demanding β-equilibrium we can calculate the energy per particle. For this purpose, we cannot use Eq. (3.1), but have to use Eq. (3.18) and Eq.(3.15). The result is presented in Fig. 3.6 where the energy per particle in β-stable matter is shown as a function of density for the different YN models. The symmetry energy is fixed to $a_t = 32\,\text{MeV}$ while the incompressibility is set to $K_0 = 200\,\text{MeV}$ (left panel in the figure) and
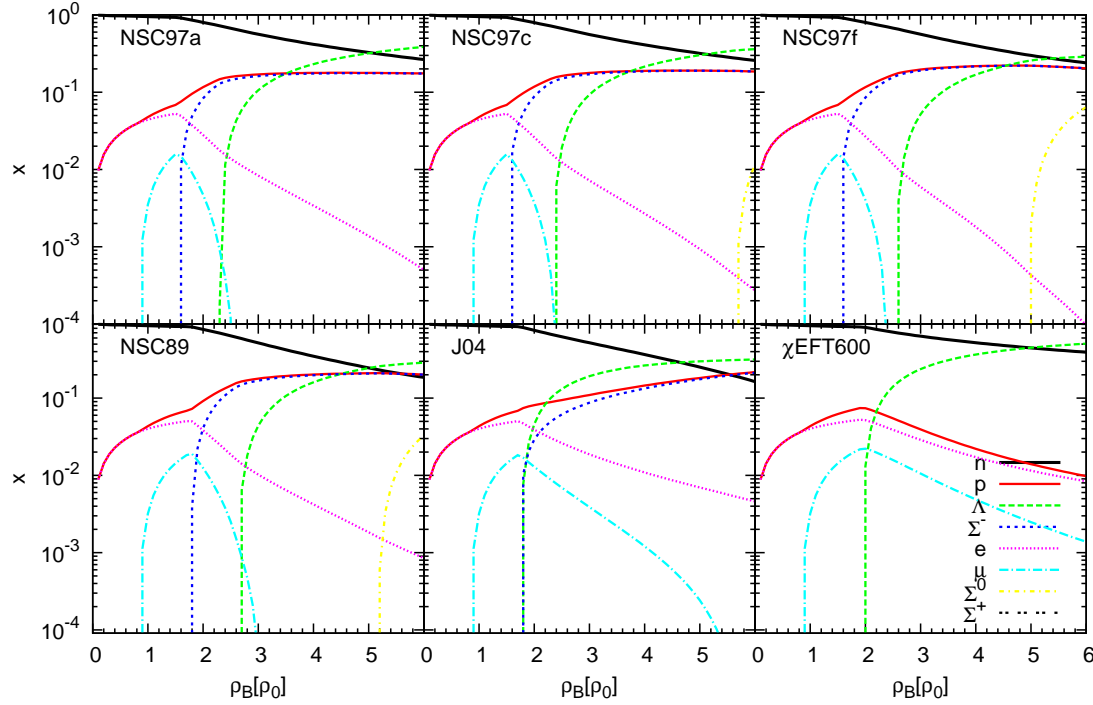
Figure 3.5: Particle fraction for a "stiff" EoS and all YN interactions.

to $K_0 = 300$ MeV (right panel). In addition, the EoS with hyperons is compared with the purely nucleonic one.

One easily observes the onset of hyperon appearance as the point at which the curves start to deviate. As expected the differences between the various YN interactions do not modify the EoS for very small densities. In the range between $(2-3)\rho_0$, all EoSs are similar to each other. However, for increasing densities the influence of hyperons becomes more significant resulting in rather different EoSs. This concerns not only the magnitudes of the different energies per particle but also their slopes at higher densities. These variations will lead to differences in the pressure and finally to significant changes in the possible maximum mass of a neutron star.

3.3.2 Threshold densities

The onset of a given hyperon species can be determined by increasing the density for fixed K_0 and a_t. The resulting threshold densities for the Σ^- hyperon for certain incompressibilities and symmetry energies are collected in Fig. 3.7 for six
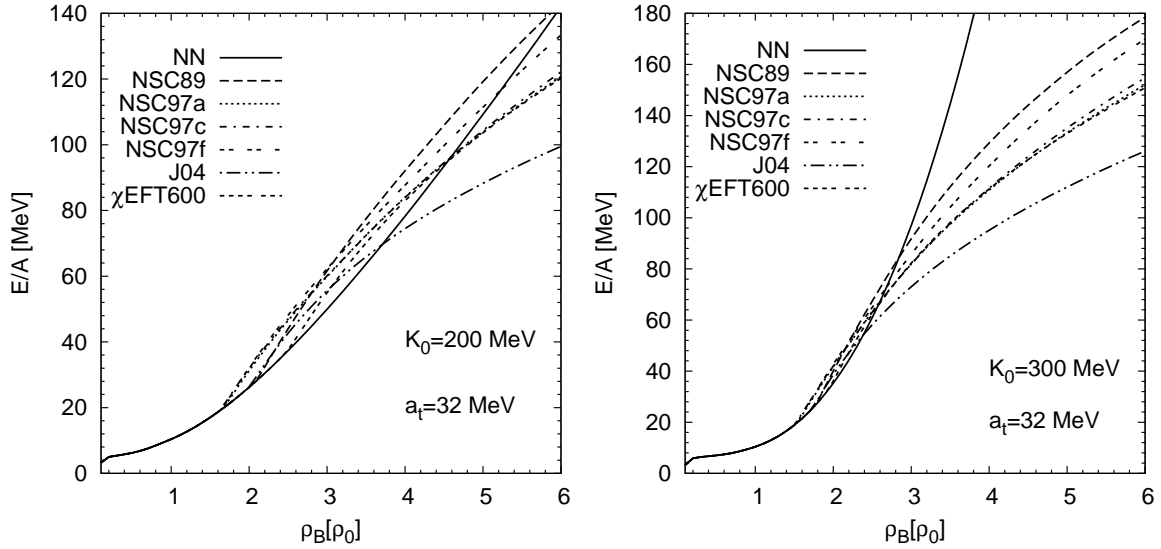
Figure 3.6: EoS for β-equilibrated matter for all models with two different values for incompressibility. The one on the left-hand side is "soft" and the one on the right-hand side is "stiff".

different YN interactions. Similarly, the threshold densities for the Λ hyperon are shown in Fig. 3.8.

In these figures one sees how the single-particle potentials for various YN interactions modify the threshold densities. In this way, the properties of the YN interaction in Fig. 2.3 and Fig. 2.5 can be attributed to the hyperon appearances.

From Fig. 3.7 one sees that the Σ^- hyperon appears in between $1.4\rho_0$ and $2.4\rho_0$ with the exception of the χEFT600 model. For almost all used YN interactions the Σ^- is the first hyperon which will appear even though the Λ hyperon is the lighter one. The reason is that the heavier mass of the Σ^- is offset by the presence of the e^- chemical potential, cf. Eq. (3.23). In general, heavier and more positively charged particles appear later. In the case of the Σ^-, compared to the Λ, the effect caused by the electric charge dominates the one coming from the mass in almost all cases.

For the Σ^- hyperon a further modification caused by the electric charge, is the influence of the symmetry energy on the threshold density because the electron chemical potential is modified by the symmetry energy. Thus, the decrease of the threshold densities due to the increase of K_0 is analogous to the decrease due to a_t.

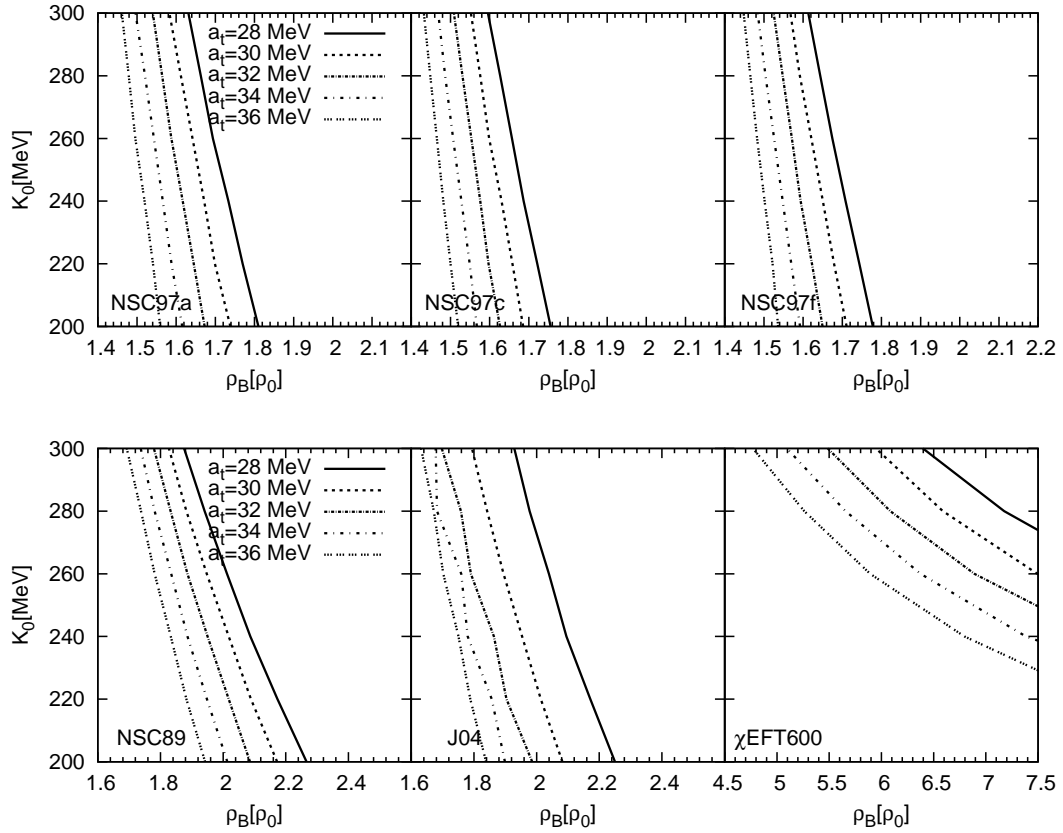For the Λ hyperon the range of threshold densities is between $1.7\rho_0$ to $4.5\rho_0$,

Figure 3.7: Threshold densities of Σ^- depending on the incompressibility and the symmetry parameter for different YN interactions.

depending on the incompressibility, symmetry energy and the used YN interaction, cf. Fig. 3.8. The influence of the incompressibility on the threshold density for this hyperon is larger than the one from the symmetry energy. This is reasonable since the incompressibility controls the rate of the energy increase with density more directly, while the symmetry energy affects only the details of the β-equilibrium. One clearly recognizes in Fig. 3.8 that the Λ appears earlier for larger incompressibilities. Thus, in general we see that for increasing incompressibilities the threshold densities decrease for both hyperons.

In contrast to the influence of K_0 and a_t, the influence of the single-particle potentials on the threshold densities is harder to analyze.

The threshold densities for the Σ^- are largest for the χEFT600 interaction since it is obtained with the most repulsive Σ^- single-particle potential. In general, hyperons will appear earlier for a more attractive single-particle potential. This becomes obvious from Eq. (3.11): the chemical potential decreases for a more negative $U_b(k_{F_b})$ and, consequently, the threshold density will also decrease.
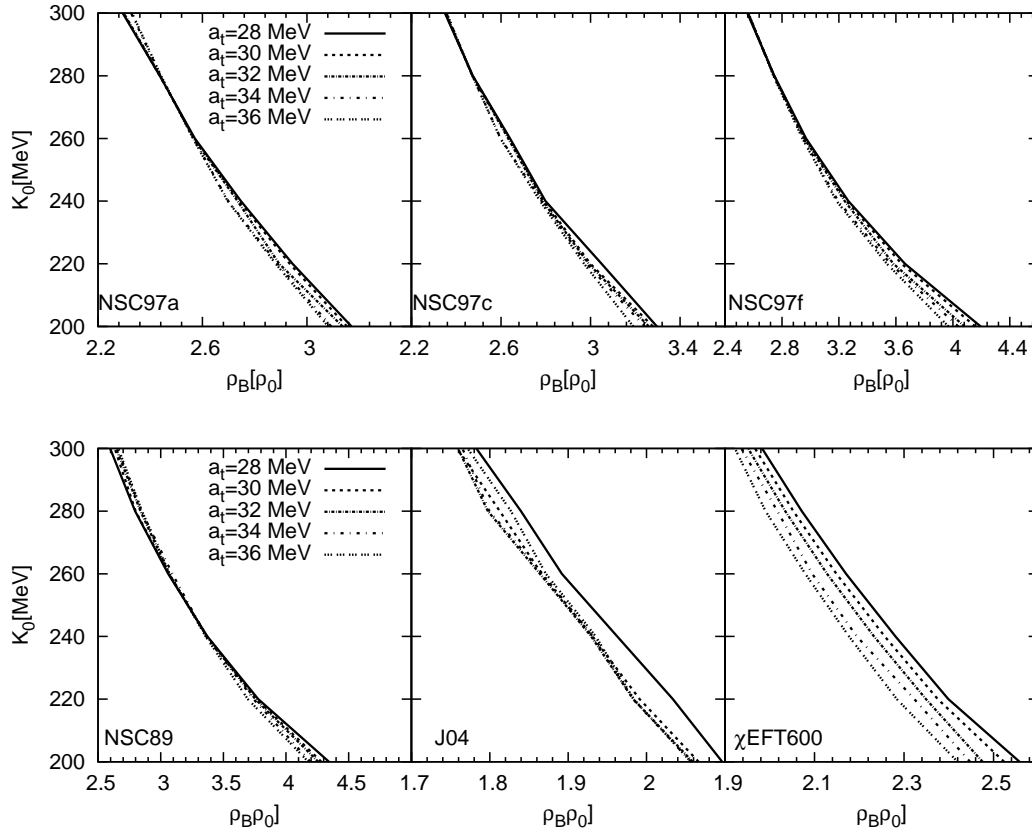
Figure 3.8: Threshold densities of Λ depending on the incompressibility and the symmetry parameter for different YN interactions.

Thus, in this way, the most repulsive single-particle potential like the one for the χEFT600 leads to the largest threshold density.

For the Λ hyperon the threshold densities are smallest for the most attractive single-particle potential obtained with the J04 model, cf. Fig. 3.8. On the other hand, they are largest for the most repulsive NSC89 interaction. For the NSC97f interaction which is in between these extrema the Λ threshold densities are very close to those of the most repulsive NSC89 one, cf. Fig. 3.8. The reason why they are so close lies in the appearance of the Σ^- hyperon. The effect is caused by the slowdown of the increase of the neutron chemical potential and is further related to the rapid increase of the Σ^- density just after its appearance, cf. Fig. 3.5. Basically, the slowdown occurs as soon as a new hyperon appears because most of the energy is used for its creation. Once the concentration of the hyperon has reached a plateau, the neutron chemical potential resumes its increase and a further hyperon might appear if the conditions for its appearance are fulfilled. Thus, the appearance of the first hyperon shifts the threshold density of the next

hyperon towards higher values. Through this mechanism a delay of the appearance of the next species of hyperons is achieved.

This effect explains why the threshold densities of the Λ are so similar for the NSC97f and NSC89 interactions. Furthermore, it also makes clear why the Λ threshold densities for the χEFT600 interaction are smaller than those of the NSC97a, NSC97c and NSC97f interactions even though their Λ single-particle potentials are almost the same, cf. Fig. 2.3.

In the case of the J04 model the above described delay mechanism becomes very interesting. For this YN interaction the Λ and Σ^- hyperon appear almost at the same density. In this case the neutron chemical potential stagnates but the Λ and the Σ^- single-particle potentials are attractive enough to compensate this effect. However the effect of a slower increase of the neutron chemical potential could be seen in the slower initial increase of the densities of hyperons as well as the later onset of the plateau. This explains why in Fig. 3.3 the $J04$ is the lowest curve.

To summarize this section, we observe that strangeness appears around $\sim 2\rho_0$ in all used YN models and parameter sets. Note, that the appearance of the first hyperon, be it the Σ^- or the Λ, cannot be further altered by taking higher YY interactions into account which have been neglected in this work. The present study in terms of the broad parameter ranges as well as the multitude of the used YN interaction models reveals that strangeness in the interior of neutron stars cannot be ignored. This will be further analyzed in the following. The results of this study where presented in [55] and similar conclusions are obtained in the Brueckner-Hartree-Fock theory [56].

3.4   Structure of neutron stars

The last statement can be further underlined by an investigation of the EoS including hyperons on neutron stars. We focus on non-rotating stars, thus ignoring any changes, caused by the rotation, on the e.g. central pressure or energy density. For a given EoS, the mass-radius relation of a NS can be determine by solving the familiar Tolman-Oppenheimer-Volkoff equation (TOV) [57]. To describe the outer crust and atmosphere of the star i.e., the region of very small baryon densities below $\rho_B < 0.001$ fm^{-3}, we have used the EoS of Baym, Pethick, and Sutherland [58], which relies on properties of heavy nuclei. For densities between 0.001 fm$^{-3} \leq \rho_B \leq 0.08$ fm^{-3}, i.e. for the inner crust, we have used the EoS of Negele and Vautherin [59] who have performed a Hartree-Fock calculation of the nuclear structure in the ground state. Details on crust properties can be found e.g. in [60, 61], while recent state-of-the-art approaches are discussed in [62].

As input for the TOV equation we need the relationship between the total

energy density and the pressure. The total energy density is obtained by adding baryonic and the leptonic contributions,

$$\frac{E_T}{\Omega} = \rho_B \frac{E}{A} + \frac{E_l}{\Omega} \, . \tag{3.29}$$

The leptonic contribution is that of a free gas and can be calculated analytically

$$\frac{E_l}{\Omega} = \frac{1}{8\pi^2} \sum_{l=e,\mu,\tau} \left[p_{F_l} \left(2\mu_l^2 - m_l^2 \right) \mu_l^2 - m_l^4 \ln \left(\frac{p_{F_l} + \mu_l}{m_l} \right) \right] \, . \tag{3.30}$$

The resulting solution of the TOV equation can then be used to compare the results of our EoS to observations of masses and radii of pulsars.

The most accurately measured masses of neutron stars are from timing observations of radio binary pulsars. These binaries include a neutron star orbiting a neutron star or a white dwarf of an ordinary main-sequence star. With sufficient observation time an astounding accuracy can be achieved. For example in the binary pulsar PSR 1913+16 the masses are measured to be 1.3867 ± 0.0002 and 1.4414 ± 0.0002 $M_\odot$ respectively [63]. It is significant to note that while double neutron star binaries have a mean mass close to the canonical 1.4 $M_\odot$, binaries with white a dwarf have a broader range of masses. Some cases have been reported where even a mass of pulsar larger than 2 $M_\odot$ was observed, but most have been refuted or are under suspicion. A recent review of neutron star observations can be found in [53].
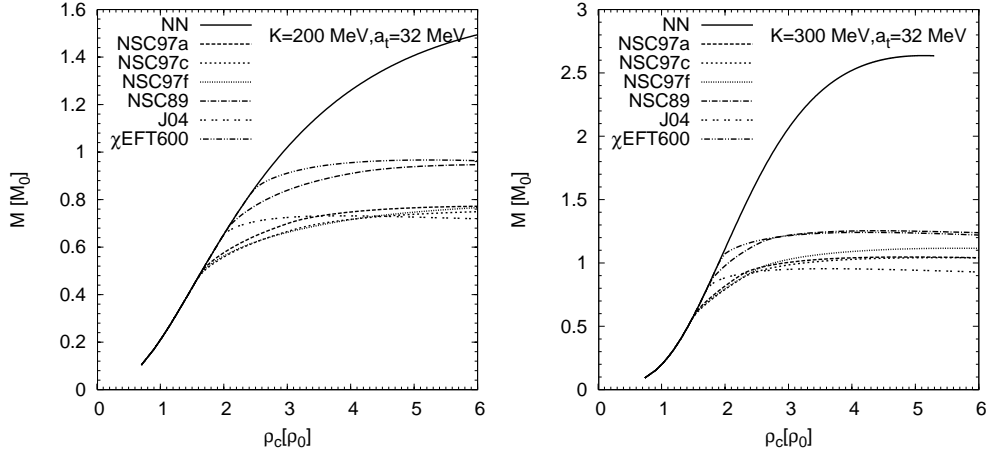

Figure 3.9: Dependence of mass of neutrons star on central density for soft EoS, shown on the left-hand side and stiff EoS on the right-hand side. The curves are shown for a symmetry energy $a_t = 32$ MeV and different YN interactions. Values of pure NN interaction is also shown.

In Fig. 3.9 we show the dependence of neutrons star masses on central density, where both baryon and lepton densities have been taken into account, for several YN interaction models and two values of K_0. The masses are given in units of solar mass and the central density in units of saturation density. The previously mentioned advantage of using the parametric equation of state in now obvious as we can see here that the maximum of neutron star mass is realized for densities above $6\rho_0$.
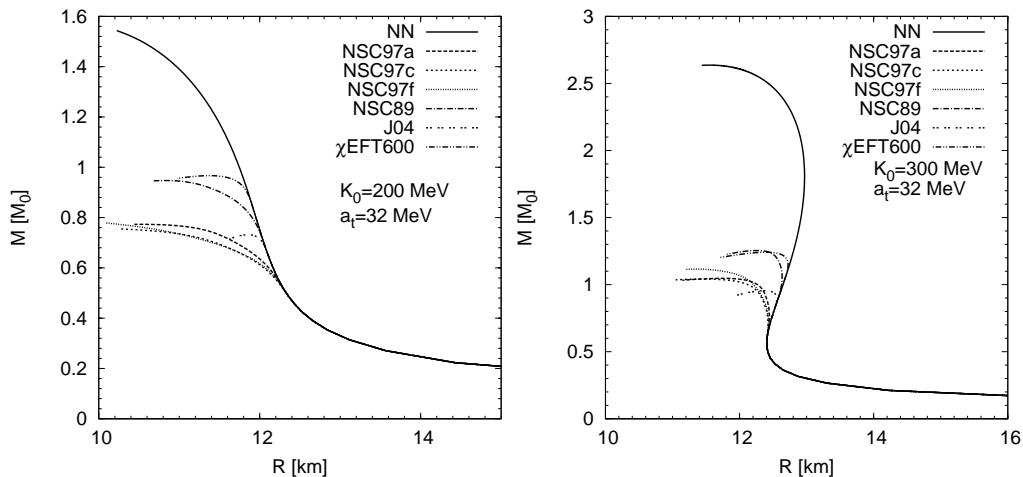

Figure 3.10: Mass-radius relation of a neutron star for a symmetry energy $a_t = 32$ MeV and different YN interactions. For comparison the mass-radius curve obtained for the pure NN interaction is also shown. Left panel: soft EoS, right panel: stiff EoS.

In Fig. 3.10 the mass-radius relation of a NS for a soft EoS (left panel) and for a stiff EoS (right panel) is shown. The symmetry energy $a_t = 32$ MeV is kept fixed in both calculations and the resulting mass-radius relation without any strangeness influence is also added for comparison.

As can be seen from Fig. 3.10 the appearance of hyperons reduces the mass of a NS drastically compared to the pure NN case. Even for larger values of the incompressibility, i.e. $K_0 = 300$ MeV, the maximum mass, obtained for all used YN interactions, is still below the canonically accepted 1.4 $M_\odot$. This is not an unusual result and is also seen in other related works such as e.g. [64, 65, 66, 67]. In general, any inclusion of further degrees of freedom will reduce the NS mass.

Furthermore, we have to keep in mind that only the YN interaction has been taken into account and if YY interactions were considered the mass-radius relation would also change. However, in order to calculate the maximum mass of a NS large densities of the order of $\sim 5\rho_0$ are needed. For these densities it is expected that the YY interaction will provide some repulsions which in turn leads to higher allowed maximum NS masses. This behavior was found in [67] where

an extensive study of Skyrme models including only the Λ hyperon reveals an increase of the maximum mass. In almost all considered cases the increase was strong enough to find maximum masses above $1.44 M_\odot$. On the other hand, if the YY interaction is attractive like in the case of [64] this will lead to smaller maximum masses. Additionally, for such high densities or hyperon concentrations higher order interactions such as the YNN, YYN and YYY interactions might also become important.

4 Landau Fermi liquid theory

Landau developed Fermi liquid theory in order to describe strongly interacting systems at low temperatures. In this theory, elementary excitations of a strongly interacting system are described by quasiparticles. If the low temperature assumption holds these quasiparticles are long-lived and interact only weakly. If we use the Fermi momentum of the system to define the ground state, all excitations above it are quasiparticles and below are quasiholes. The in-medium interaction is then used to "dress" the free particles and turn them into quasiparticles and quasiholes.

So long as these assumptions hold, we can treat the quasiparticles as the fundamental degrees of freedom which then interact with each other. Although this theory cannot describe the ground state itself, it will enable us to study excitations from it and how the medium responds to these excitations. This will lead to the concept of the response function of the medium which we will calculate microscopically. Subsequently, we can study the transport properties of the medium such as cross sections and mean free paths.

After the introduction of the Landau-Migdal parameters in Sec. 4.1 we will discuss the replacement of the three-body force with a density-dependent interaction in Sec. 4.2. In Sec. 4.2.1 we will repeat some of the results of the equation of state (EoS) and composition of matter similar to the previous chapter but now with the usage of a density-dependent interaction. In the final section, Sec. 4.3, we will show results for the Landau-Migdal parameters, mainly in symmetric matter, but also for the equilibrated matter.

4.1   Landau-Migdal parameters

A simple and instructive description of the residual interaction in homogenous infinite nuclear matter is given by the Landau interaction developed in the context of the Fermi liquid theory. Starting from the full density matrix in (relative)

momentum space $\tilde{\rho}(\vec{k}\sigma\sigma'\tau')$, the various densities are defined as [68]

$$\tilde{\rho}_{00}(\vec{k}) = \sum_{\sigma}\sum_{\tau}\tilde{\rho}(\vec{k}\sigma\tau\sigma\tau) \,, \tag{4.1}$$

$$\tilde{\rho}_{1t_3}(\vec{k}) = \sum_{\sigma}\sum_{\tau\tau'}\tilde{\rho}(\vec{k}\sigma\tau\sigma\tau')\tau^{t_3}_{\tau\tau'} \,, \tag{4.2}$$

$$\tilde{\vec{s}}_{00}(\vec{k}) = \sum_{\sigma\sigma'}\sum_{\tau}\tilde{\rho}(\vec{k}\sigma\tau\sigma'\tau)\vec{\sigma}_{\sigma\sigma'} \,, \tag{4.3}$$

$$\tilde{\vec{s}}_{1t_3}(\vec{k}) = \sum_{\sigma\sigma'}\sum_{\tau\tau'}\tilde{\rho}(\vec{k}\sigma\tau\sigma'\tau')\vec{\sigma}_{\sigma\sigma'}\tau^{t_3}_{\tau\tau'} \,, \tag{4.4}$$

where the $\tilde{\rho}(\vec{k}\sigma\tau\sigma'\tau')$ is the density matrix defined in [68] and references therein. The quantities σ and τ are the spin and isospin coordinates of the wave function while $\vec{k}$ is its momentum. The quantities $\vec{\sigma}_{\sigma\sigma'}$ and $\tau^{t_3}_{\tau\tau'}$ are matrix elements of the Pauli matrices in spin and isospin space. The Landau-Migdal interaction is defined as

$$\begin{aligned}\tilde{V}(\vec{k}_1\sigma_1\tau_1\sigma_1'\tau_1'; \vec{k}_2\sigma_2\tau_2\sigma_2'\tau_2') &= \frac{\delta^2\mathcal{V}}{\delta\tilde{\rho}(\vec{k}_1\sigma_1\tau_1\sigma_1'\tau_1')\delta\tilde{\rho}(\vec{k}_2\sigma_2\tau_2\sigma_2'\tau_2')} \\ &= \tilde{f}(\vec{k}_1,\vec{k}_2) + \tilde{f}'(\vec{k}_1,\vec{k}_2)\vec{\tau}_1\cdot\vec{\tau}_2 + \tilde{g}(\vec{k}_1,\vec{k}_2)\vec{\sigma}_1\cdot\vec{\sigma}_2 + \tilde{g}'(\vec{k}_1,\vec{k}_2)(\vec{\sigma}_1\cdot\vec{\sigma}_2)(\vec{\tau}_1\cdot\vec{\tau}_2) \,, \end{aligned}\tag{4.5}$$

where $\mathcal{V}$ is the potential part of the energy per particle. The isoscalar-scalar, isovector-scalar, isoscalar-vector, and isovector-vector channels of the residual interaction are given by

$$\tilde{f}(\vec{k}_1,\vec{k}_2) = \frac{\delta^2\mathcal{V}}{\delta\tilde{\rho}_{00}(\vec{k}_1)\delta\tilde{\rho}_{00}(\vec{k}_2)} \,, \tag{4.6}$$

$$\tilde{f}'(\vec{k}_1,\vec{k}_2) = \frac{\delta^2\mathcal{V}}{\delta\tilde{\rho}_{1t_3}(\vec{k}_1)\delta\tilde{\rho}_{1t_3}(\vec{k}_2)} \,, \tag{4.7}$$

$$\tilde{g}(\vec{k}_1,\vec{k}_2) = \frac{\delta^2\mathcal{V}}{\delta\tilde{\vec{s}}_{00}(\vec{k}_1)\delta\tilde{\vec{s}}_{00}(\vec{k}_2)} \,, \tag{4.8}$$

$$\tilde{g}'(\vec{k}_1,\vec{k}_2) = \frac{\delta^2\mathcal{V}}{\delta\tilde{\vec{s}}_{1t_3}(\vec{k}_1)\delta\tilde{\vec{s}}_{1t_3}(\vec{k}_2)} \,. \tag{4.9}$$

Assuming that only states at the Fermi surface contribute, $\tilde{f}, \tilde{f}', \tilde{g}$ and $\tilde{g}'$ depend only on the angle θ between $\vec{k}_1$ and $\vec{k}_2$, and can be expanded in Legendre polynomials, e.g.

$$\tilde{f}(\vec{k}_1,\vec{k}_2) = \frac{1}{N_0}\sum_{l=0}^{\infty}\tilde{F}_l P_l(\cos\theta) \,. \tag{4.10}$$

The coefficient $\tilde{F}_l$ is called the Landau coefficient. Other Landau coefficients appear in the expansion of the other channels, so we also have $\tilde{F}'_l$ in the expansion of $\tilde{f}'$, $\tilde{G}_l$ in the expansion of $\tilde{g}$ and $\tilde{G}'_l$ in the expansion of $\tilde{g}'$. The normalization factor N_0 representing the level density at the Fermi surface is given by,

$$N_0 = \frac{2M^* k_F}{\pi^2} \, , \tag{4.11}$$

for a two-component system. It is used to make the Landau coefficient dimensionless.

If we now apply the orthogonality relations for Legendre polynomials,

$$\int_{-1}^{1} P_l(x) P_{l'}(x) dx = \frac{2}{2l+1} \delta_{ll'} \, , \tag{4.12}$$

we obtain

$$\tilde{F}_l = \frac{2l+1}{2} N_0 \int_{-1}^{1} d(\hat{\vec{k}}_1 \cdot \hat{\vec{k}}_2) P_l(\hat{\vec{k}}_1 \cdot \hat{\vec{k}}_2) \tilde{f}(\vec{k}_1, \vec{k}_2) \, , \tag{4.13}$$

where $\hat{\vec{k}} = \vec{k}/|\vec{k}|$.

Since we are studying infinite nuclear matter we can choose pure neutron and proton states, which leads to $\tilde{\rho}_{1,\pm 1} = 0$ and $\rho_t = \tilde{\rho}_{10}$ and similarly for all other densities. This means that we can keep only the diagonal elements of the density matrix and we have

$$\rho(\vec{k}) = \rho_{p\uparrow} + \rho_{p\downarrow} + \rho_{n\uparrow} + \rho_{n\downarrow} \, , \tag{4.14}$$

$$\rho_s(\vec{k}) = \rho_{p\uparrow} - \rho_{p\downarrow} + \rho_{n\uparrow} - \rho_{n\downarrow} \, , \tag{4.15}$$

$$\rho_t(\vec{k}) = \rho_{p\uparrow} + \rho_{p\downarrow} - \rho_{n\uparrow} - \rho_{n\downarrow} \, , \tag{4.16}$$

$$\rho_{st}(\vec{k}) = \rho_{p\uparrow} - \rho_{p\downarrow} - \rho_{n\uparrow} + \rho_{n\downarrow} \, , \tag{4.17}$$

and

$$f(\vec{k}_1, \vec{k}_2) = \frac{\partial^2 \mathcal{V}}{\partial \rho(\vec{k}_1) \partial \rho(\vec{k}_2)} \, , \tag{4.18}$$

$$f'(\vec{k}_1, \vec{k}_2) = \frac{\partial^2 \mathcal{V}}{\partial \rho_t(\vec{k}_1) \partial \rho_t(\vec{k}_2)} \, , \tag{4.19}$$

$$g(\vec{k}_1, \vec{k}_2) = \frac{\partial^2 \mathcal{V}}{\partial \rho_s(\vec{k}_1) \partial \rho_s(\vec{k}_2)} \, , \tag{4.20}$$

$$g'(\vec{k}_1, \vec{k}_2) = \frac{\partial^2 \mathcal{V}}{\partial \rho_{st}(\vec{k}_1) \partial \rho_{st}(\vec{k}_2)} \, . \tag{4.21}$$

For the dimensionless Landau Fermi liquid parameters we have

$$F_l = \frac{2l+1}{2} N_0 \int_{-1}^{1} d(\hat{\vec{k}}_1 \cdot \hat{\vec{k}}_2) P_l(\hat{\vec{k}}_1 \cdot \hat{\vec{k}}_2) f(\vec{k}_1, \vec{k}_2) \,. \qquad (4.22)$$

The effective mass M^* for symmetric nuclear matter can be calculated via Eq. (2.12). For an isotropic system, Landau showed that [69]

$$\frac{M^*}{M} = 1 + \frac{F_1}{3} \,, \qquad (4.23)$$

by using Galilean invariance, where M is the free mass. The parameter F_1 is the second coefficient in the Legendre expansion of the isoscalar-scalar channel of the residual interaction.

The Landau-Migdal approximation is often used in connection with RPA calculations because it greatly simplifies the calculation of the RPA response function. The approximation consists of assuming that the interacting particles and holes are on the Fermi surface and that the interaction takes place only in the limit where the transferred momentum $q = 0$. Thus it is obvious that this approximation is only valid for small q. For this purpose we will also introduce the Landau-Migdal parameters, in addition to the Landau Fermi liquid parameters that we have introduced thus far. It will become clear in the next chapter why we need these parameters [70].

The Landau-Migdal parameters are defined as follows

$$f^{\tau\sigma\,\tau'\sigma'}(\vec{k}_1, \vec{k}_2) = \frac{\partial^2 \mathcal{V}}{\partial\rho_{\tau\sigma}(\vec{k}_1)\partial\rho_{\tau'\sigma'}(\vec{k}_2)} \,, \qquad (4.24)$$

and can, in the Hartree-Fock approximation, be easily connected to the direct and exchange terms of the interaction

$$\begin{aligned} f^{\tau\sigma\,\tau'\sigma'}(\vec{k}_1, \vec{k}_2) = & \left\langle \vec{k}_1\tau\sigma; \vec{k}_2\tau'\sigma' \right| V \left| \vec{k}_1\tau\sigma; \vec{k}_2\tau'\sigma' \right\rangle \\ & - \left\langle \vec{k}_1\tau\sigma; \vec{k}_2\tau'\sigma' \right| V \left| \vec{k}_2\tau'\sigma'; \vec{k}_1\tau\sigma \right\rangle \,. \end{aligned} \qquad (4.25)$$

The connection between the residual interaction channels and Landau-Migdal parameters is quite obvious and straightforward. For the isoscalar-scalar channel we have

$$f(\vec{k}_1, \vec{k}_2) = \sum_{\substack{\tau_\sigma \tau'_{\sigma'}}} f^{\tau\sigma\,\tau'\sigma'}(\vec{k}_1, \vec{k}_2) \frac{\rho_{\tau\sigma}(\vec{k}_1)}{\rho(\vec{k})} \frac{\rho_{\tau'\sigma'}(\vec{k}_2)}{\rho(\vec{k})} \,. \qquad (4.26)$$

The same connection can be established for all other channels with the aid of the inverse of the relationships Eq. (4.14)-Eq. (4.17) and the expressions Eq.

(4.18)-Eq. (4.21). Additionally, the connection between the Landau Fermi liquid parameters and the Landau-Migdal parameters can easily be established.

We can also define both zeroth and higher order Landau-Migdal parameters, in a similar fashion as in Eq. (4.13):

$$f_l^{\tau\sigma\tau'\sigma'}(k_1, k_2) = \frac{2l+1}{2} \int_{-1}^{1} d(\hat{\vec{k}}_1 \cdot \hat{\vec{k}}_2) P_l(\hat{\vec{k}}_1 \cdot \hat{\vec{k}}_2) \frac{\partial^2 \mathcal{V}}{\partial \rho_{\tau\sigma}(\vec{k}_1)\partial\rho_{\tau'\sigma'}(\vec{k}_2)} \, . \qquad (4.27)$$

In the case of unpolarized nuclear matter, we will suppress the spin indices and use a simplified notation such that:

$$f_l^{\tau\tau'}(k_1, k_2) = f_l^{\tau\sigma\tau'\sigma'}(k_1, k_2) \, . \qquad (4.28)$$

Unlike the Landau Fermi liquid parameters, the Landau-Migdal parameters are not dimensionless but have the dimension $[\text{MeV}^{-2}]$ in natural units.

The calculation of the effective mass has to be extended in the case of asymmetric nuclear matter to allow for different masses of different particles. Since we have already defined the Landau-Migdal parameters, we can use them and define the effective mass in a similar fashion to Eq. (4.23) [69]:

$$\frac{M_p^*}{M} = 1 + \frac{1}{3}F_1^p \, , \qquad (4.29)$$

$$\frac{M_n^*}{M} = 1 + \frac{1}{3}F_1^n \, , \qquad (4.30)$$

where

$$F_l^p = N_0^p \left(f_l^{pp} + (k_n/k_p)^2 f_l^{pn} \right) \, , \qquad (4.31)$$

$$F_l^n = N_0^n \left(f_l^{nn} + (k_p/k_n)^2 f_l^{pn} \right) \, . \qquad (4.32)$$

Here we have introduced the proton and neutron density of states via

$$N_0^p = \frac{M_p^* k_p}{\pi^2}, \qquad N_0^n = \frac{M_n^* k_n}{\pi^2} \, . \qquad (4.33)$$

In addition to the connection between the effective mass and the Landau Fermi liquid parameters there are other connections between these parameters and properties of nuclear matter. For the incompressibility in symmetric matter, we have

$$K = \frac{3k_F^2}{M^*}(1 + F_0) \, , \qquad (4.34)$$

and the symmetry energy is

$$a_t = \frac{k_F^2}{6M^*}(1 + F_0') \, . \qquad (4.35)$$

4.2   Density-dependent force

Just as in the previous chapter, we supplement the NN interaction with effects which come from higher many-body forces. Unfortunately, the parametric EoS of the previous chapter has only a limited applicability. The major limit is that we are unable to disentangle the momentum dependence of the original potential (i.e. we cannot take the second derivative with respect to momentum). In order to be able to do this and reproduce the properties of nuclear matter, we need to introduce a microscopic potential which mimics the effect of higher-order contributions, primarily the three-body force. This potential is than combined with the two-body effective force (i.e. $V_{\text{low k}}$ and V_{UCOM}) and its parameters are fitted to reproduce the properties of nuclear matter at saturation, such as the saturation density, binding energy, incompressibility and symmetry energy. For this purpose we use a density-dependent Yukawa-like force [71]:

$$V_{DD}(q) = \alpha_1 \hat{\rho}^{\lambda_1} \frac{\mu_1^2}{q^2 + \mu_1^2} + \alpha_2 \hat{\rho}^{\lambda_2} \frac{\mu_2^2}{q^2 + \mu_2^2}(\vec{\tau}_1 \cdot \vec{\tau}_2) + \alpha_3 \hat{\rho}^{\lambda_3} \frac{\mu_3^2}{q^2 + \mu_3^2} \,, \qquad (4.36)$$

where τ is the Pauli matrix acting in isospin space, q is the transferred momentum between in and out states and $\hat{\rho} = \rho/\rho_0$. The range parameters of the density-dependent force are $\mu_1 = \mu_2 = 1.42$ fm^{-1}, $\mu_3 = 2.5$ fm^{-1}. The matrix elements of the density-dependent force in the plane-wave basis can be found in [72].

	$V_{\text{low k}} + DDa$	$V_{\text{low k}} + DDb$	$V_{UCOM} + DDa$	$V_{UCOM} + DDb$
λ_1	0.08	0.10	0.05	0.12
λ_2	0.08	0.10	0.05	0.12
λ_3	0.20	0.65	0.20	0.65
$\alpha_1[\text{fm}^2]$	-2089.98	-529.90	-1311.91	-498.13
$\alpha_2[\text{fm}^2]$	202.64	99.74	86.51	31.68
$\alpha_3[\text{fm}^2]$	2753.12	1347.86	1798.65	1190.37
$K_0[\text{MeV}]$	240	300	240	300

Table 4.1: Table of coefficients for the nuclear potential V_{DD} (cf. [71] and [73])

In general we will favor the DDa version of the density-dependent force to DDb. We do this because the incompressibility value of 300 MeV is considered too large and the value of 240 MeV is favored as being closer to the actual physical value. However for some of the results we will also show the DDb parametrization as well for the sake of comparison.

4.2.1   Equation of state

As in the previous chapter we need to satisfy the conditions of the β-equilibrium in order to calculate the EoS of equilibrated matter. Thus, we again use Eq. (3.21) and Eq. (3.22). As for the chemical potential in this case there is no need to substitute anything, like in the previous chapter, so we use Eq. (3.12) and Eq. (3.11) in their unmodified form. Once we determine the β-equilibrium we use Eq. (3.3) to calculate the energy per particle.

One significant difference, compared to the previous chapter is the introduction of a non-zero temperature through Eq. (3.13). This also means that we have to modify Eq. (3.3) such that we have

$$E/A = \frac{2}{\rho_B} \sum_b \int_0^\infty \frac{d^3\vec{p}}{(2\pi)^3} \left(M_b + \frac{p^2}{2M_b} + \frac{1}{2} U_b(\vec{p}) \right) \frac{1}{1 + \exp\left((\epsilon_b - \mu_b)/T \right)}, \quad (4.37)$$

where ϵ_b is given by:

$$\epsilon_b(\vec{p}) = M_b + \frac{p^2}{2M_b} + U_b(\vec{p}). \quad (4.38)$$

Fig. 4.1 shows the particle concentrations for the various hyperon interactions in combination with the NN-model $V_{\text{low k}} + DDa$ at zero temperature. As for similar figures in the previous chapter we see how sharp the appearance of the hyperons is, i.e. how quickly their concentration rises initially after their appearance. Here again we see that the first hyperon appears around $\sim 2\rho_0$ and how the appearance of Σ^- lowers the concentration of negatively charged leptons. In essence, all of the behavior of hyperon appearance and concentration remains similar to that of the parametric EoS with the same K_0.

As already mentioned, the usage of $V_{\text{low k}}$ imposes a restriction on the allowed density range. In the case of β-equilibrated matter with only protons and neutrons and no hyperons it would be $\sim 4\rho_0$. However the introduction of hyperons lowers the Fermi momentum of the neutrons sufficiently to make the calculation possible up to $\sim 5\rho_0$. Additionally the smoothness of the curves indicates that there are no artifacts due to the sharp cut-off in this calculation.

Like Fig. 4.1, Fig. 4.2 shows the particle concentrations for all hyperon interactions in combination with the NN-model $V_{\text{low k}} + DDa$, but now at a temperature of $T = 10$ MeV. While most of the features of these two figures are the same, there are several notable differences which are to be expected. The biggest one is that the density at which hyperons appear is shifted to lower values and for most models we already have a small amount of hyperons at saturation density. The other noticeable effect is a significantly slower rate of increase of the hyperon densities in the initial stages of their appearance.
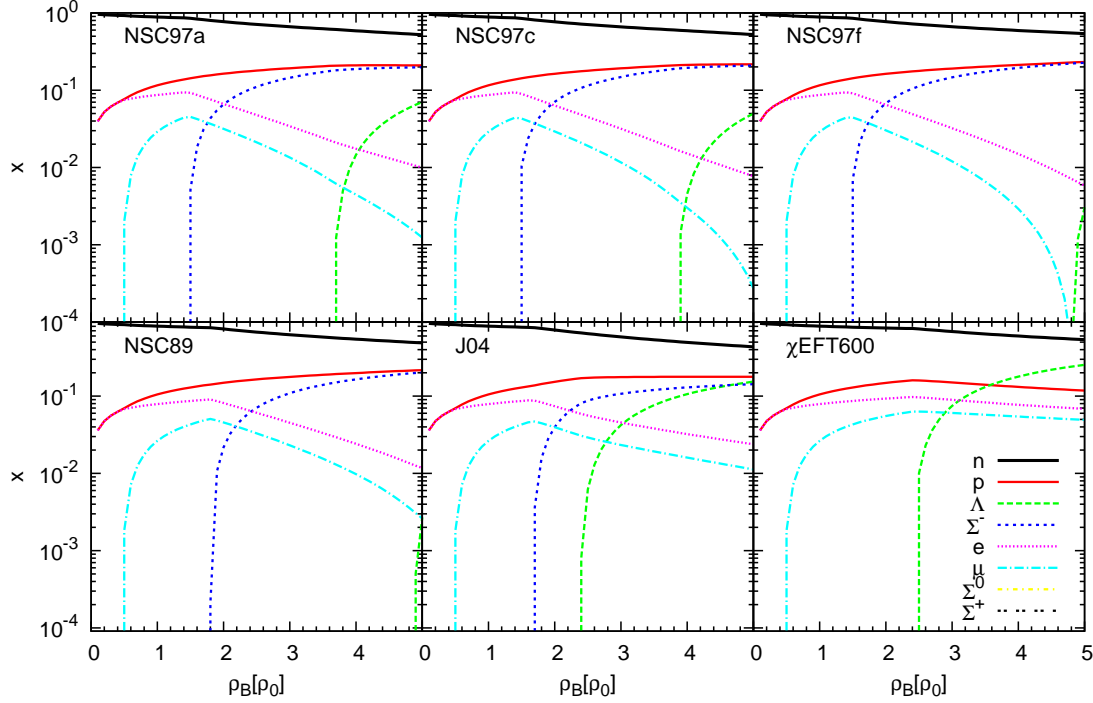
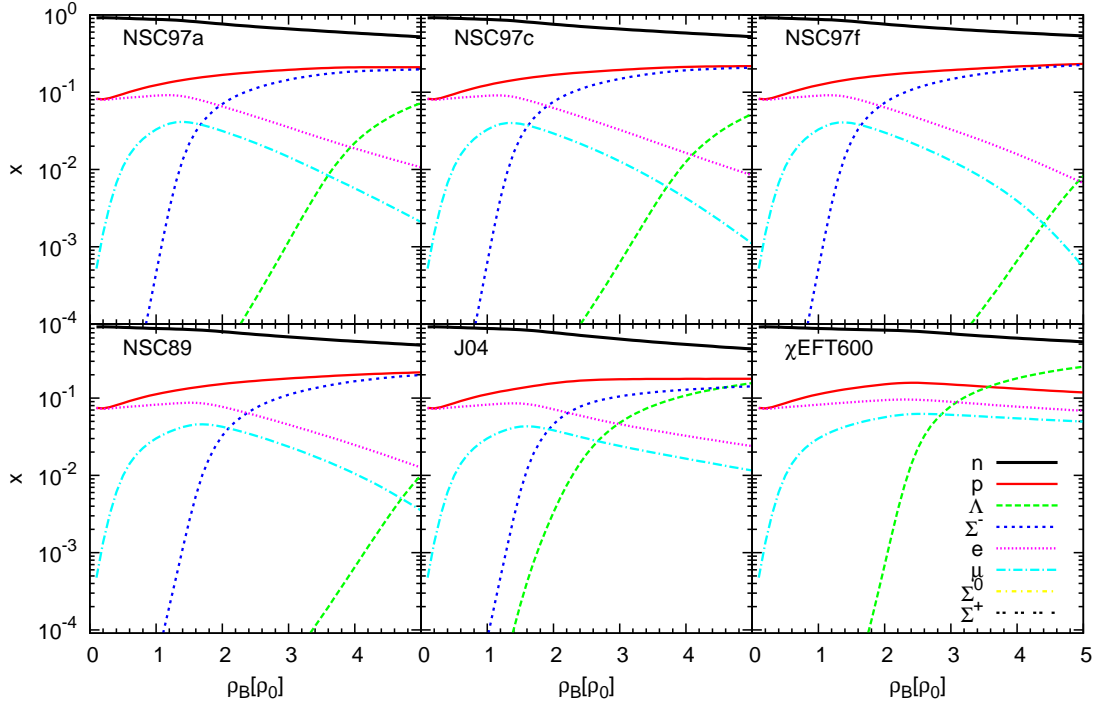Figure 4.1: Composition of matter at $T = 0$ MeV for several hyperon interactions with $V_{\text{low k}} + DDa$.

With the composition of matter fixed, we can now move on to the calculation of the EoS in the equilibrium. Fig. 4.3 shows the EoS for the $V_{\text{low k}} + DDa$ (upper panels) and $V_{UCOM} + DDa$ (lower panels). It also displays the EoS for two different temperatures: $T = 0$ MeV on the right and $T = 10$ MeV on the left. The concentrations of hyperons are not shown for $V_{UCOM} + DDa$ since they are similar to those of $V_{\text{low k}} + DDa$.

Once again the appearance of hyperons is evident in the deviation of the curves from the ones without any hyperons. We also notice the softening of the EoS at higher densities as the hyperons are introduced. This is the same result which we had for the parametric EoS so it is reasonable to conclude that the effect of the reduction of the maximum of the neutron stars mass are the same here, even though we cannot calculate them in this case.

As for the effects of the non-zero temperature, it is clear from Fig. 4.3 that they are present at lower densities and strongest at the very beginning of the curves. However, as the density increases the influence of temperature becomes smaller

Figure 4.2: Composition of matter at $T = 10$ MeV for several hyperon interactions with $V_{\text{low k}} + DDa$.

and by the end of the curves it is practically impossible to tell the difference between the two temperatures. This observation is easily explainable if we note that the Fermi momentum of the particles increases with density, as does the Fermi energy. As the Fermi energy increases the ratio between the system temperature and it decreases. By the time the density reaches values of $\sim 4\rho_0$, for a system temperature of $T = 10$ MeV, this ratio is close to zero. Hence at such densities we can neglect even the temperature of $T = 10$ MeV. Therefore in order see an effect at high densities one would have to increase the temperature to levels which are not expected to be found even in newly born neutron stars.

4.3 Results

In this section we will show results for the Landau-Migdal parameters. Although one finds the Landau Fermi liquid parameters more often in the literature than the Landau-Migdal parameters, we show the latter as well. We do this because
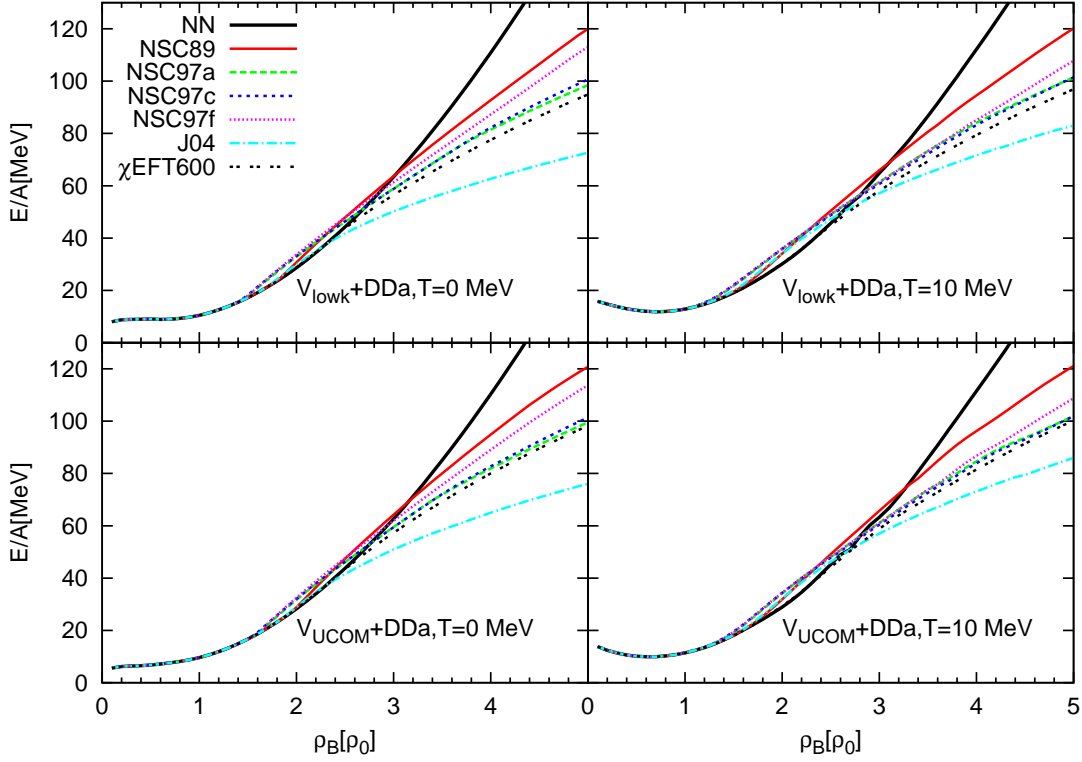
Figure 4.3: Equations of state for microscopic interactions with hyperons. Upper panels are with $V_{\text{low k}} + DDa$ and lower with $V_{UCOM} + DDa$ while for the left panels we have $T = 0$ MeV for the right we have $T = 10$ MeV.

they serve as an input for the calculations within the framework of the RPA which we will perform in the next chapter.

Most of the figures display results for symmetric matter, because there are only a few differences compared to the results in β-equilibrium. Since the Landau-Migdal parameters do not depend directly on the temperature we will not show any of the results for non-zero temperatures, even though β-equilibrium indirectly introduces a dependence on temperature. However in the next chapter we perform our calculation consistently and use the appropriate parameters as input.
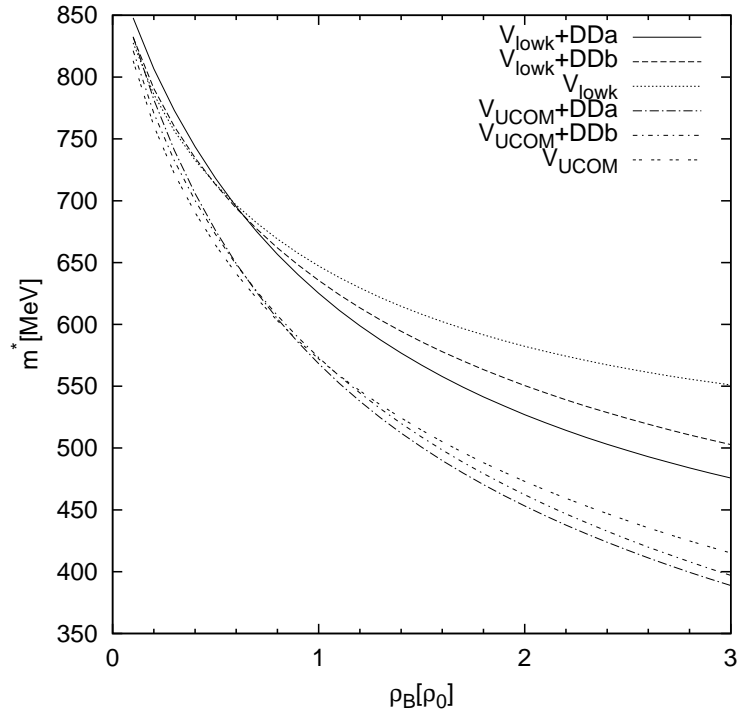
Figure 4.4: The effective mass of nucleons in symmetric nuclear matter.

4.3.1 Symmetric matter

Fig. 4.4 shows the effective mass of nucleons in symmetric nuclear matter; the values for several interaction are shown. The figure clearly shows how the in-medium mass of nucleons decreases with density, confirming that the NN interaction is indeed attractive. As expected, as the nucleons become more tightly packed they attract each other more strongly, thus continuously decreasing the effective mass as the density increases. It is interesting to note that the effects of the density-dependent force are not large in the case of the effective mass and that there is a larger difference due to differences in the microscopic two-body interactions. Additionally it is evident that these two-body interactions produce an effective mass value at saturation density which is in the usual range of expected values.

The density dependence of the Landau Fermi liquid parameters F_0, F_0', G_0 and G_0' in symmetric nuclear matter is shown in Fig. 4.5. As expected, F_0, representing the central part of the force, is usually the most dominant. For values below -1 the system becomes unstable under density oscillations. One expects that at densities where $F_0 \leq -1$ the approximations underlying nuclear matter start to
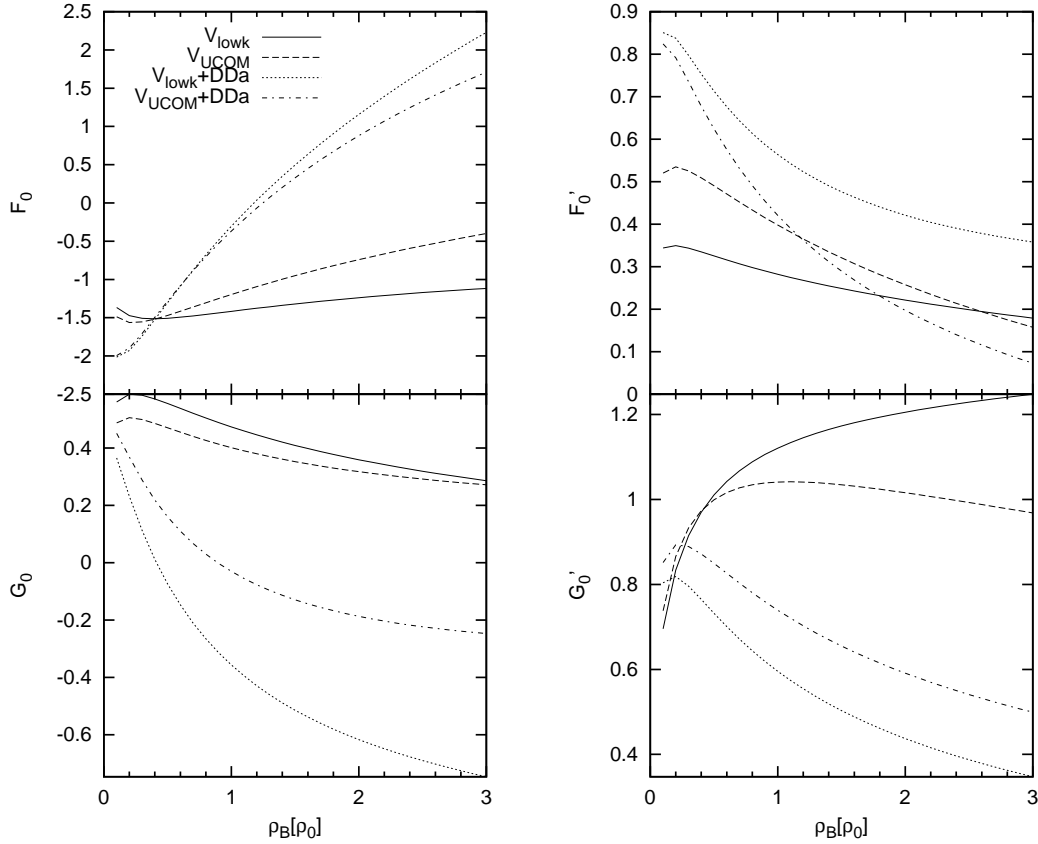
Figure 4.5: Landau Fermi liquid parameters in symmetric nuclear matter for $l = 0$.

breakdown and the nucleons start to form nuclei. Evidently the $V_{\text{low k}}$ without any density dependent force is never above -1, while for the V_{UCOM} the stability is reached at $\sim 1.5\rho_0$. For the corrected potentials, the usual value of $\sim 0.6\rho_0$ in symmetric nuclear matter is obtained. The ferromagnetic instability, $G_0 \leq -1$, which is observed in Skyrme models [5, 67] does not occur in any of our models.

Fig. 4.6 shows the density dependence of the Landau parameters F_1, F_1', G_1 and G_1' in symmetric nuclear matter. The most important of them, F_1, closely mimics the behavior of the effective mass which it is connected to through Eq. (4.23). Like in the case of the effective mass we observe that the influence of the density-dependent force is not large. As for the remaining parameters, very little reliable information exists about them which makes them difficult to interpret. As expected, all of the $l = 1$ parameters are, for the most part, smaller than their corresponding $l = 0$ parameter and while it is also possible to calculate the Landau Fermi liquid parameters with larger l from Eq. (4.22), they would be even
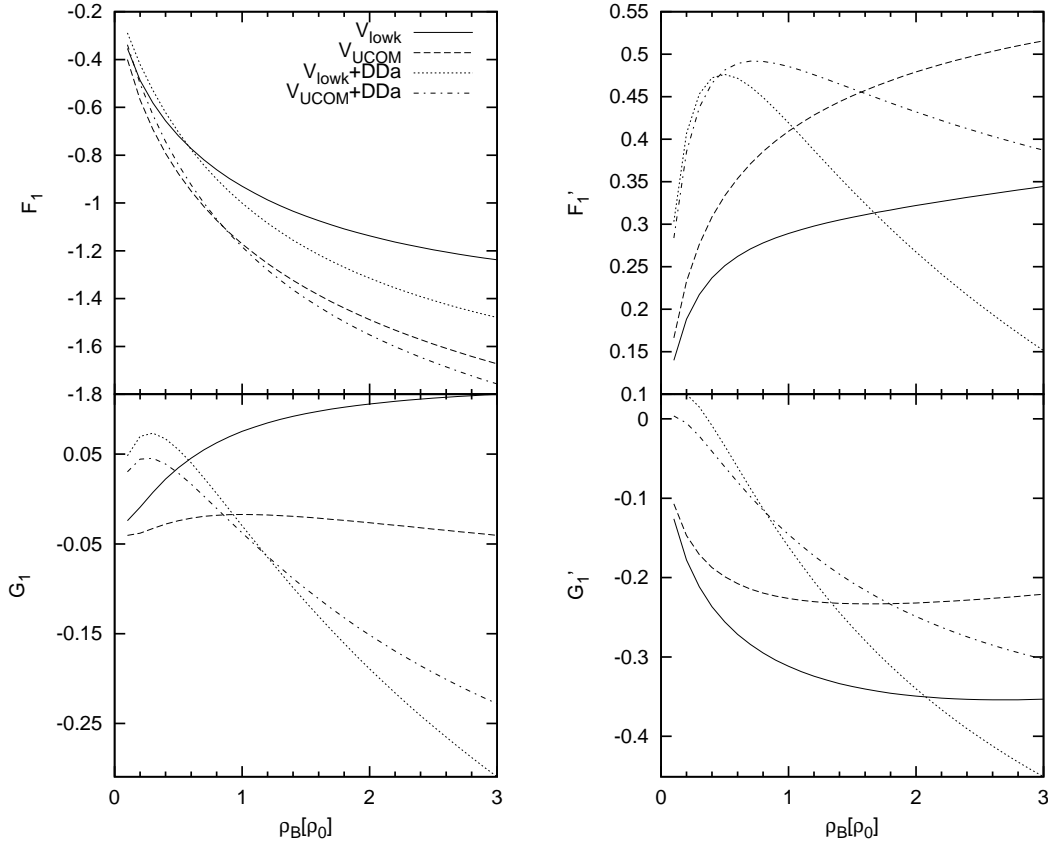
Figure 4.6: Landau Fermi liquid parameters in symmetric nuclear matter for $l = 1$.

smaller and thus contribute less.

Fig. 4.7 and Fig. 4.8 show the density dependence of the Landau-Migdal parameters in symmetric nuclear matter. The values for the neutron-neutron interactions are not shown since they are identical to those of the proton-proton interaction. The reason for this lies in the fact that we have neglected the electromagnetic force which leaves only the strong force to consider.

In the left column of Fig. 4.7 and Fig. 4.8, f_{pp} and f_{pn}, represent the spin-independent interaction while those on the right side, g_{pp} and g_{pn}, represent the spin-dependent interaction. One should also keep in mind that in reality these parameters do not represent the particle-particle interactions but are in-fact indicative of the in-medium particle-hole interaction. Thus, for f_{pp} (g_{pp}) we are in-fact showing the strength of the interaction between two pp^{-1} states with like (unlike) spins, while f_{pn} (g_{pn}) indicates the matrix elements between nn^{-1} and pp^{-1} states with like (unlike) spins.
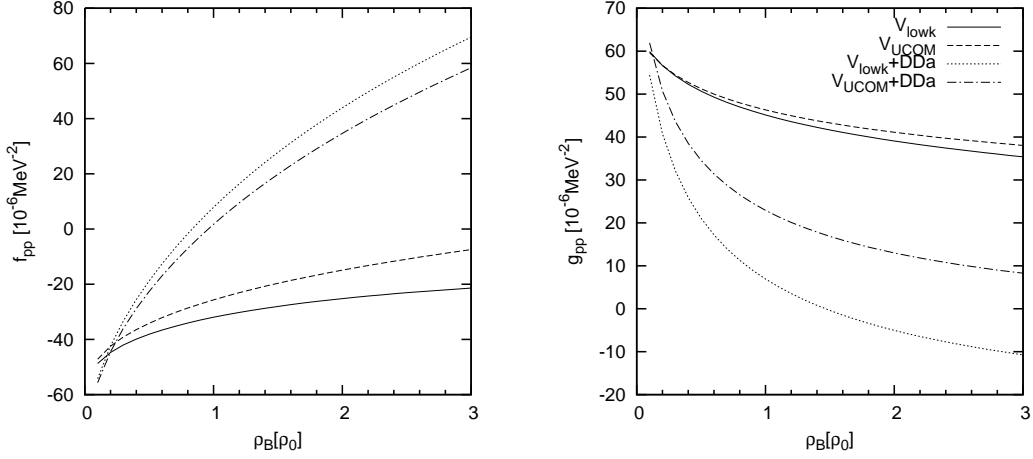
Figure 4.7: Landau-Migdal parameters in symmetric nuclear matter describing the proton-proton interaction.
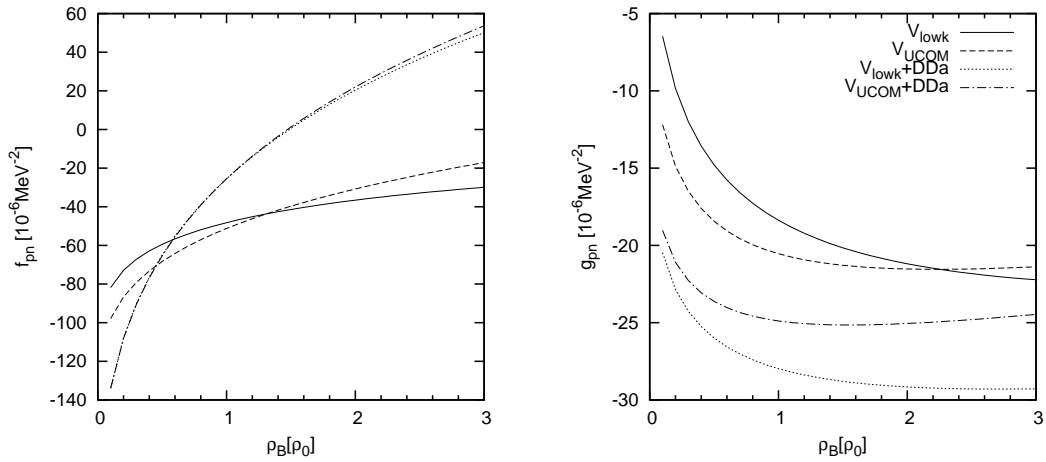

Figure 4.8: Landau-Migdal parameters in symmetric nuclear matter describing the proton-neutron interaction.

Hyperon-Nucleon Landau-Migdal parameters

Just as for the NN interaction, one can introduce Landau-Migdal parameters for hyperons Eq. (4.27). The only difference is that the isospin can take more values.

The generalization of Eq. (4.27) is straightforward. In the case of symmetric matter we can calculate these hyperon Landau-Migdal parameters if we use Eq. (4.25) where the momentum of the hyperon is set to zero.

We have chosen to show only the symmetric matter results, again because the results in β-equilibrium are not very different. Additionally, in symmetric matter these parameters are not influenced by the NN interaction in any way and even in equilibrated matter they are only weakly dependent on them.
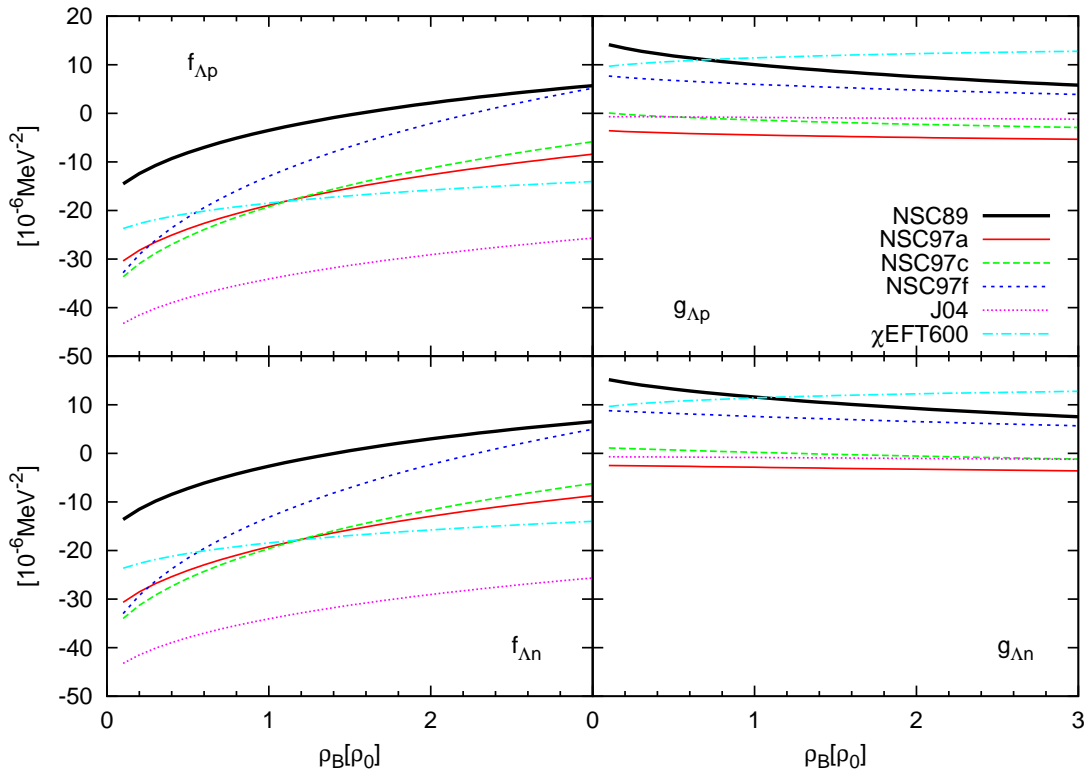
Figure 4.9: Λ Landau-Migdal parameters in symmetric nuclear matter.

In this section we will show the results only for the YN combinations, because we do not use a YY interaction. In the next chapter we will take all such YY combinations as being equal to zero. Like in the case of pn these YN combinations indicate the matrix elements between NN^{-1} states and YY^{-1} state with like (unlike) spins. Thus we have $f_{\Lambda p}$ ($g_{\Lambda p}$) describing in-medium particle-hole interactions between pp^{-1} and $\Lambda\Lambda^{-1}$ states with like (unlike) spins, etc.

Fig. 4.9 to Fig. 4.12 show all YN combinations of the hyperon Landau-Migdal

parameters. (Fig. 4.9 is devoted to the Λ, Fig. 4.10 to the Σ^-, Fig. 4.11 to
the Σ^0 and Fig. 4.11 to the Σ^+.) It is evident (and expected) that several of
these combinations are equal to each other in symmetric matter. So we have
(in symmetric matter) $f_{\Lambda p} = f_{\Lambda n}$, $f_{\Sigma^0 p} = f_{\Sigma^0 n}$, $f_{\Sigma^- p} = f_{\Sigma^+ n}$ and $f_{\Sigma^- n} = f_{\Sigma^+ p}$,
and there are analogous relations for the $g's$. The reason is merely the isospin
independence of strong interactions. Small differences, which are hard to notice
in these figures, are present due to the different masses of these particles.
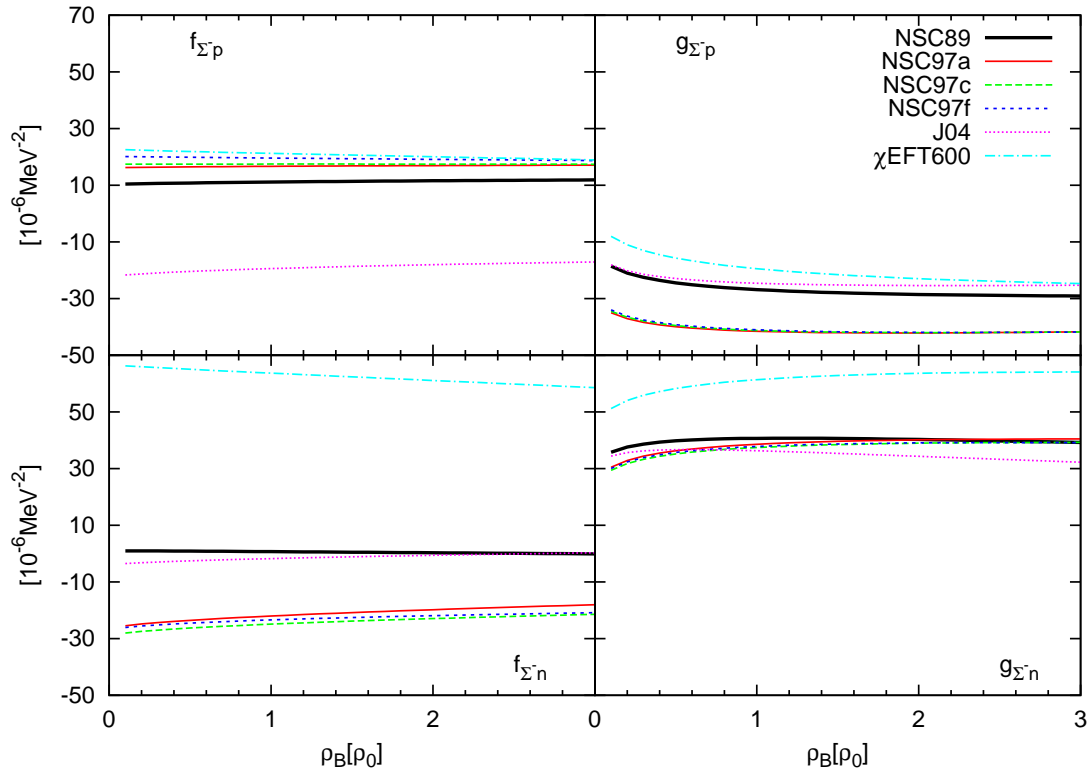
Figure 4.10: Σ^- Landau-Migdal parameters in symmetric nuclear matter.

Fig. 4.9 shows the Λ Landau-Migdal parameters in symmetric nuclear matter.
The curves exhibit a very similar density dependence which is stronger (weaker)
for the like (unlike) spins. The main difference lies in the starting point, but this
is an expected result given the differences between the potentials we have seen
in the previous chapters. This is a general feature which can be observed in all
hyperon Landau-Migdal parameters. It is interesting to note that almost all YN
interactions give negative results for the like-spin interactions, implying that this

part of the ΛN interaction is genuinely attractive. For the unlike-spin interactions there is no consensus on attraction or repulsion.
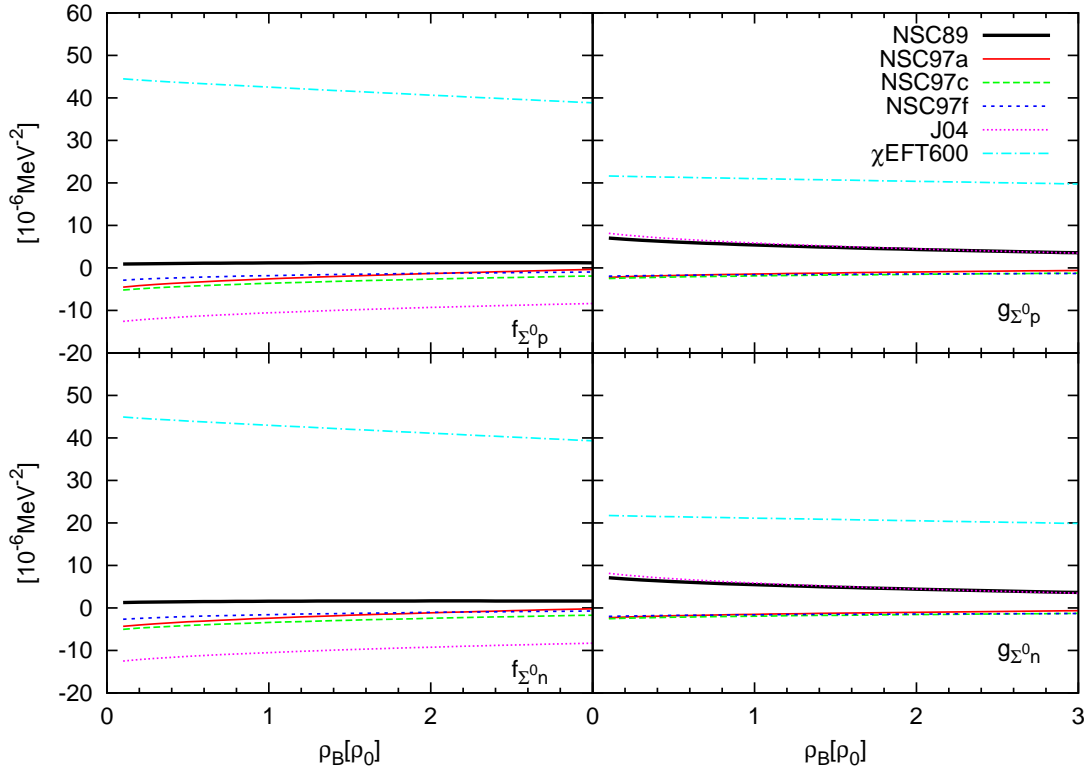

Figure 4.11: Σ^0 Landau-Migdal parameters in symmetric nuclear matter.

In Fig. 4.10, we display the Σ^- Landau-Migdal parameters. The density dependence of the Σ^-, as well as the Landau-Migdal parameters for the other Σ hyperons, is very weak and some of them are practically constant. The reason behind this behavior is that the values of the relative momentum on which the YN $V_{\text{low k}}$ depends are restricted to low values where the momentum dependence of the potential is weak.

In this case all interactions, except $J04$, show remarkably similar results for the f_{Σ^-p}, parameter suggesting a reliable result pointing towards attraction in this channel. Similar agreement exists for the g_{Σ^-n} parameter suggesting repulsion in this case, with the $\chi EFT600$ being the notable exception in this channel. While there isn't such agreement in the other channels, we can at least claim that f_{Σ^-n} and g_{Σ^-p} are attractive.
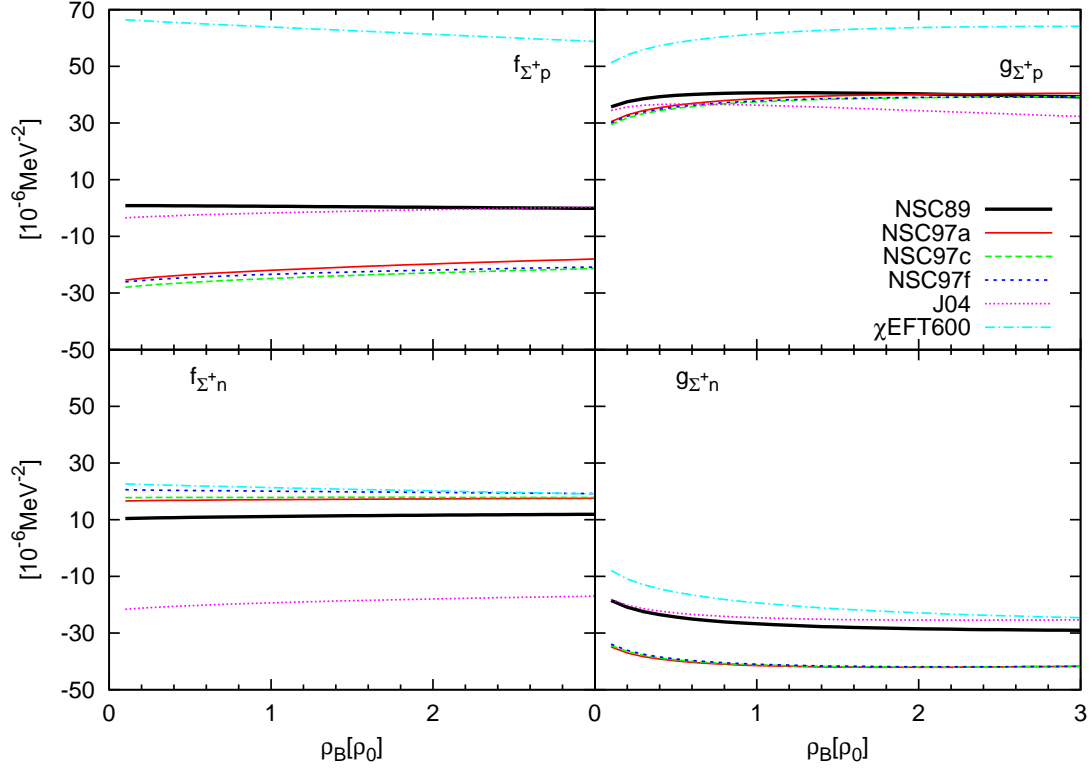
Figure 4.12: Σ^+ Landau-Migdal parameters in symmetric nuclear matter.

The Σ^0 Landau-Migdal parameters, shown in Fig. 4.11, indicate that for the like spins most interactions are attractive. Fig. 4.12 finally shows the Σ^+ Landau-Migdal parameters whose behavior is determined by the relationships mentioned earlier, linking then to the behavior of the Σ^- parameters which we have already discussed.

4.3.2 β-equilibrium

For completeness we show the Landau Fermi liquid parameters for $l = 0$ in β-equilibrium. Fig. 4.13 shows that the differences compared to the case of symmetric matter are not that large for F_0 and G_0 while they can be noticed for F_0' and G_0'. This is expected since the later two quantities are sensitive to differences in the proton to neutron ratio while the former are not. Since this statement is true in general, we do not need to show the other parameters in β-equilibrium.
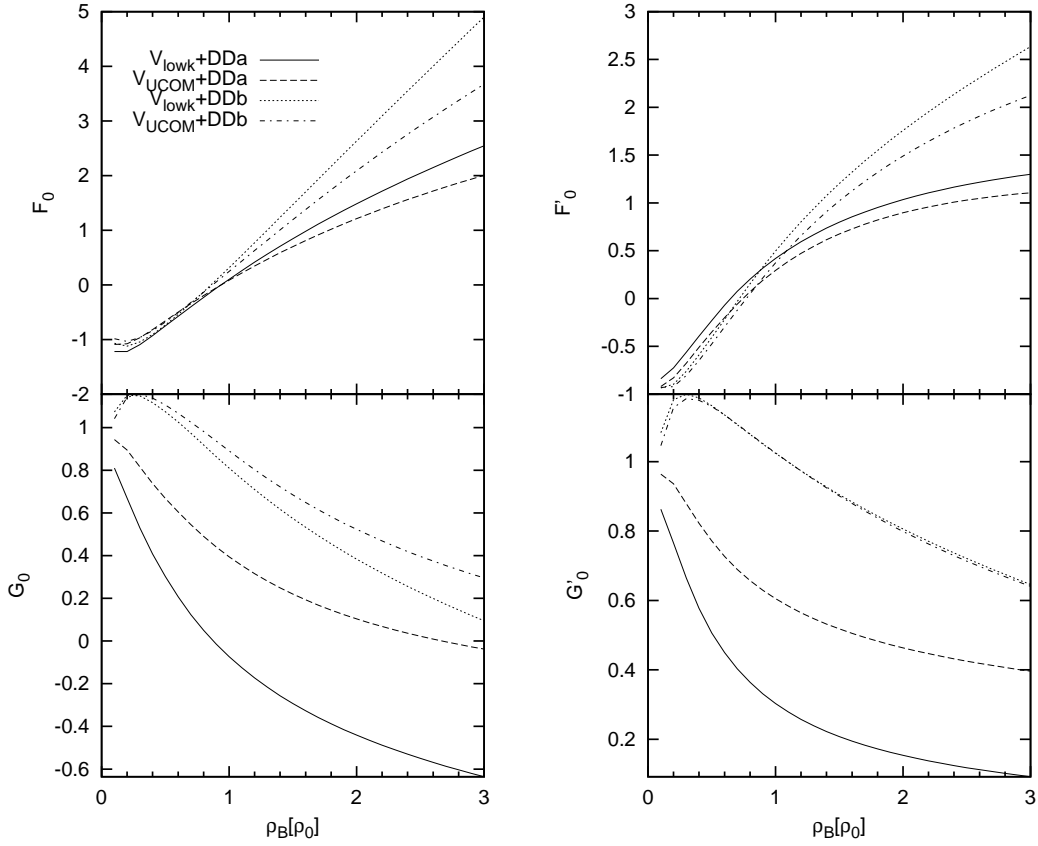
Figure 4.13: Landau Fermi liquid parameters in equilibrated matter for $l = 0$.

One small difference that can be seen for F_0 is that the point at which the matter becomes unstable, $F_0 \leq -1$, has moved to smaller values and is now found at $\sim 0.4\rho_0$.

In Fig. 4.13 we have not shown the pure $V_{\text{low k}}$ and V_{UCOM} since the equilibrium is unrealistic in this case and often impossible to achieve. However, we have instead shown values for the higher K_0 which display some difference compared to the lower K_0 case. The most striking differences are the much larger value of F_0 towards higher densities and the very repulsive nature of the spin part of the force seen through the large G_0 values.

5 Neutrino interactions

The neutrino opacity of dense matter plays an important role in the core collapse supernova theory and in the theory of the development of a newly formed neutron star. In fact, it is believed that neutrinos are intimately involved in the mechanism behind supernovae explosions. Neutrino opacity in neutron stars has two sources: neutral current and charged current interactions of neutrinos with the medium. The calculation of these opacities is a complicated problem. A simple estimate shows that neutrinos in such a dense environment interact with multiple baryons simultaneously [74] as well as that the baryons themselves are interacting with other baryons present in the medium.

Various approximations have been used to address these issues: the effects of relativity; the matter composition; and effects of the baryon-baryon interaction. In such calculations it is not unexpected to find enhancements of the neutrino mean path by factors of $\sim 2-3$. One of the most common approaches is the modification of the baryon response functions due to the in-medium modifications.

There are many physical issues that require the knowledge of the response function of the medium to an external probe. Well-known examples are electron scattering by nuclei or the propagation of neutrinos in nuclear matter. In the mean-field framework, the response function must take into account the effects of long-range correlations by the RPA, which is the small amplitude limit of a time-dependent mean-field approach. The approximation is obtained when the particle-hole interactions are approximated with the Landau-Migdal interaction from the previous chapters. The diagrammatic representation of the approximation is show in Fig. 5.2.

This chapter is organized in the following way; in Sec. 5.1 we will introduce the weak interaction, the charged and neutral current process and calculate the cross section. In Sec. 5.2 we introduce the random phase approximation (RPA) and show the resulting cross sections. Sec. 5.3 is devoted to the results. Those for the neutral current cross section are found in Sec. 5.3.1, the charged current cross section in Sec. 5.3.2 and the mean free path is given in Sec. 5.3.3.
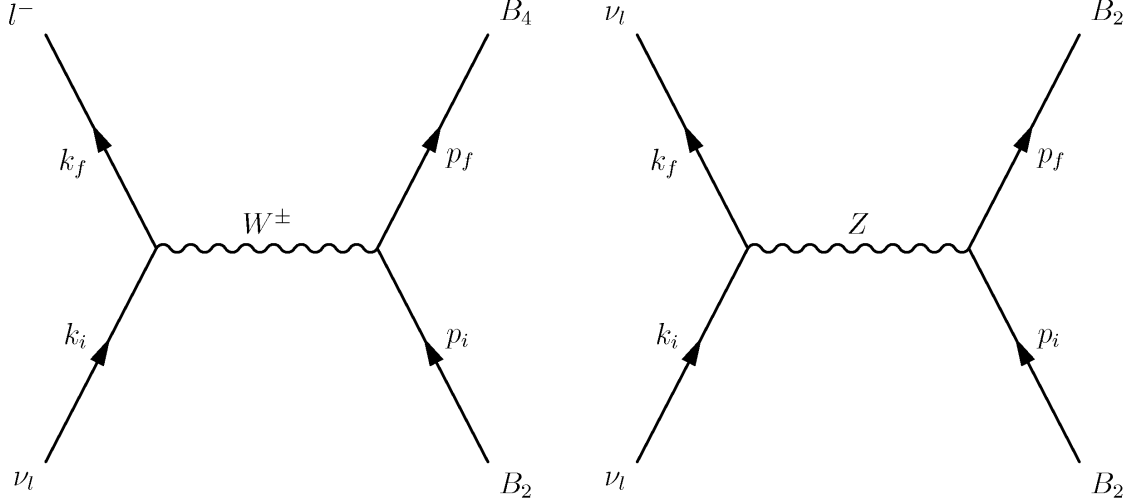
5.1   Weak interaction

Figure 5.1: Weak interactions for β-equilibrium.

The unified model of the electroweak interaction allows for the derivation of accurate cross sections for weak processes between elementary particles [75]. The Lagrangian of such interactions has the form:

$$\mathcal{L}_l = -\frac{g}{2\sqrt{2}} \sum_{l=e,\mu,\tau} \left[\bar{\psi}_{\nu_l}\gamma^\lambda(1-\gamma^5)\psi_l W_\lambda^+ + \bar{\psi} - \frac{g}{2\sqrt{2}} \sum_{l=e,\lambda,\tau} \bar{\psi}_{\nu_l}\gamma^\lambda(1-\gamma^5)\psi_l W_\lambda^- \right]$$

$$- \frac{g}{4\cos\theta_W} \left[\bar{\psi}_{\nu_l}\gamma^\lambda(1-\gamma^5)\psi_{\nu_l} - \bar{\psi}_l\gamma^\lambda(1-\gamma^5)\psi_l \right] Z_\lambda \,, \tag{5.1}$$

$$\mathcal{L}_q = -\frac{g}{2\sqrt{2}}\bar{\psi}_P\gamma^\lambda(1-\gamma^5)U_{CKM}\psi_N W_\lambda^+ - \frac{g}{2\sqrt{2}}\bar{\psi}_N U_{CKM}^\dagger \gamma^\lambda(1-\gamma^5)\psi_P \, W_\lambda^-$$

$$- \frac{g}{4\cos\theta_W} \left[\bar{\psi}_P\gamma^\lambda(1-\frac{8}{3}\sin^2\theta_W-\gamma^5)\psi_P - \bar{\psi}_N\gamma^\lambda(1-\frac{4}{3}\sin^2\theta_W-\gamma^5)\psi_N \right] Z_\lambda^0 \,, \tag{5.2}$$

where $\mathcal{L}_l$ contains the leptonic part and $\mathcal{L}_q$ contains the quark part of the Lagrangian. The positive quarks are collected in $\bar{\psi}_P = (\bar{\psi}_u \ \bar{\psi}_c \ \bar{\psi}_t)$ and the negative are found in $\bar{\psi}_N = (\bar{\psi}_d \ \bar{\psi}_s \ \bar{\psi}_b)$. The standard *Cabibbo-Kobayashi-Maskawa* mixing matrix is represented by U_{CKM} [76]. The parameters in the electroweak Lagrangian are the coupling constant $g = 0.231$, the masses of the $W^\pm$ $m_W = 78$ GeV, and the Z^0, $m_Z = 89$ GeV, bosons and the weak Weinberg angle $\sin^2\theta_W = 0.23$.

However, since the momenta of all particles which we consider are far below the masses of the vector bosons (Z and $W^\pm$) we can take the lowest-order approximation to the weak interaction. Thus the interaction Lagrangian is not the full

electroweak Lagrangian, but instead we will have a Fermi-like weak Lagrangian, (masses of the vector bosons are considered infinite), which can be written in terms of current-current interactions as [77]:

$$\mathcal{L}_{int}^{cc} = \frac{G_F C}{\sqrt{2}} j_\mu J_W^\mu \,, \tag{5.3}$$

$$\mathcal{L}_{int}^{nc} = \frac{G_F}{\sqrt{2}} j_\mu^\nu J_Z^\mu \,, \tag{5.4}$$

where $G_F = 1.166 \times 10^{-11} \mathrm{MeV}^{-2}$ is Fermi weak coupling constant, and C is the Cabibbo factor: $C = \cos\theta_c$ for strangeness changing reactions and $\Delta S = 0$ and $C = \sin\theta_c$ for $\Delta S = 1$. The first Lagrangian Eq. (5.3) describes the charged current process mediated by the W-boson, the left-hand side of Fig. 5.1,

$$\nu_l + B_2 \rightarrow l + B_4 \,, \tag{5.5}$$

while the second Eq. (5.4) describes neutral current processes mediated by the Z-boson, the right-hand side of Fig. 5.1,

$$\nu_l + B_2 \rightarrow \nu_l + B_4 \,. \tag{5.6}$$

The corresponding charged currents are:

$$j_\mu = \bar{\psi}_l \gamma_\mu (1 - \gamma_5) \psi_\nu \,, \tag{5.7}$$

$$J_W^\mu = \bar{\psi}_4 \gamma^\mu (g_V - g_A \gamma_5) \psi_2 \,, \tag{5.8}$$

for Eq. (5.3), while for Eq. (5.4) the neutral currents are:

$$j_\mu^\nu = \bar{\psi}_\nu \gamma_\mu (1 - \gamma_5) \psi_\nu \,, \tag{5.9}$$

$$J_Z^\mu = \bar{\psi}_2 \gamma^\mu (c_V - c_A \gamma_5) \psi_2 \,. \tag{5.10}$$

The fields ψ_l, ψ_ν, ψ_2 and ψ_4 are quantized fields of leptons, neutrinos, incoming baryons and outgoing baryons. Since they all are fermions they can be described in terms of quantized Dirac fields. We expand them in terms of a complete set of plane-wave states

$$\psi(x) = \sum_{sp} \left(\frac{m}{\Omega E_p} \right)^{\frac{1}{2}} c_s(p) u_s(p) e^{-ipx} \,, \tag{5.11}$$

where $c_s(p)$ is a creation operator and $u_s(p)$ denotes the spinor of a particle with spin s and four-momentum p. The normalization in this case is for a box of volume Ω, but as usual we will take the limit $\Omega \rightarrow \infty$. The vector and axial-vector coupling constants g_V and g_A for charged currents and c_V and c_A for neutral currents are listed in Tab. 5.2 and Tab. 5.1 for the particles of interest, see Ref.[77].

	g_V	g_A
$\nu_l + n \to l^- + p$	1	$D + F = 1.23$
$\nu_l + \Sigma^- \to l^- + \Lambda$	0	$\sqrt{2/3}D = 0.62$
$\nu_l + \Sigma^- \to l^- + \Sigma^0$	$\sqrt{2}$	$\sqrt{2}F = 0.67$
$\nu_l + \Sigma^0 \to l^- + \Sigma^+$	$-\sqrt{2}$	$-\sqrt{2}F = -0.67$
$\nu_l + \Lambda \to l^- + \Sigma^+$	0	$-\sqrt{2/3}D = -0.62$
$\nu_l + \Lambda \to l^- + p$	$\sqrt{3/2}$	$-\sqrt{3/2}(F + D/3) = 0.89$
$\nu_l + \Sigma^0 \to l^- + p$	1	$\sqrt{1/2}D = 0.54$
$\nu_l + \Sigma^- \to l^- + p$	-1	$D - F = 0.28$
$\nu_e + \mu^- \to \nu_\mu^- + e^-$	1	1

Table 5.1: Charged current vector and axial vector couplings [77]. Numerical values are quoted using $D = 0.756$, $F = 0.477$, $\sin^2 \theta_W = 0.23$ and $\sin^2 \theta_c = 0.053$ (see Ref.[78]). As usual $\nu_l(l)$ stands for all neutrinos (leptons). For corrections arising due to explicit $SU(3)$ breaking terms, see Ref.[79].

	c_V	c_A
$\nu_e + e^- \to \nu_e + e^-$	$0.5 + 2\sin^2 \theta_W = 0.96$	0.5
$\nu_\mu + \mu^- \to \nu_\mu + \mu^-$	$0.5 + 2\sin^2 \theta_W = 0.96$	0.5
$\nu_e + \mu \to \nu_e + \mu$	$-0.5 + 2\sin^2 \theta_W = -0.04$	-0.5
$\nu_{\mu,\tau} + e^- \to \nu_{\mu,\tau} + e^-$	$-0.5 + 2\sin^2 \theta_W = -0.04$	-0.5
$\nu_l + n \to \nu_l + n$	-0.5	$-D - F = -0.62$
$\nu_l + p \to \nu_l + p$	$0.5 - 2\sin^2 \theta_W = 0.04$	$D + F = 0.62$
$\nu_l + \Lambda \to \nu_\Lambda$	-0.5	$-F - D/3 = -0.36$
$\nu_l + \Sigma^- \to \nu_l + \Sigma^-$	$-1.5 + 2\sin^2 \theta_W = -1.04$	$D - 3F = -0.34$
$\nu_l + \Sigma^+ \to \nu_l + \Sigma^+$	$0.5 - 2\sin^2 \theta_W = 0.04$	$D + F = 0.62$
$\nu_l + \Sigma^0 \to \nu_l + \Sigma^0$	-0.5	$D - F = 0.14$
$\nu_l + \Sigma^0 \to \nu_l + \Lambda$	0	$2D/\sqrt{3} = 0.44$

Table 5.2: Neutral current vector and axial vector couplings [77]. Numerical values are quoted using $D = 0.756$, $F = 0.477$, $\sin^2 \theta_W = 0.23$ and $\sin^2 \theta_c = 0.053$ (see Ref.[78]). As usual $\nu_l(l)$ stands for all neutrinos (leptons). For corrections arising due to explicit $SU(3)$ breaking terms, see Ref.[79].

Once the currents and the states have been defined one is able to proceed with the calculation of the processes shown in Fig. 5.1. In a vacuum such calculations are most commonly performed by calculating the expectation value of the transition operator Eq. (C.1). However, in the medium it is more convenient to use the

optical theorem and calculate the cross section. In this work we have used this approach and calculated the cross sections. In Appendix C some details of the calculation are shown, the end result for the differential cross section is found as Eq. (C.29).

For the derivation in Appendix C we have used several approximations that are justified if one considers the typical energy scales involved. The first one relates to the properties of baryons in a dense medium. The temperature range we are interested in is of the order 10 MeV thus we can safely assume that the baryons we are considering (nucleons and hyperons) due to their mass ~ 1 GeV, which is far greater than the temperature range ($T \ll M_b$), are non-relativistic. Hence in Eq. (C.38) we use the nonrelativistic propagators of Eq. (C.36) instead of the relativistic ones Eq. (C.18). The approximation can also be expressed as disregarding the baryon momentum compared to its energy $\frac{|p_b|}{E_b} \ll 1$. The second approximation concerns the leptons (electrons and neutrinos) whose chemical potential, in neutron stars, is far greater than the mass of the electron or neutrino ($m_l \ll \mu_l$). Hence we consider the leptons as being fully relativistic, which gives $\frac{\vec{p}_l}{E_l} = \hat{\vec{p}}_l$ and Eq. (C.27).

With these approximations it is natural to use the laboratory reference frame in which, for the relative velocity, we have

$$ v_{rel} = \frac{|\vec{k}_i|}{\epsilon_i} \, . \tag{5.12} $$

Thus we have all of the information needed to perform the calculation of the differential cross section in-medium and the result calculated in Appendix C is:

$$ \frac{1}{\Omega} \frac{d^3\sigma(E_\nu)}{d\Omega^2 dq_0} = \frac{G_F^2}{8\pi^3} E_3^2 \left(1 - f(E_3)\right) \left[(1 + \cos\theta)S_V(q_0, q) + (3 - \cos\theta)S_A(q_0, q)\right] \, . \tag{5.13} $$

This equation works both for the charged current and the neutral current cross section. In the first case the Fermi function f and energy E_3 will be those of the leptons while in the second case it will be the neutrinos. Obviously in both cases we have to take care to use the appropriate structure functions.

Since in section Sec. 5.3 we will be interested in the dependence of the differential cross section on the transferred energy it is useful to see which range of values is allowed by the kinematics for the transferred energy given these approximations. The limiting factor will be the value of the angle θ (equivalently $\cos\theta$). From the definition of transferred momentum $\vec{q} = \vec{p}_\nu - \vec{p}_l$ one gets

$$ \frac{\vec{p}_\nu \cdot \vec{p}_l}{E_\nu E_l} = \cos\theta = \frac{E_\nu^2 + E_l^2 - q^2}{2 - E_l E_\nu} \, . \tag{5.14} $$

The limits are $|\cos\theta| \leq 1$. From this with the aid of the relation for the transferred energy $q_0 = E_\nu - E_l$ we get two conditions $|q_0| \leq q$ and $q_0 \leq 2E_\nu - q$. Since in most cases for the differential cross section we fix $|\vec{q}| = E_\nu$, these two conditions will be one and the same.

From the differential cross section we can calculate the total cross section and the mean free path. The total cross section per unit volume is easily calculated by integrating over all of the remaining variables by

$$\frac{\sigma(E_\nu)}{\Omega} = \int \frac{1}{\Omega}\frac{d^3\sigma(E_\nu)}{d^2\Omega\,dq_0}d\Omega dq_0\,. \tag{5.15}$$

The mean free path is just the inverse of the total cross section

$$\lambda(E_\nu) = \left(\frac{\sigma(E_\nu)}{\Omega}\right)^{-1}\,. \tag{5.16}$$

5.2   Random phase approximation
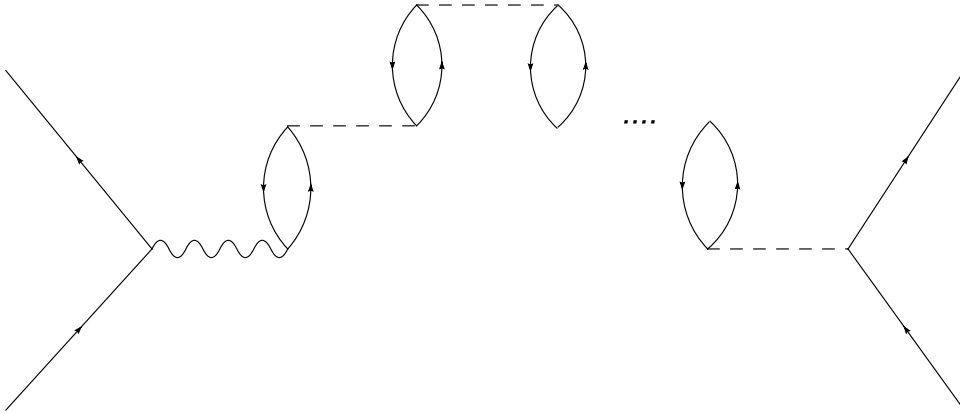
Figure 5.2: Higher-order loop corrections to the weak interaction in dense matter.

In Appendix C we have introduced the structure (S) and polarization $(\tilde{\Pi})$ functions in Eq. (C.28) and Eq. (C.25), respectively. The Hartree-Fock approximation of the polarization function contains only one loop. However in the case of dense matter we must also consider interactions with a higher number of loops. Essentially, a neutrino propagating in dense matter will create an excitation which can propagate via the interaction with matter thus modifying the response of the matter. This can be represented schematically as in Fig. 5.2.

The inclusion of a higher number of loops corresponds to the ring approximation or random phase approximation[1] [33]. The key point that must be stressed out about these graphs is that there are exactly two particles participating in each loop, that is if we were to cut the graph vertically we would only cross two propagator lines. These propagator pairs in the loop are those of particles and holes and not particles and antiparticles. One can also note that this is in fact a quasiparticle RPA since we are using the quasiparticle approximation which replaces the bare mass and chemical potentials of particles with the effective ones. Putting it in another way, the propagators entering the zeroth-order polarization function $\tilde{\Pi}^0(\vec{q}, q_0)$ defined by Eq. (C.38), are not of free particles and holes, but are themselves dressed.

In practical terms the RPA relies on summing all of the ring diagrams in Fig. 5.2. The summing of these ring diagrams yields then the Bethe-Salpeter equation[2] for the particle-hole polarization function [33],

$$\tilde{\Pi}_{\eta\lambda\varphi\chi}(\vec{q}, q_0) = \Pi^0_{\eta\lambda\varphi\chi}(\vec{q}, q_0) + \sum_{\alpha\beta\gamma\delta} \Pi^0_{\eta\lambda\alpha\delta}(\vec{q}, q_0) K_{\alpha\delta;\beta\gamma}(\vec{q}, q_0) \tilde{\Pi}_{\beta\gamma\varphi\chi}(\vec{q}, q_0), \quad (5.17)$$

where $\tilde{\Pi}(\vec{q}, q_0)$ is the full polarization function and $K_{\alpha\delta;\beta\gamma}(\vec{q}, q_0)$ is a kernel defined by the interaction. The indices α, β, γ and δ run over both spin and isospin space and in our case also involve hyperons. For the RPA the kernel takes the form

$$K^{(1)}_{\alpha\beta;\gamma\delta} \equiv \langle \gamma\,\beta \mid V \mid \alpha\,\delta \rangle - \langle \beta\,\gamma \mid V \mid \alpha\,\delta \rangle, \quad (5.18)$$

where V is a potential, which defines the interaction. It has been shown [33] that such a definition of the kernel indeed corresponds to the RPA, since it produces the same equations of motion.

We will not go further here into the details about various kernels and the solution of Eq. (5.17) but refer the reader to Appendix C. Additionally more details on the RPA itself, especially for finite systems, can be found in [33]. However we note that for a truly self-consistent calculation one should interpret the RPA as the small limit of time-dependent Hartree-Fock-Bogoliubov theory.

5.2.1 Cross sections within the random phase approximation

With the knowledge of the RPA polarization function we can see how the cross section changes with the inclusion of it. The RPA is simply accounted for as the

---

[1]This name has historic reasons and it is not very illuminating here. For our case the term ring approximation carries much more meaning.

[2]In our approach, since we will be dealing with nonrelativistic particles this should be called the Salpeter equation, but at this level Eq. (5.17) is general and could also be used for relativistic particles.

replacement of the structure functions S with the RPA structure functions S^{RPA} obtained in Appendix C. The distinction between the vector and axial structure function is more obvious in this case as we cannot just factorize out the coupling constant and get the same function. Thus for the cross section in the RPA we have, as in [5]

$$\frac{1}{\Omega}\frac{d^3\sigma(E_1)}{d\Omega^2 dq_0} = \frac{G_F^2}{8\pi^3}E_3^2[1 - f(E_3)]\left[(1 + \cos\theta)S_V^{RPA}(q_0, q)\right.$$
$$\left. + (3 - \cos\theta)S_A^{RPA}(q_0, q)\right] . \tag{5.19}$$

Again, like Eq. (5.13), the formula is general enough to be used in both the charged current and the neutral current case. All we have to be careful about is which structure function we use and which particle is the outgoing one.

5.3   Results

Let us now turn to the quantitative results of neutrino reaction rates. For the differential cross section and the mean free path the contributions from each particle type need to be accounted for. For the calculation of the differential cross section Eq. (5.13), the chemical potentials, Fermi momenta and the temperature need to be specified. For symmetric matter these quantities are set by hand while, in the case of β-equilibrated matter, they are provided by the calculation explained in chapter 3. The particle-hole parameters are calculated as in chapter 4. The effects of temperature, like the effects of the strong interaction, mainly affect the results presented here through the polarization (structure) functions.

In the case where only nucleons are present, we will focus on showing results at $0.5\rho_0$ and ρ_0. For the cases with hyperons we will show results at $2\rho_0$ and $3\rho_0$ since at these densities the concentrations of hyperons are sizable. For the temperature we will focus on $T = 0$ MeV, which should best describe older and colder neutron stars while $T = 10$ MeV represents neutron stars soon after creation.

For all cross sections presented below we have fixed the neutrino energy at $E_\nu = 25$ MeV and fixed the momentum transfer to $q = E_\nu$ for the neutral current cross sections and to $q = E_\nu + \mu_e$ for the charged current cross sections. For the mean free path we take the neutrino energy to be $E_\nu = \pi T$ since this is the mean energy of untrapped neutrinos [80].

5.3.1   The neutral current cross section

An indication of interaction corrections is first shown in Fig. 5.3. This figure shows arguably the simplest case of all those investigated here, the neutrino neutral current cross section in symmetric nuclear matter with just two-body NN

interactions. Two densities and two temperatures are shown. The results of the Hartree-Fock and RPA calculations for both the $V_{\text{low k}}$ and V_{UCOM} are compared.
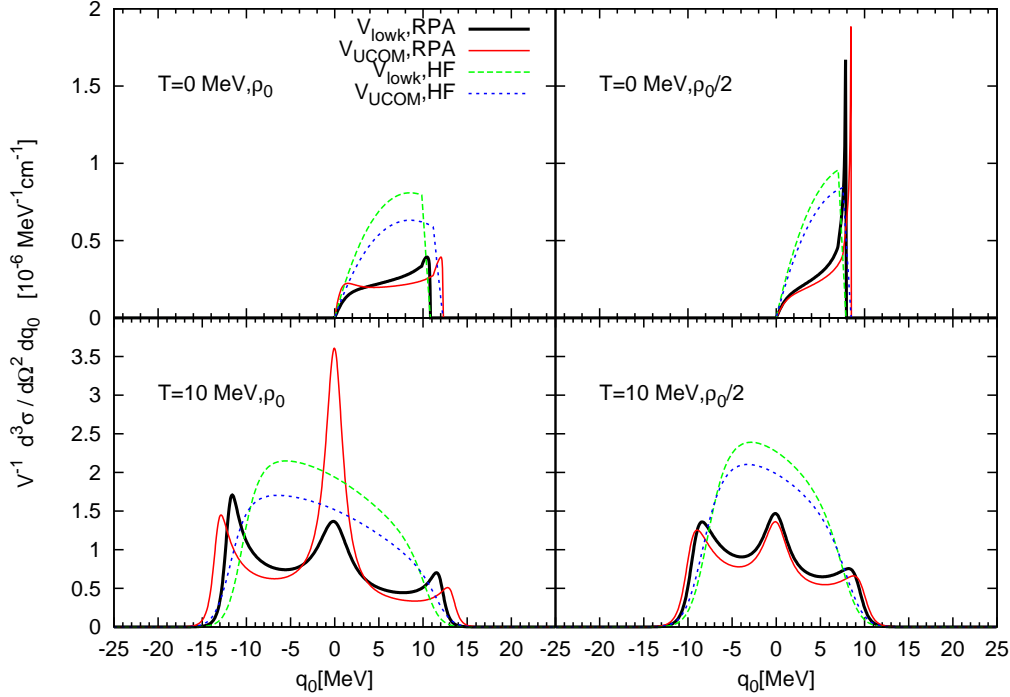

Figure 5.3: Neutrino neutral current cross section in symmetric nuclear matter with just two-body NN interactions.

At zero temperature (upper panels) we can clearly see the effects of the different effective masses of a nucleon in the $V_{\text{low k}}$ and V_{UCOM} as the difference in endpoints of the cross sections. If we now compare this result with Fig. 5.4 we see the same values for the endpoints with and without the density-dependent force. This is obvious because, in the quadratic approximation for the energy, the endpoint is determined by the ratio $\frac{k_F}{M^*}$ which is different for the $V_{\text{low k}}$ and V_{UCOM} potentials but the same with and without the density-dependent force, cf. Fig. 4.4.

The bottom panels illustrate the effect of temperature on the differential cross section. At zero temperature only positive energies are present, because of Pauli blocking, but at non-zero temperature there is a sufficient number of excited states to allow such transitions. This is an effect present at any temperature. For low baryon densities even low temperatures render the system non-degenerate. For the temperature of $T = 10$ MeV, and in general for all finite temperatures, the

cross section is dominated by a region for which $q_0 < T$.

The biggest difference between the Hartree-Fock and RPA calculation is the enhancement apparent at the end of the allowed energy interval. This enhancement is easiest understood if we consider the neutral current vector polarization function. In symmetric nuclear matter, where only nucleons contribute and proton and neutron zeroth-order polarization functions are the same and Eq. (C.73) simplifies to

$$\tilde{\Pi}_V^{NC} = \tilde{\Pi}^0 \left[\left((c_{pp}^V)^2 + (c_{nn}^V)^2\right) \left(1 - f_{pp}\tilde{\Pi}^0\right) + 2c_{pp}^V c_{nn}^V f_{pn}\tilde{\Pi}^0 \right] / D_{NC}^V , \qquad (5.20)$$

where the denominator D_{NC}^V simplifies to

$$\begin{aligned} D_{NC}^V &= \left[1 - (f_{pp} + f_{pn}) \tilde{\Pi}^0 \right] \left[1 - (f_{pp} - f_{pn}) \tilde{\Pi}^0 \right] \\ &= \left[1 - 2F_0 \frac{\tilde{\Pi}^0}{N_0} \right] \left[1 - 2F_0' \frac{\tilde{\Pi}^0}{N_0} \right] , \end{aligned} \qquad (5.21)$$

where the F_0 and F_0' are the Landau parameters and N_0 is the density of states, see chapter 4. In the case of the Hartree-Fock calculation the determinant D_{NC}^V is equal to one. When it approaches zero in the case of the RPA it causes precisely the enhancement seen in Fig. 5.4 and all similar enhancements in subsequent figures. This behavior is usually referred to as the zero-sound because it represents a resonance corresponding to a collective motion of the system.

If we neglect the zero-sound enhancement, the effect of the medium correction seen in the RPA curves is that of damping. From looking at Eq. (C.59) we can see that whenever the kernel $K_{\alpha\beta;\delta\gamma}$ is a positive-definite matrix (an overall repulsive interaction) we will have a suppression and when we have negative-definite matrix (attractive interaction) we will have an enhancement. If the nature of the spin-like and spin-unlike interaction is different, i.e. one is repulsive and the other attractive, than we have a composite effect whose nature will depend on which channel (vector or axial) dominates. It is in fact often the case that spin-like and spin-unlike interactions are different, cf. Fig. 4.13. In the case of Fig. 5.3, and for all other neutral current cross sections with only nucleons, the repulsive interaction in the vector channel mostly dominates the response. The only exception is the enhancement at zero energy transfer at finite temperature which is caused by the axial channel.

In Fig. 5.4 the neutrino neutral current cross section in symmetric nuclear matter with density-dependent interactions is shown. It is evident that the inclusion of density-dependent interactions enhances the collective behavior of the system. Hence the peaks we see at zero temperature are much more pronounced. It also significantly alters the finite temperature response, although the Hartree-Fock calculation, which is only influenced by the effective mass, stays largely unchanged.
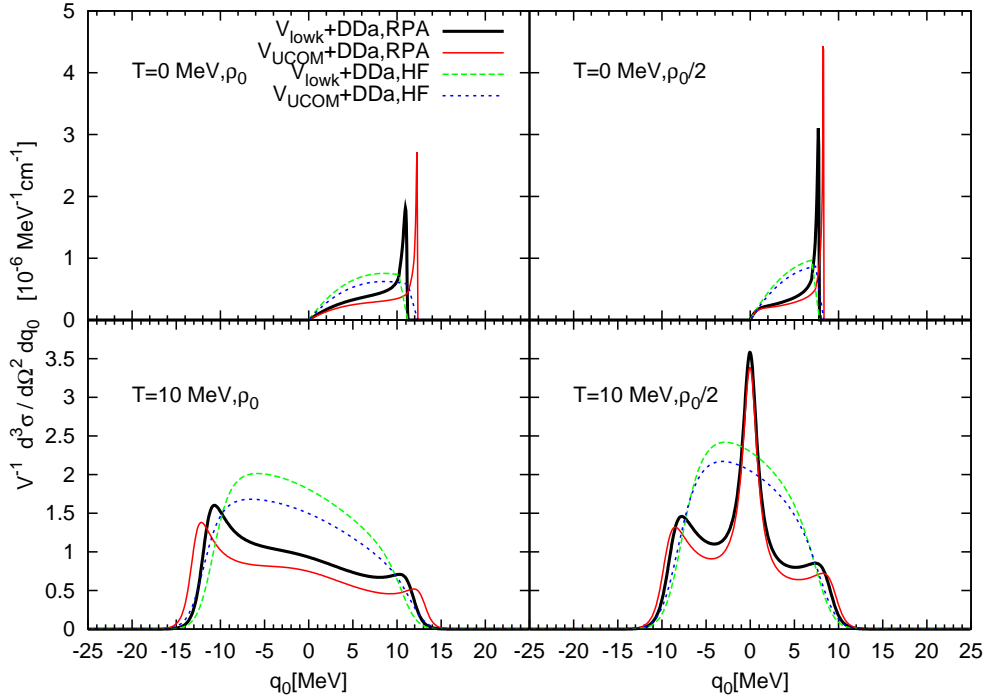
Figure 5.4: Neutrino neutral current cross section in symmetric nuclear matter with density-dependent interactions.

Large effects for the RPA calculation are the result of significantly altered interactions in both like spin (F_0) and the unlike spin (G_0) channels which we saw in Fig. 4.5.
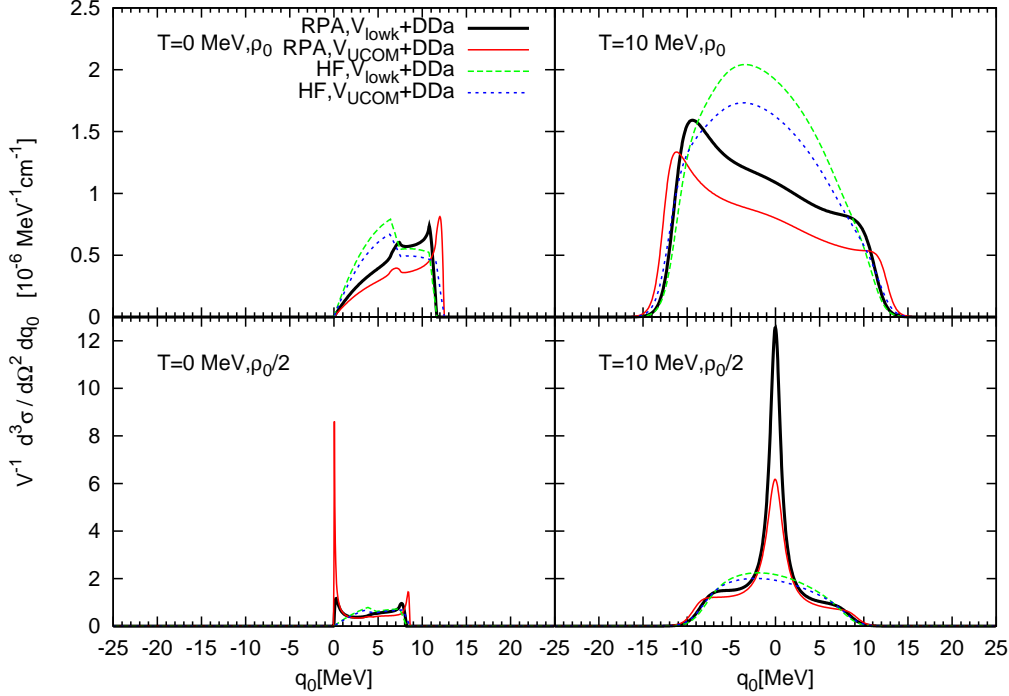
The neutrino neutral current cross section in β-equilibrated dense matter with density-dependent interactions is shown in Fig. 5.5. The appearance of two distinct Fermi surfaces is now clearly visible. Hence we now have two Fermi momenta and two effective masses to consider. In the case of the lower panels ($\rho_0/2$) we see an extremely strong peak close to zero. This peak is caused by the determinant of the vector response which appears when solving Eq. (5.18). Obviously at this density the interaction is attractive enough to cause such an effect. This is somewhat unusual since most other peaks at zero energy transfer are produced by the determinant of the axial response, as we will see in the following figures.

In the case of dense matter with hyperons we have a complex multicomponent system whose response is different from a response of the relatively simple nucleonic system we showed so far. At any given density the concentrations and

Figure 5.5: Neutrino neutral current cross section in β-equilibrated dense matter with density-dependent interactions.

the effective masses as well as the strength of the coupling to the medium will play a significant role. In addition to the Fermi spheres of nucleons we also have to consider those of hyperons and for the RPA we now have a more complex matrix which enters the kernel. All of these effects will be entangled when we solve the matrix equation Eq. (C.59) which will make the study of individual effects difficult. However some of the leading effects can be recognized due to their magnitude.

Fig. 5.6, Fig. 5.7 and Fig. 5.8 show the neutrino neutral current cross section in β-equilibrated dense matter with density-dependent interactions and the YN interaction for NSC97f, χEFT 600 and J04 models, respectively. The upper panels show results at $2\rho_0$ and the lower panels show those at $3\rho_0$. On the left-hand sides of these three figures we plot the $V_{\text{low k}} + DDa$ and on the right-hand sides $V_{UCOM} + DDa$.

At zero temperature we see the first drop after the initial rise which comes from the hyperons, the second decrease comes from protons and is much less
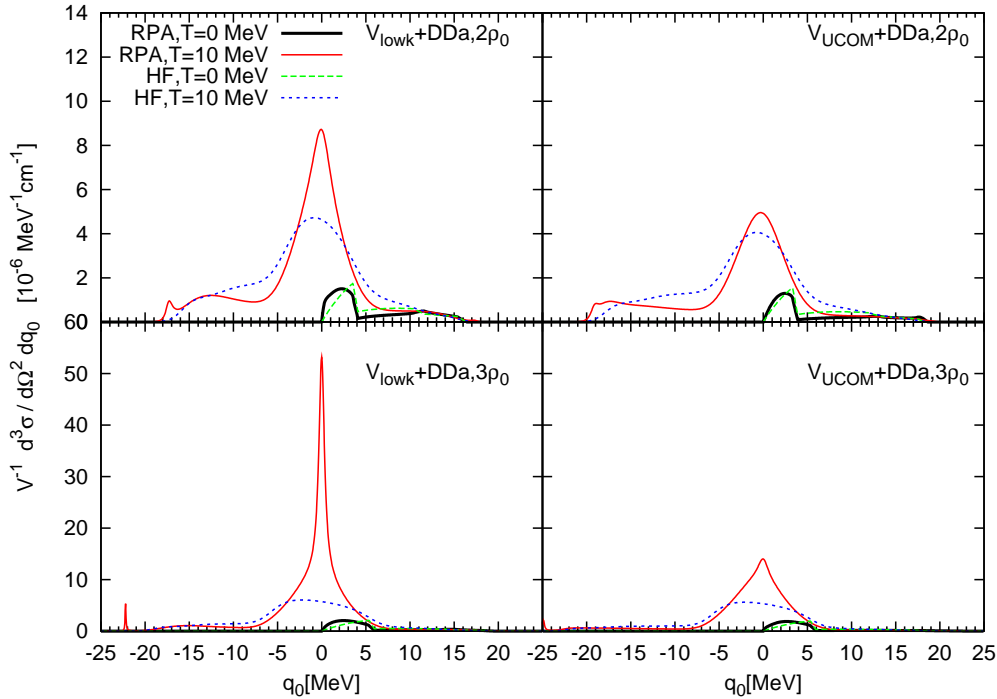
Figure 5.6: Neutrino neutral current cross section in β-equilibrated dense matter with density-dependent interactions and YN interaction from the NSC97f model.

pronounced and the last drop is from neutrons. This clearly binds the effect of hyperons to low energy transfers which is also true for finite temperatures. The best example for effects at higher energy transfer coming from nucleons is the appearance of the peak on the left end of the $T = 10$ MeV curves. This peak comes only from neutrons but it is strongly enhanced by the determinant of the vector response. The only reason why we do not have a stronger peak at this point is that at these energies the Pauli blocking effect is rather strong. Such a peak is commonly referred to as the zero-sound peak. We can also notice that as the density increases the peak moves out towards higher energy transfers, and on some occasions is completely outside of the main part of the cross section.

The biggest difference between the three figures, Fig. 5.6, Fig. 5.7 and Fig. 5.8 lies in their behavior at zero energy transfer. At this point the NSC97f model shows a peak coming from the approach to zero of the axial response determinant whose magnitude as this point is ~ 0.1 at $2\rho_0$ leading to an order of magnitude increase in the cross section. For χEFT 600 at the same density it has the value of
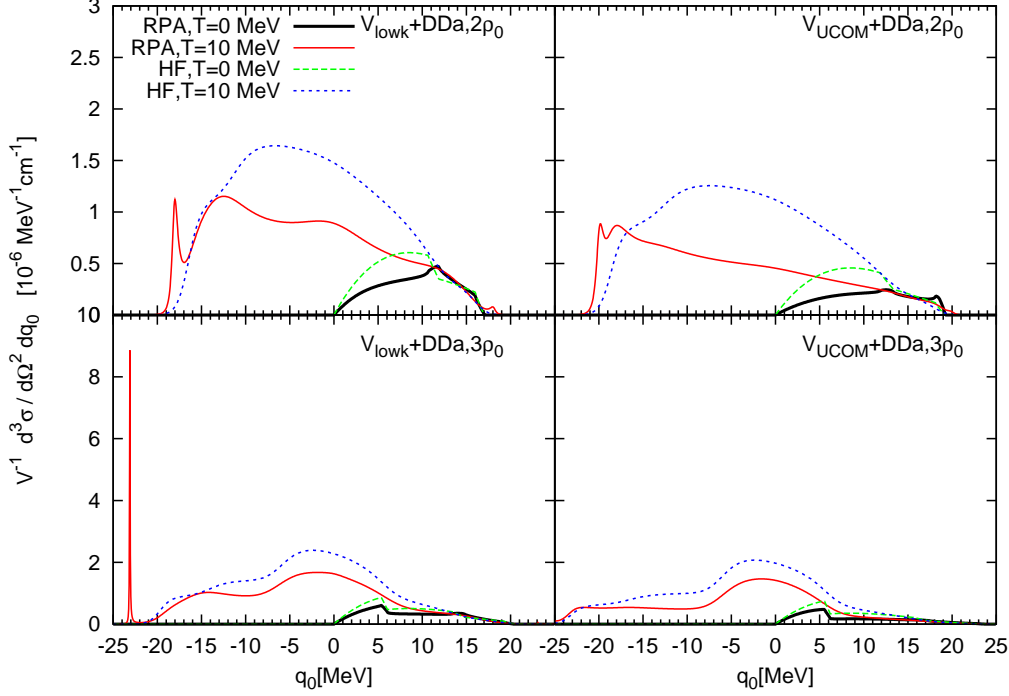
Figure 5.7: Neutrino neutral current cross section in β-equilibrated dense matter with density-dependent interactions and the YN interaction from the χEFT 600 model.

~ 0.5 making the peak non-existent. The same value for the J04 lies between these two at ~ 0.25 which results in a visible, but significantly less pronounced peak for this model. While these observations were made for the case of $V_{\text{low k}} + DDa$ an identical hierarchy is observed for $V_{UCOM} + DDa$ but in this case all peaks are less pronounced. They are less pronounced because the axial response determinant is systematically larger in these cases.

The last figure in this section, Fig. 5.9, is devoted to displaying the comparison of all neutrino neutral current cross sections in β-equilibrated dense matter with density-dependent interactions at a density of $3\rho_0$ and a temperature of $T = 10$ MeV. This comparison shows in a systematic way some of observations made in specific cases before. The upper panels show the comparison of the Hartree-Fock calculation while the lower shows the same for the RPA. The limitation of hyperon effects to small energy transfers is evident if we take a look at the Hartree-Fock calculation. Small differences at higher energy transfers come from changes in the
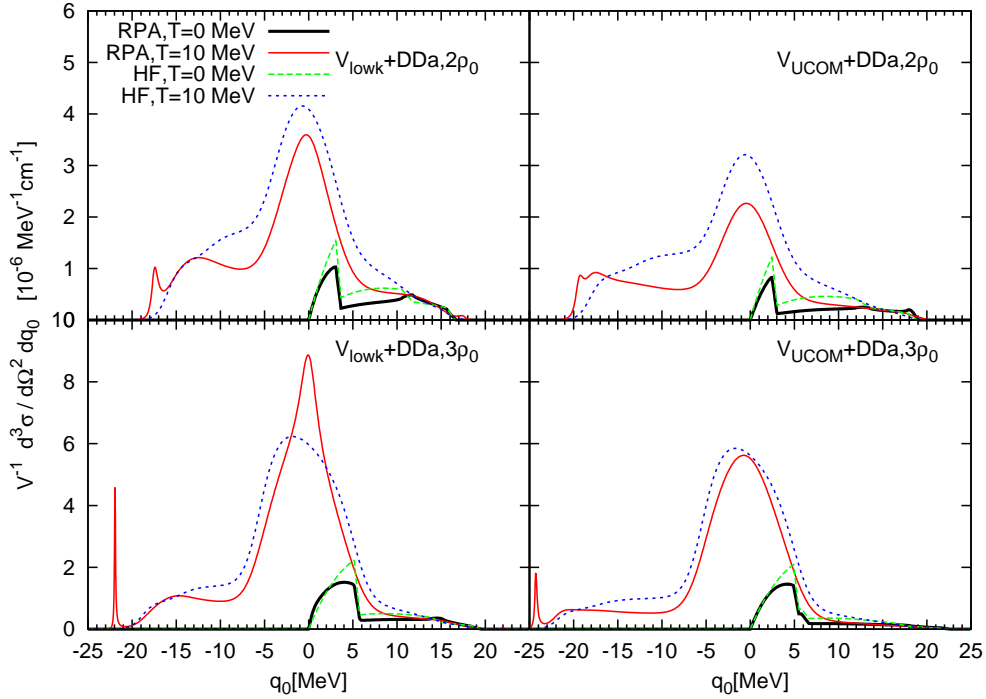
Figure 5.8: Neutrino neutral current cross section in β-equilibrated dense matter with density-dependent interactions and the YN interaction from the $J04$ model.

neutron Fermi momentum introduced by β-equilibrium. The zero-sound effects as well as the differences in the peaks at zero energy transfer are apparent in the lower left panel displaying the $V_{\text{low k}} + DDa$. The absence of such an effect for $V_{UCOM} + DDa$ shows the sensitivity to the parameters in the kernel of Eq. (5.18).

5.3.2 The charged current cross section

Fig. 5.10 shows the charged current cross section in symmetric nuclear matter with inclusion of density-dependent interactions. As could have been expected these graphs are very similar to those for the neutral current because the polarization functions of the nn and the pn system in symmetric matter are practically identical. They are alike because the kinematical differences which arise in β-equilibrium due to the presence of the electron chemical potential are not there in symmetric matter. The small difference seen in the upper panels, is that the cross section curves do not start at zero but at a small negative value. The reason
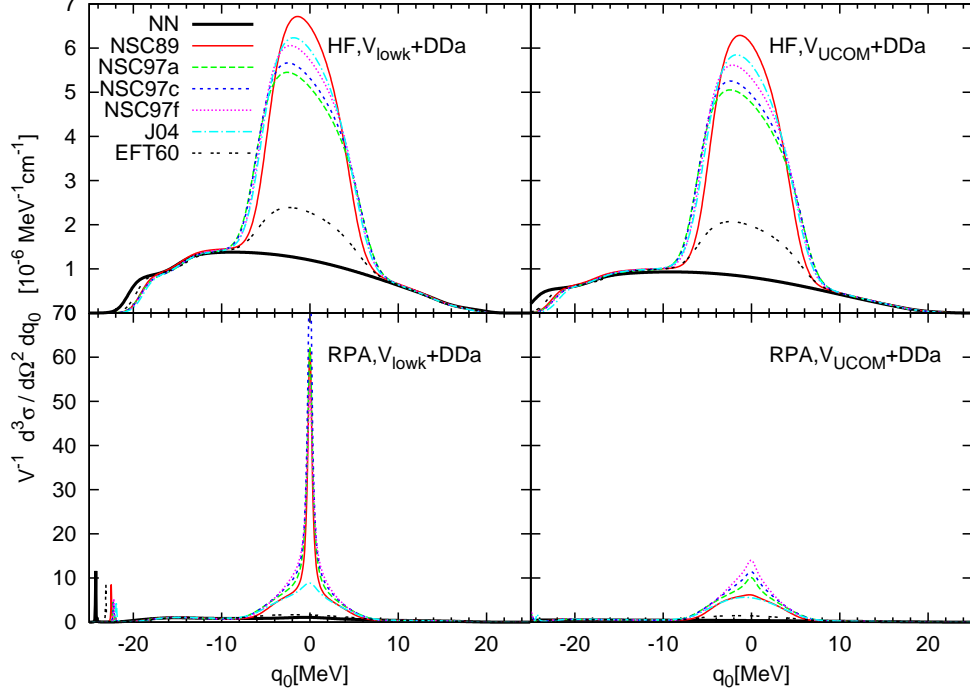
Figure 5.9: Neutrino neutral current cross section in β-equilibrated dense matter with density-dependent interactions and various the YN interaction at a density of $3\rho_0$ and a temperature of $T = 10$ MeV.

behind this is the small difference in mass of the proton and neutron. The same peak structure at the end of the energy range as well as the suppression for lower energy transfers, for the RPA calculations, is seen here just like in the case of the neutral current and the reasons for them are the same.

In the Fig. 5.11 we display the neutrino charged current cross section in β-equilibrated dense matter with density-dependent interactions. These results are significantly different compared to the neutral current case because of the presence of the electron chemical potential in the cross section. We see that the entire cross section has been shifted towards negative values of the energy transfer. The amount of the shift is closely linked to the value of the electron chemical potential. As for the phase space available for these cross sections it is easy to see that on the left-hand side they are dominated by Pauli blocking while on the right-hand side they are determined by the kinematical limits.

For the case of the charged current cross section with hyperons we only show,
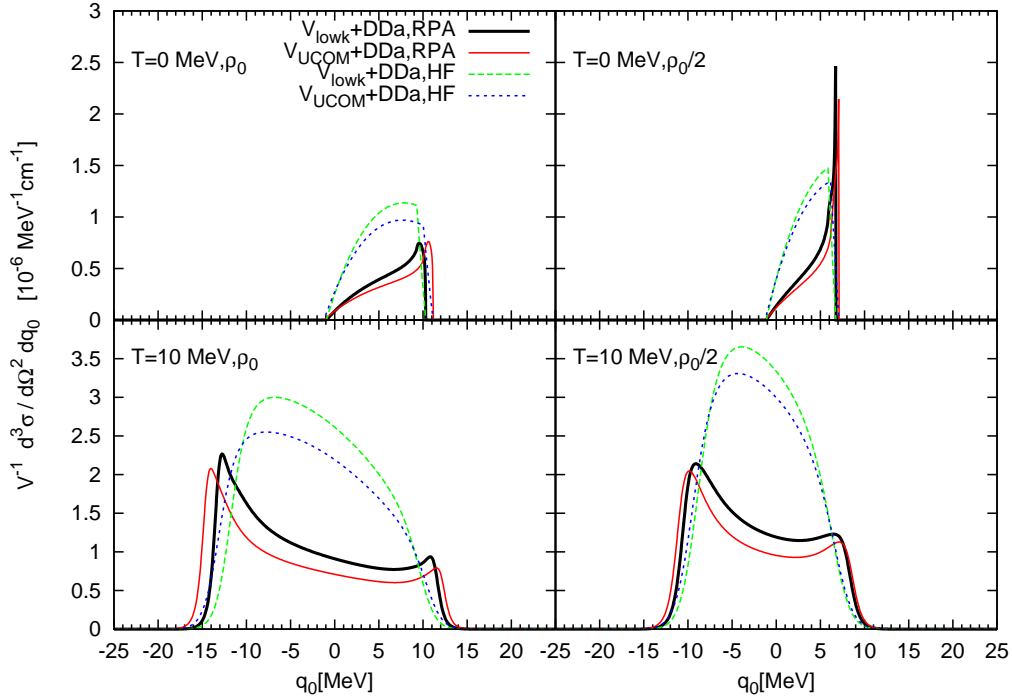
Figure 5.10: Neutrino charged current cross section in symmetric nuclear matter with density-dependent interactions.

Fig. 5.12, because all effects seen in this model can be also seen in all others. The general feature of suppression in the RPA calculations compared to the Hartree-Fock ones is here just like for Fig. 5.11, which showed the cross section without hyperons. The limitations on the phase space are the result of the same effect. The only small difference is that the value of the electron chemical potential is different due to differences in the β-equilibrium. Even the magnitudes of the cross section stay the same because by far the most dominate part is the *pn* polarization loop. A small effect of the hyperon polarization functions can be seen in the lower right figure as a small indentation in the middle of the RPA curve for $T = 10$ MeV.

5.3.3 Mean free path

Both neutral current (left) and charged current (right) neutrino mean free paths, in symmetric nuclear matter with density-dependent interactions for several tem-
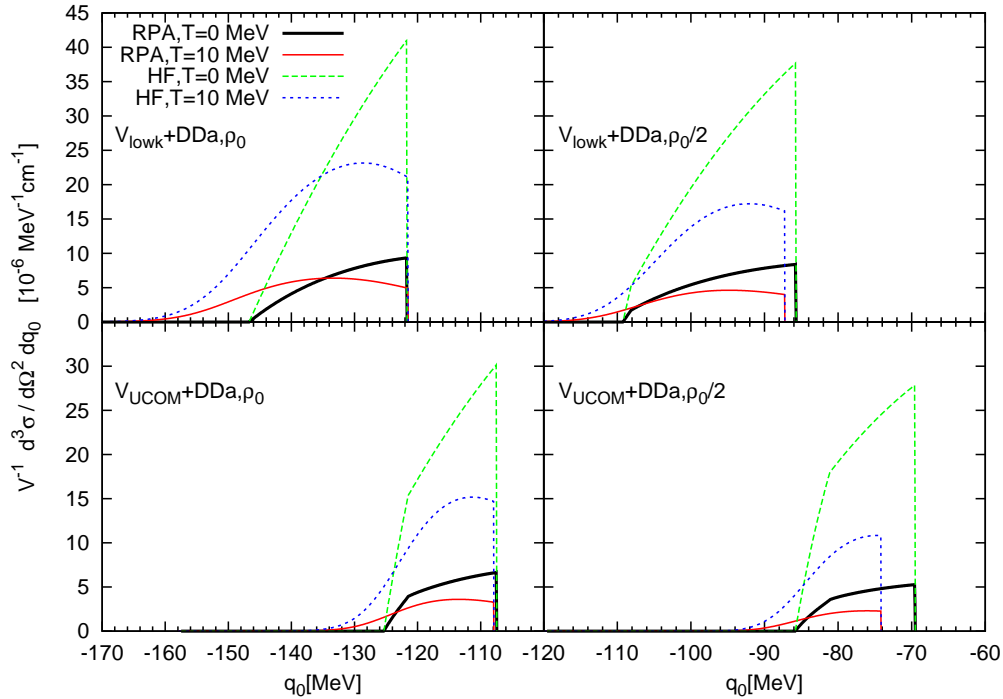
Figure 5.11: Neutrino charged current cross section in β-equilibrated dense matter with density-dependent interactions.

peratures, are shown in Fig. 5.13. In this figure it is easy to see that, as the increase of temperature opens up the phase space available for the cross sections, the mean free path decreases. The resulting increase will eventually lead to neutrinos being trapped inside the neutron star. However, it is clear to see that as the neutron star grows older and cools, the neutrinos will start to free stream out of it. Hence only young and hot neutron stars can be considered as possible environments for neutrino trapping.

The comparison between the left and the right side of Fig. 5.13 tells us that while the charged current contribution to the mean free path is slightly larger than the contribution of the neutral current they are of the same order of magnitude and both are equally important for the study of neutrino transport in dense matter. As for the differences between the Hartree-Fock and RPA calculations it is even more obvious than before that the main effect of the medium's response is the suppression of the cross section. One exception is the case for low densities in the neutral current where we see an enhancement in the RPA calculation. However
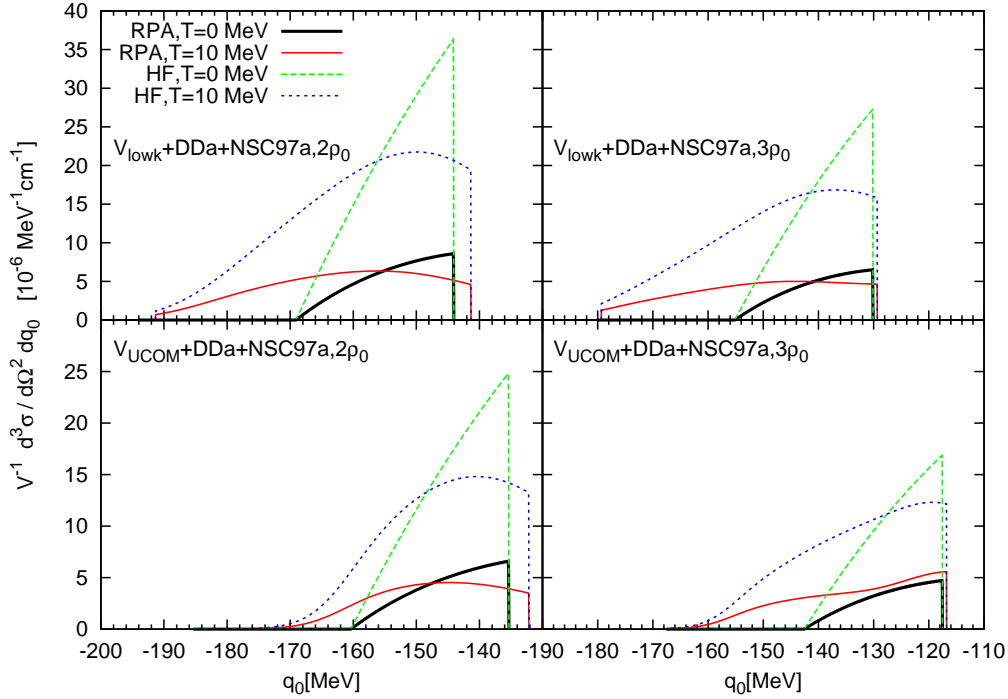
Figure 5.12: Neutrino charged current cross section in β-equilibrated dense matter with density-dependent interactions with the YN interaction from the NSC97a model.

if we recall that this is precisely the density at which F_0 becomes smaller than -1, cf. Fig. 4.5, we realize that this is where the approximation of infinite nuclear matter starts to breakdown. Hence, this effect should be considered with some scepticism and one wonders if Fermi liquid theory is valid in this density range.

The effects of hyperons on the neutrino mean free path in β-equilibrated dense matter with density-dependent interactions for several temperatures can be seen in Fig. 5.14. The results shown in this figure represent the Hartree-Fock calculation. It is clearly seen how the appearance of hyperons decreases the neutral current neutrino mean free path. Obviously different models with different hyperon threshold densities will start to affect the mean free path at different stages. By the time the density reaches $3\rho_0$ all models for which both Λ and Σ^- appear below this density give the same result. The model which only has a Λ at this density, χEFT600, is also the only model which differs from all others. If we exclude this model from our considerations we can conclude that at $3\rho_0$ the introduction
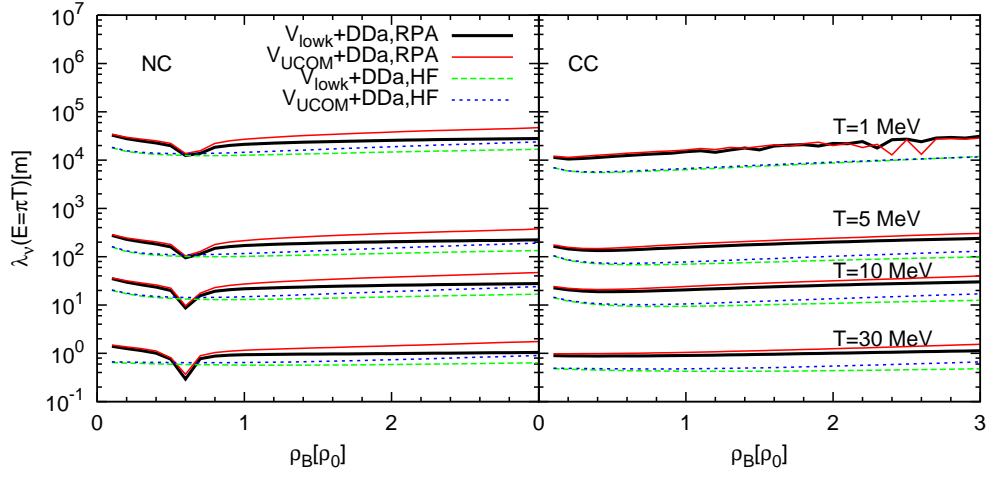
Figure 5.13: Neutrino mean free paths in symmetric nuclear matter with density-dependent interactions for several temperatures.
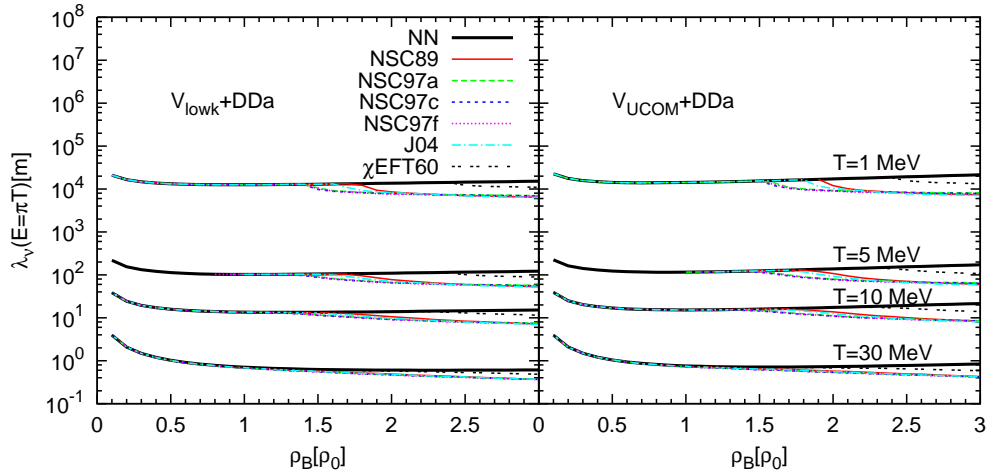

Figure 5.14: Neutral current neutrino mean free paths in β-equilibrated dense matter with density-dependent interactions for several temperatures. The results shown are for the Hartree-Fock calculation.

of hyperons leads to the factor of ~ 2 decrease in the mean free path compared to the pure nucleon case. This makes the neutrinos which are trapped at densities above which hyperons appear slightly longer trapped as the neutron star cools.
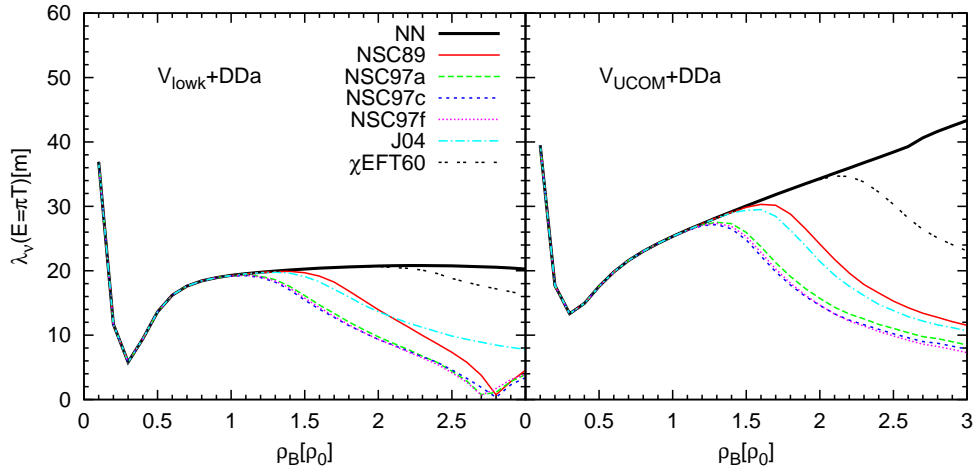

Figure 5.15: Neutral current neutrino mean free paths in β-equilibrated dense matter with density-dependent interactions for various YN interactions. The results shown are for the RPA calculation at $T = 10$ MeV.

The results of the RPA calculation are shown in Fig. 5.15. The figure displays the neutral current neutrino mean free path in β-equilibrated dense matter with density-dependent interactions for various YN interactions. The effects which we observe here are similar to those for all other temperatures so we focus on a temperature of $T = 10$ MeV. The enhancement at low densities that we saw in symmetric matter when considering Fig. 5.13, has now moved to density of $\sim 0.4\rho_0$, similar to the effect we saw when we plotted F_0 in β-equilibrium in Fig. 4.13.

An interesting difference is that for $V_{\text{low k}}$ without hyperons and V_{UCOM} the response functions have a different density dependence. If we look at Eq. (C.53) we see that the polarization function is directly proportional to the M^{*2} (for the neutral current case). Hence the faster decrease of the effective mass in the case of V_{UCOM}, which was observed in Fig. 4.4, explains this difference.

Fig. 5.16 displays the ratio of mean free paths in the RPA and Hartree-Fock calculations. The results shown are in β-equilibrated dense matter with density-dependent interactions for various YN interactions at a temperature of $T = 10$ MeV. This figure shows that the response of the $V_{\text{low k}}$ and V_{UCOM} combined
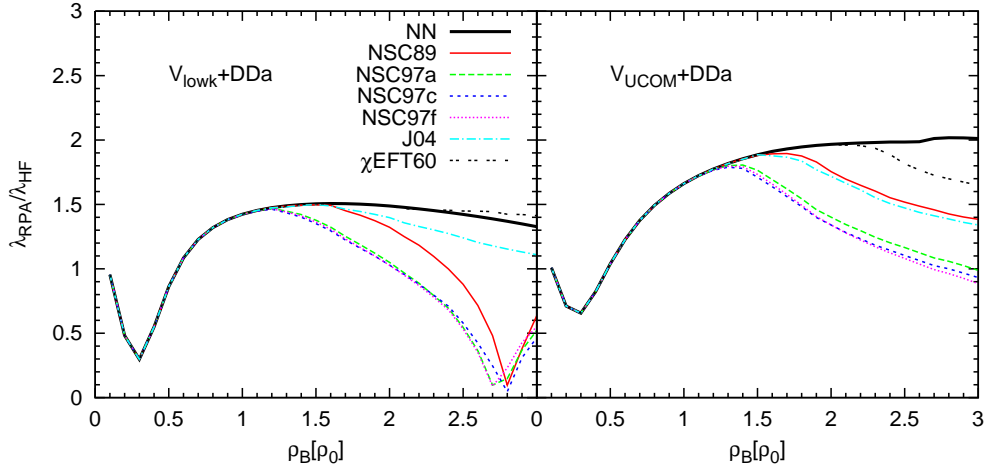
Figure 5.16: Ratio between the neutral current neutrino mean free paths for the RPA and the Hartree-Fock calculation. The result shown are in β-equilibrated dense matter with density-dependent interactions for various YN interactions at a temperature of $T = 10$ MeV.

with density-dependent interaction DDa is different even when combining them with hyperon interactions. It is obvious that the response of the medium with and without hyperons can be significantly dependent on the exact values of the Landau-Migdal parameters entering the kernel. For the most part in nucleonic matter the neutrino mean free path is suppressed but when we include hyperons this can clearly lead to significant enhancements. In fact, in the case of $V_{\text{low k}}$ some models lead to a drop in the mean free path between $(2-3)\rho_0$ by an order of magnitude. Such a large change, with the peak-like shape seen in Fig. 5.15, would lead to an accumulation of trapped neutrinos at this density range coming from deeper inside the neutron star. However as we did not study trapped neutrinos it is possible that once they are included such structures would disappear.

Fig. 5.17 shows the charged current neutrino mean free path in β-equilibrated dense matter with density-dependent interactions for various YN interactions. The calculation displayed was preformed in the RPA. The effects here are nowhere nearly as dramatic as in the case of the neutral current. Hence we do not show the result of the Hartree-Fock calculation, but refer to the same result for the symmetric matter shown in Fig. 5.13. The effect seen there is also true in β-equilibrated dense matter. The medium's response increases the mean free path through the suppression of the cross section. As for the effect of hyperon appearance, unlike
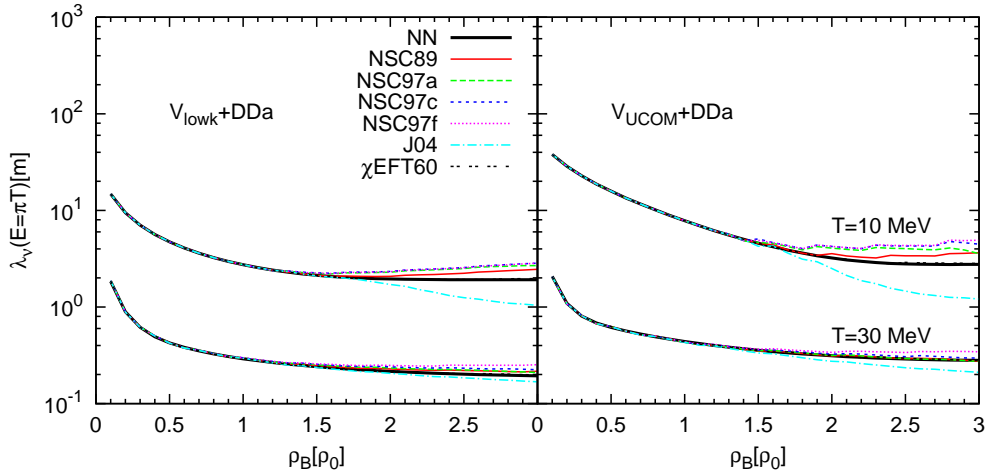
Figure 5.17: Charge current neutrino mean free path in β-equilibrated dense matter with density-dependent interactions for various YN interactions. The results shown are from the RPA calculation.

in the neutral current case, the YN models do not reach a common point by $3\rho_0$. Additionally the effect of hyperons compared to the pure nucleon case is not that large. The reason behind this effect is that in the case of the charged current the nucleonic contribution to the cross section is still by far the largest. The only way the hyperons affect the cross section is by changing the phase space through changes in the β-equilibrium. Hence the cross section may shift around from one energy range to the next but still remains dominated by nucleons.

In our discussion we have considered only electrons and their neutrinos. However, the neutral current results are more general and can be applied to all neutrino species. Additionally, all derivations of the cross sections from Appendix C can be easily extended to the case of the other lepton families. The same is true for antineutrinos, the only difference being that the concentrations of muons and τ-leptons, as well as of their antiparticles, are zero in cold neutron stars.

6 Summary and Conclusion

The construction of the hyperon-nucleon low-momentum effective potential, $V_{\text{low k}}$, allowed us to study the properties of hyperons in dense matter, together with properties of dense matter containing hyperons. The YN $V_{\text{low k}}$ potentials were constructed in a RG formalism from several bare potentials and applied to a nuclear matter calculation. The starting point of the nuclear matter calculation, after determination of the matrix elements of $V_{\text{low k}}$, was the single-particle potential of hyperons. Since $V_{\text{low k}}$ is an effective interaction, standard many-body technique can be directly applied.

As expected the results show only a limited degree of agreement and we were able to make only a few conclusions regarding the single-particle potential. One definite result was the attractive nature of the Λ single-particle potential in nuclear matter, although its exact behavior could not be ascertained. The differences in the results came from the inability to construct a unique YN interaction. This inability is not the fault of the $V_{\text{low k}}$ method, but the rather unfortunate consequence of incomplete and low precision of data available for YN scattering.

However, we took this situation as an opportunity to study all possible outcomes of different hyperon single-particle potentials. In essence it is highly unlikely that *all* of the potentials presented here will turn out to be incorrect, hence the *truth* definitely lies within the range of possibilities explored in this thesis. Which of these potentials gives a true description will hopefully be decided in the not-so-distant future. The planned experiments at the J-PARC and FAIR facilities are certainly going to give us some significant pointers in this direction. The simple addition of some much needed scattering data would bring us, in the YN sector, closer to the high quality situation which already exists for the NN sector. Any further development in this area is then dependent on more experimental data, but we have developed a reliable method which can be easily implemented as soon as such data is available.

After the introduction of the YN single-particle potential we proceeded to the calculation of the energy per particle in nuclear matter. In this case it turned out that the NN $V_{\text{low k}}$ potential was not well suited for the study of dense matter. Even when combining it with an appropriate three-body force from chiral perturbation theory, the properties of nuclear matter were not reproduced with sufficient

quality. Thus we proceeded to replace the nucleonic part of the equation of state with a parametrization. The parameters made it possible to study a wide range of equations of state. This broadness, in addition to the multitude of different YN potentials used makes us confident that the conclusions drawn here are as reliable as possible.

The primary result of this study is that strangeness will appear, via either the Σ^- or Λ, at around twice the saturation density of nuclear matter. This is not an unexpected result since other studies in this area drew the same conclusion, but never before has anyone studied such a range of equations of state in combination with so many different potentials. Hence, any study of neutron stars must find a way to either include hyperons or to find a solid reason for excluding them. Unfortunately the results on neutron star masses were not in agreement with the observed masses of known pulsars. However, this is a known side-effect of neglecting YY interactions and does not make our statement of hyperon appearance any less correct.

However, the parametrization introduced made it impossible to study the responses of matter to the neutrino probe. Hence we returned back to the microscopic interaction for the NN interaction and introduced a density-dependent force in order to mimic the effects of higher-order contributions. This force was then used in combination with the effective NN potentials ($V_{\text{low k}}$ and V_{UCOM}) and fitted to the properties of nuclear matter. Once fixed, the density-dependent force was used to calculate the Landau-Migdal parameters. These parameters served as input to the calculation of the medium's response to an external probe. They describe the strength of the interaction between the interacting particle-hole states.

A straightforward extension to the nuclear matter calculations performed in this thesis, which would apply to all considered quantities, is the inclusion of higher order terms in the perturbative expansion. Such an extension is natural given the fact that we are using *soft* effective potentials and should thus be described perturbatively. This would give contributions beyond that of Hartree-Fock for all quantities, ranging from the energy per particle over the single-particle potential, to the Landau-Migdal parameters. In this way a residual interaction can be created which would surpass the calculation presented here and could be easily used for the study of the matter's response to neutrinos.

Once we determined the strength of the interaction we were able to calculate the response of the medium to an external probe. The external probe used was the neutrino and the medium's response was studied in two approximations: the Hartree-Fock approximation; and the RPA. In both cases we included hyperons and saw how the cross section for both neutral and charged currents was modified. In the case of the neutral current, the biggest effect was the opening up of new reaction channels leading to an increase of the cross section at small energy trans-

fers. At the same time the effect of hyperons on the charged cross section were not large. The only effects were indirect ones through the change of the electron chemical potential due to β-equilibrium.

For the difference between the medium's response in the Hartree-Fock approximation and the RPA, we saw how for the most part in the latter case the medium suppresses the cross section. The only exception was the appearance of strong peaks in the neutral current cross section. Those on the edge of the energy range came from the vector response and were signals of zero sound; while those at zero energy transfer came mostly from the axial response. The latter peaks from the axial response were only noticeable in the case of finite temperature, since for zero temperature Pauli blocking leads to a complete suppression.

Finally, we used the neutrino mean free path to examine how it was influenced by changes in the cross section. As expected, the inclusion of hyperons led to a decrease of the mean free path. The conclusions when the RPA was included were not so clear, but for the most part it led to a decrease of the mean free path. This was not unexpected since we noticed the suppression as the dominate effect of the RPA for cross sections. However in the cases where an axial response led to great increase of hyperon contributions to the cross section, we saw a strong decrease of the mean free path. Such effects could be significant for neutron stars as it would mean that neutrinos stay trapped inside the star for longer times, i.e until lower temperatures.

A Appendix A

A.1 Lippmann-Schwinger equation

In order to mathematically formulate the scattering process we start from the total Hamiltonian H and assume that it can be separated as

$$H = H_0 + V \,, \tag{A.1}$$

where H_0 is the free (unperturbed) Hamiltonian. We will apply H to states which have the same energy spectrum as free states, i.e.

$$H_0 \ket{\phi} = E \ket{\phi} \,. \tag{A.2}$$

Then the Schrödinger equation we have to solve is

$$H \ket{\psi} = (H_0 + V) \ket{\psi} = E \ket{\psi} \,, \tag{A.3}$$

where $\ket{\phi}$ is the eigenvector of H_0, $\ket{\psi}$ is eigenvector of H, and E is an eigenvalue of both H and H_0.

The desired solution of Eq. (A.3) is then

$$\ket{\psi} = \frac{1}{E - H_0} V \ket{\psi} + \ket{\phi} \,, \tag{A.4}$$

and is known as the Lippmann-Schwinger equation [81].

The transition operator T is defined such that

$$V \ket{\psi} = T \ket{\phi} \,. \tag{A.5}$$

If we multiply Eq. (A.4) with V and apply Eq. (A.5) we obtain

$$T \ket{\phi} = V \ket{\phi} + V \frac{1}{E - H_0 + i\epsilon} T \ket{\phi} \tag{A.6}$$

which is the operator form of the Lippmann-Schwinger equation since it is valid for any complete set of orthogonal states $\ket{\phi}$.

A.2   Single particle states

A single-particle state of a fermion is denoted by $|i\rangle$ where i represents the complete set of quantum numbers (spin, isospin momentum, etc.). They are normalized such that

$$\langle i|j\rangle = \delta_{ij} \,. \tag{A.7}$$

The completeness relationship of single-particle states is expressed by the outer product

$$\sum_i |i\rangle \langle i| = 1 \,. \tag{A.8}$$

In the case of continuous quantum numbers one must use the Dirac delta function instead of the Kronecker delta and replace the summation with the integration or a combination of both in the case of mixed discret and continuous quantum numbers.

A.3   Plane waves

An appropriate one-particle plane wave state can be labeled by momentum $\vec{p}$, spin(isospin) $s(t)$ and spin(isospin) projection $m_s(m_t)$. Thus we have

$$|\vec{p}, s\, m_s, t\, m_t\rangle = |\vec{p}\rangle \otimes |sm_s\rangle \otimes |tm_t\rangle \,, \tag{A.9}$$

with the normalization and completeness as defined above with momentum being continuous. A fully antisymmetrized two-particle state can then be constructed as:

$$|\vec{p_1}, s_1\, m_{s_1}, t_1\, m_{t_1}; \vec{p_2}, s_2\, m_{s_2}, t_2\, m_{t_2}\rangle = \tag{A.10}$$

$$\frac{|\vec{p_1}, s_1\, m_{s_1}, t_1\, m_{t_1}\rangle\, |\vec{p_2}, s_2\, m_{s_2}, t_2\, m_{t_2}\rangle - |\vec{p_2}, s_2\, m_{s_2}, t_2\, m_{t_2}\rangle\, |\vec{p_1}, s_1\, m_{s_1}, t_1\, m_{t_1}\rangle}{\sqrt{2}} \,.$$

A.4   Partial waves

In the partial-wave basis a two-particle state can be expressed as:

$$\left|\vec{P}p(LS)JM_J t_1 m_{t_1} t_2 m_{t_2}\right\rangle = \left|\vec{P}p(LS)JM_J\right\rangle \otimes |t_1 m_{t_1} t_2 m_{t_2}\rangle \,, \tag{A.11}$$

where the $\vec{P}$ is the total momentum of the system, $p = |\vec{p}|$ is the magnitude of the relative momentum, L is the orbital angular momentum, S is the total spin, J is the total angular momentum and M_J is its projection. [1]

---

[1]Isospin can be coupled in a similar fashion but we refrain from doing it since we want to keep the isospin dependence explicit.

Since the total momentum is always conserved we will drop it from the further considerations. The partial-wave states are normalized as

$$\langle p(LS)JM_Jt_1m_{t_1}t_2m_{t_2}|p'(L'S')J'M_{J'}t_1'm_{t_1'}t_2'm_{t_2'}\rangle =$$
$$\frac{\pi}{2pp'}\delta(p-p')\delta_{LL'}\delta_{SS'}\delta_{JJ'}\delta_{M_JM_J'}\delta_{t_1t_1'}\delta_{m_{t_1}m_{t_1'}}\delta_{t_2t_2'}\delta_{m_{t_2}m_{t_2'}}\,,\qquad(A.12)$$

with the completeness relation as

$$\frac{2}{\pi}\sum_{(LS)JM_Jt_1m_{t_1}t_2m_{t_2}}\int p^2dp\,|p(LS)JM_Jt_1m_{t_1}t_2m_{t_2}\rangle$$
$$\langle p(LS)JM_Jt_1m_{t_1}t_2m_{t_2}|=1\,.\qquad(A.13)$$

A.5   Change of basis (plane wave to partial wave)

We can take two single-particle states described by Eq. (A.9) and couple them to create the above defined two-particle state in the partial-wave basis Eq. (A.11). We first couple the momenta by transferring to the center of mass reference frame. The total and the relative momenta of a system of two particles, in the center of mass frame, are given by

$$\vec{P} = \vec{p}_1 + \vec{p}_2\,,\qquad(A.14)$$
$$\vec{p} = \frac{m_1}{m_1+m_2}\vec{p}_2 - \frac{m_2}{m_1+m_2}\vec{p}_1\,,\qquad(A.15)$$

where m_1 and m_2 are the masses of the particles. The inverse of these relationships is than given by

$$\vec{p}_1 = \frac{m_1}{m_1+m_2}\vec{P} - \vec{p}\,,\qquad(A.16)$$
$$\vec{p}_2 = \frac{m_2}{m_1+m_2}\vec{P} + \vec{p}\,,\,.\qquad(A.17)$$

The coupling of spins proceeds in the usual fashion through the Clebsh-Gordan coefficients:

$$|SM_S\rangle = \sum_{m_{s_1}m_{s_2}}\left(\begin{array}{cc|c}s_1 & s_2 & S\\ m_{s_1} & m_{s_2} & M_S\end{array}\right)|s_1m_{s_1}\rangle|s_2m_{s_2}\rangle\,,\qquad(A.18)$$

$$|s_1m_{s_1}\rangle|s_2m_{s_2}\rangle = \sum_{SM_S}\left(\begin{array}{cc|c}s_1 & s_2 & S\\ m_{s_1} & m_{s_2} & M_S\end{array}\right)|SM_S\rangle\,.\qquad(A.19)$$

We then transform the relative momentum to a basis involving the magnitude of this momentum, orbital angular momentum and its projection.

$$|\vec{p}\rangle = \sqrt{\frac{2}{\pi}} \sum_{LM_L} |pLM_L\rangle \left\langle LM_L | \hat{\vec{p}} \right\rangle = \sqrt{\frac{2}{\pi}} \sum_{LM_L} |p\,LM_L\rangle \, Y^*_{LM_L}(\hat{\vec{p}}), \qquad (A.20)$$

where $Y_{LM_L}(\hat{\vec{p}})$ are spherical harmonics and $\hat{\vec{p}}$ is a unit vector in the direction of $\vec{p}$. What remains is to couple the orbital angular momentum and the total spin into total angular momentum. Then we have

$$|\vec{p}_1, s_1 m_{s_1}, t_1 m_{t_1}\rangle \, |\vec{p}_2, s_2 m_{s_2}, t_2 m_{t_2}\rangle = \sqrt{\frac{2}{\pi}} \sum_{SM_S} \sum_{LM_L} \sum_{J} \left(\begin{array}{cc|c} s_1 & s_2 & S \\ m_{s_1} & m_{s_2} & M_S \end{array} \right)$$

$$Y^*_{LM_L}(\hat{\vec{p}}) \left(\begin{array}{cc|c} L & S & J \\ M_L & M_S & M_L + M_S \end{array} \right) |p(LS)JM_J t_1 m_{t_1} t_2 m_{t_2}\rangle. \qquad (A.21)$$

The sum over M_J has been suppressed because of the relation $M_J = M_L + M_S$.

A.6   Lippmann-Schwinger equation in the partial-wave basis

If we use the partial wave states defined by Eq. (A.12) and Eq. (A.13) and evaluate the operator form of the Lippmann-Schwinger equation Eq. (A.6) we arrive at the form of the Lippmann-Schwinger equation in partial wave basis:

$$T^{\alpha'\alpha}_{k,y'y}(q',q;q^2) = V^{\alpha'\alpha}_{k,y'y}(q',q) +$$

$$\frac{2}{\pi} \sum_{\beta,z} P \int_0^{\inf} dl \, l^2 \frac{V^{\alpha'\beta}_{k,y'z}(q',l) T^{\beta\alpha}_{k,zy}(l,q;q^2)}{E_y(q) - E_z(l)}. \qquad (A.22)$$

The labels y, z indicate the particle channels, e.g. $y = YN$, and α, β denote the partial waves, e.g. $\alpha = LSJ$ where L is the angular momentum, J the total momentum and S the spin. In this equation the energies are given by

$$E_y(q) = M_y + \frac{q^2}{2\mu_y}, \qquad (A.23)$$

with the reduced mass $\mu_y = M_Y M_N / M_y$ and the total mass $M_y = M_Y + M_N$ of the hyperon M_Y and the nucleon M_N.

In the basis defined by Eq. (A.12) the transition operator is seen to couple various spin and isospin channels. However we are not completely free in the choice

of these couplings. Our choices are limited by the need to satisfy various conservation laws. This will reduce the complete matrix, which one can construct with discret indices, into several smaller parts which do not couple with one another.

Let us first examine all possible states we have. Obviously one does not need to consider the total angular momentum J since it is conserved. But for the total spin and angular momentum we have the spin singlet states $S = 0$ with $L = J$ and the spin triplet states $S = 1$ with $L = J + 1$ or $L = J$ or $L = J - 1$. This would then give a 4×4 matrix in this space but parity conservation reduces this to two 2×2 matrices. If we suppress all other indices in addition to momentum we can write them as:

$$
\begin{pmatrix} T^{0J0J} & T^{0J1J} \\ T^{1J0J} & T^{1J1J} \end{pmatrix}, \qquad \begin{pmatrix} T^{1J-11J-1} & T^{1J-11J+1} \\ T^{1J+11J-1} & T^{1J+1J+1} \end{pmatrix} . \tag{A.24}
$$

Here the first matrix represents the singlet-triplet coupling and the second one is the triplet-triplet coupling [2].

As for the isospin indices y, if we restrict ourselves to combinations of the form YN, we have four possibilities for Y and two for N, which give us eight possibilities for y. This would result in an 8×8 matrix in this representation, but like in the previous case we also have a conservation law to consider. Here it is the conservation of charge which limits the possible couplings, so instead of one 8×8 matrix we have two 1×1 matrices, for charge $+2$ and -1, and two 3×3 matrices, for charge 1 and 0. Now, if we suppress all indices except isospin we can write these matrices as:

$$
(T_{\Sigma^+ p \Sigma^+ p}), \begin{pmatrix} T_{\Lambda p \Lambda p} & T_{\Lambda p \Sigma^+ n} & T_{\Lambda p \Sigma^0 p} \\ T_{\Sigma^+ n \Lambda p} & T_{\Sigma^+ n \Sigma^+ n} & T_{\Sigma^+ n \Sigma^0 p} \\ T_{\Sigma^0 p \Lambda p} & T_{\Sigma^0 p \Sigma^+ n} & T_{\Sigma^0 p \Sigma^0 p} \end{pmatrix},
$$

$$
\begin{pmatrix} T_{\Lambda n \Lambda n} & T_{\Lambda n \Sigma^0 n} & T_{\Lambda n \Sigma^- p} \\ T_{\Sigma^0 n \Lambda n} & T_{\Sigma^0 n \Sigma^0 n} & T_{\Sigma^0 n \Sigma^- p} \\ T_{\Sigma^- p \Lambda n} & T_{\Sigma^- p \Sigma^0 n} & T_{\Sigma^- p \Sigma^- p} \end{pmatrix}, (T_{\Sigma^- n \Sigma^- n}) . \tag{A.25}
$$

A.7   Numerics

Here we show a few details regarding the numerical solution of Eq. (1.1). In this section for the sake of brevity we will suppress the subscript *low k* for all operators since from this point on all operators will be those of low momentum.

In order to be able to calculate the T-matrix numerically it is necessary that we derive an expression for it which is suitable for a numerical use. Here several

---

[2]For the NN potential there is no singlet-triplet coupling since the off-diagonal matrix elements T^{0J1J} and T^{1J0J} do not exist.

problems arise, but two are the main ones: the recurrent nature of the Lippmann-Schwinger equation and the principal value nature of the integral that appears. There are several ways to do this. Here we will essentially follow the prescription used in [82] with necessary changes made to account for the multichannel Lippmann-Schwinger equation that we have instead of the single-channel equation used in [82].

Starting from Eq. (A.22), first we add and subtract an expression which is conveniently designed so we get rid of the principal value integral. This additional expression is easily simplified

$$
\begin{aligned}
T^{\alpha'\alpha}_{y'y}(q',q;q^2) = {} & V^{\alpha'\alpha}_{y'y}(q',q) \\
& + \frac{2}{\pi} \sum_{\beta,z} \int_0^\Lambda dl \frac{l^2 V^{\alpha'\beta}_{y'z}(q',l) T^{\beta\alpha}_{zy}(l,q;q^2) - E_0^2 V^{\alpha'\beta}_{y'z}(q',E_0) T^{\beta\alpha}_{zy}(E_0,q;q^2)}{E_y(q) - E_z(l)} \\
& + \frac{2}{\pi} \sum_{\beta,z} V^{\alpha'\beta}_{y'z}(q',E_0) T^{\beta\alpha}_{zy}(E_0,q;q^2) P \int_0^\Lambda dl \frac{E_0^2}{E_y(q) - E_z(l)} \, ,
\end{aligned} \tag{A.26}
$$

where we use the abbreviation $E_0^2 = 2\mu_z \left(M_y + \frac{q^2}{2\mu_y} - M_z \right)$. As one can notice the first integral is no longer a principal value integral, but an ordinary integral, and the second one is analytically solvable. First let us solve the second integral,

$$
P \int_0^\Lambda \frac{E_0^2 dl}{E_y(q) - E_z(l)} = -P \int_0^\Lambda \frac{2\mu_z E_0^2 dl}{l^2 - E_0^2} = -\mu_z E_0 \ln \frac{\Lambda - E_0}{\Lambda + E_0} \, . \tag{A.27}
$$

The other integral needs to be solved numerically so we use Gaussian quadrature

$$
\int_0^\Lambda dl F(l) = \sum_{j=1}^N F(l_j) \omega_j \, , \tag{A.28}
$$

to represent the integration as a discrete sum, where ω_j are the appropriate weights. Now we use these two results in Eq. (A.26) to yield:

$$
\begin{aligned}
T^{\alpha'\alpha}_{y'y}(q',q;q^2) = {} & V^{\alpha'\alpha}_{y'y}(q',q) \\
& + \frac{2}{\pi} \sum_{\beta,z} \sum_{j=1}^N \frac{l_j^2 V^{\alpha'\beta}_{y'z}(q',l_j) T^{\beta\alpha}_{zy}(l_j,q;q^2) - E_0^2 V^{\alpha'\beta}_{y'z}(q',E_0) T^{\alpha'\alpha}_{zy}(E_0,q;q^2)}{E_y(q) - E_z(l_j)} \omega_j \\
& - \sum_{\beta,z} V^{\alpha'\beta}_{y'z}(q',E_0) T^{\beta\alpha}_{zy}(E_0,q;q^2) \frac{2\mu_z}{\pi} E_0 \ln \frac{\Lambda - E_0}{\Lambda + E_0} \, .
\end{aligned} \tag{A.29}
$$

From here we easily find

$$
\begin{aligned}
V_{y'y}^{\alpha'\alpha}(q',q) = \sum_{j=1}^{N+1}\sum_{\beta,z}\Big[& \delta_{ij}\delta_{y'z}\delta_{\alpha'\beta} + \omega_j' V_{y'z}^{\alpha'\beta}(q',l_j) \\
& + \delta_{jN+1} V_{y'z}^{\alpha'\beta}(q',l_j)\frac{2\mu_z}{\pi}k_{N+1}\ln\frac{\Lambda - k_{N+1}}{\Lambda + k_{N+1}}\Big] T_{zy}^{\beta\alpha}(l_j,q)\,,
\end{aligned}
\tag{A.30}
$$

where we define the new weights ω_j' as:

$$
\omega_j' = \begin{cases} -\frac{2}{\pi}\frac{l_j^2\omega_j}{E_y(q)-E_z(l_j)} & for \quad j \neq N+1 \\ \frac{2}{\pi}\sum_{m=1}^{N}\frac{k_{N+1}^2\omega_m}{E_y(q)-E_z(l_m)} & for \quad j = N+1 \end{cases}\,,
\tag{A.31}
$$

and replaced $E_0 = k_{N+1}$.

Hence through matrix inversion we can calculate the T-matrix as

$$
T_{y'y}^{\alpha'\alpha}(q',q;q^2) = \sum_{j=1}^{N+1}\sum_{\beta,z}\left(F_{y'z}^{\alpha'\beta}(q',l_j)\right)^{-1} V_{zy}^{\beta\alpha}(l_j,q)\,,
\tag{A.32}
$$

where

$$
\begin{aligned}
F_{y'z}^{\alpha'\beta}(q',l_j) = & \,\delta_{ij}\delta_{y'z}\delta_{\alpha'\beta} + \omega_j' V_{y'z}^{\alpha'\beta}(q',l_j) \\
& + \delta_{jN+1} V_{y'z}^{\alpha'\beta}(q',l_j)\frac{2\mu_z}{\pi}k_{N+1}\ln\frac{\Lambda - k_{N+1}}{\Lambda + k_{N+1}}\,.
\end{aligned}
\tag{A.33}
$$

We also note that since we are dealing with the half-on-shell T-matrix we have to keep in mind that the entire matrix needs to be on-shell simultaneously and that there is a common energy E to which all energies of the individual channels are equal to. This will have no influence on coupled channels in which the masses are equal such as Eq. (A.24), but in channels where the masses are not equal such as Eq. (A.25) we have to correct the on-shell value of the corresponding momentum. Thus our cut-off Λ will not be the same for all channels. If we use the lightest channel to set the cut-off, then the other channels have to be changed according to the following formula

$$
\Lambda_y = \sqrt{2\mu_y(E - M_y)} = \sqrt{2\mu_y(M_{y'} + \frac{\Lambda^2}{2\mu_{y'}} - M_{y'})}\,.
\tag{A.34}
$$

For the charge equal to zero the lightest channel is Λn, so we have $\Lambda_{\Lambda n} = \Lambda$. For charge equal one we have $\Lambda_{\Lambda p} = \Lambda$.

This effect is easy to understand if one considers the off-diagonal elements of the T-matrix in Eq. (A.25) such as $T_{\Lambda p\Sigma^+n}$. Here it is obvious that it is the energy and not the momentum which is conserved by the transition operator. More details on solving a multi-channel integral equation of Fredholm type can be found in [83].

B Appendix B

B.1 Hartree-Fock ground-state energy

In the Hartree-Fock approximation the Hamiltonian of the system is composed of the mass, a kinetic and a potential part [84]:

$$\hat{H} = \hat{M} + \hat{T} + \hat{V} \, . \tag{B.1}$$

In Hartree-Fock theory, the states of a homogenous and isotropic system are given by plane waves

$$\left\langle \vec{k}_i | \vec{r} \right\rangle = \frac{1}{\sqrt{\Omega}} e^{-i\vec{k}_i \cdot \vec{r}} \, , \tag{B.2}$$

where $\vec{k}_i$ is the momentum and $\vec{r}$ is the position of the system. Ω represents the volume of the system. The complete set of states is then

$$|\nu_i\rangle = \left| \vec{k}_i \right\rangle \otimes |sm_s\rangle \otimes |tm_t\rangle = \frac{1}{\sqrt{\Omega}} e^{i\vec{p}\cdot\vec{r}} \chi_{sm_s} \chi_{tm_t} \, , \tag{B.3}$$

where $\chi_{sm_s}(\chi_{tm_t})$ denotes the spin (isospin) wave-function. For the volume of the system Ω we will take the $\Omega \to \infty$ limit. From the discrete momentum basis defined by Eq. (B.2) we need to go to a continuous basis defined by

$$\langle \vec{p} | \vec{r} \rangle = \frac{1}{(2\pi)^{3/2}} e^{-i\vec{p}\cdot\vec{r}} \, , \tag{B.4}$$

B.1.1   Mass and kinetic term

With these definitions of a continuous and discrete basis we now evaluate the one-body operators of mass and kinetic energy:

$$
\left\langle \Phi | \hat{M} | \Phi \right\rangle = \frac{\Omega}{(2\pi)^3} \sum_{s_1 m_{s_1} t_1 m_{t_1}} M_{s_1 m_{s_1} t_1 m_{t_1}} \int d^3 \vec{p}_1
$$

$$
= \frac{\Omega}{2\pi^2} \sum_{s_1 m_{s_1}} \sum_{t_1 m_{t_1}} M_{s_1 m_{s_1} t_1 m_{t_1}} \frac{p_{F_{s_1 m_{s_1} t_1 m_{t_1}}}^3}{3} \tag{B.5}
$$

$$
\left\langle \Phi | \hat{T} | \Phi \right\rangle = \frac{\Omega}{(2\pi)^3} \sum_{s_1 m_{s_1}} \sum_{t_1 m_{t_1}} \int d^3 \vec{p}_1 \frac{\vec{p_1^2}}{2 M_{s_1 m_{s_1} t_1 m_{t_1}}}
$$

$$
= \frac{\Omega}{4\pi^2} \sum_{s_1 m_{s_1}} \sum_{t_1 m_{t_1}} \frac{p_{F_{s_1 m_{s_1} t_1 m_{t_1}}}^5}{5 M_{s_1 m_{s_1} t_1 m_{t_1}}} \, . \tag{B.6}
$$

We can simplify this expression if we take into account that our environment is unpolarized and that it consists of nucleons and hyperons:

$$
\left\langle \Phi | \hat{M} | \Phi \right\rangle = \frac{\Omega}{\pi^2} \left(M_{00} \frac{p_{F_{00}}^3}{3} + \sum_{\frac{1}{2} m_{t_1}} M_{\frac{1}{2} m_{t_1}} \frac{p_{F_{\frac{1}{2} m_{t_1}}}^3}{3} \sum_{1 m t_1} M_{1 m_{t_1}} \frac{p_{F_{1 m_{t_1}}}^3}{3} \right)
$$

$$
= \frac{\Omega}{\pi^2} \left(M_\Lambda \frac{p_{F_\Lambda}^3}{3} + \sum_N M_N \frac{p_{F_N}^3}{3} \sum_\Sigma M_\Sigma \frac{p_{F_\Sigma}^3}{3} \right) \tag{B.7}
$$

$$
\left\langle \Phi | \hat{T} | \Phi \right\rangle = \frac{\Omega}{2\pi^2} \left(\frac{p_{F_{00}}^5}{5 M_{00}} + \sum_{\frac{1}{2} m_{t_1}} \frac{p_{F_{\frac{1}{2} m_{t_1}}}^5}{5 M_{\frac{1}{2} m_{t_1}}} + \sum_{1 m_{t_1}} \frac{p_{F_{1 m_{t_1}}}^5}{5 M_{1 m_{t_1}}} \right)
$$

$$
= \frac{\Omega}{2\pi^2} \left(\frac{p_{F_\Lambda}^5}{5 M_\Lambda} + \sum_N \frac{p_{F_N}^5}{5 M_N} + \sum_\Sigma \frac{p_{F_\Sigma}^5}{5 M_\Sigma} \right) \, . \tag{B.8}
$$

B.1.2   Potential term

The potential part is a two-body operator which, in the plane-wave basis, is evaluated as:

$$
\left\langle \hat{V} \right\rangle = \frac{1}{2} \sum_{s_1 m_{s_1}} \sum_{s_2 m_{s_2}} \sum_{t_1 m_{t_1}} \sum_{t_2 m_{t_2}} \sum_{\vec{p}_1} \sum_{\vec{p}_2} \tag{B.9}
$$

$$
\left(\vec{p}_1, s_1 m_{s_1}, t_1 m_{t_1}; \vec{p}_2, s_2 m_{s_2}, t_2 m_{t_2} \right| V \left| \vec{p}_1, s_1 m_{s_1}, t_1 m_{t_1}; \vec{p}_2, s_2 m_{s_2}, t_2 m_{t_2} \right) \, ,
$$

where the fully antisymmetric state can be expressed with the help of an exchange operator P_{ij} as

$$|\vec{p}_1, s_1 m_{s_1}, t_1 m_{t_1}; \vec{p}_2, s_2 m_{s_2}, t_2 m_{t_2}) = \frac{(1 - P_{12})}{\sqrt{2}} |\vec{p}_1, s_1 m_{s_1}, t_1 m_{t_1}\rangle |\vec{p}_2, s_2 m_{s_2}, t_2 m_{t_2}\rangle .$$
(B.10)

We note that since $P_{ij}^2 = 1$ we have $(1 - P_{12})^2 = 2(1 - P_{12})$.

With help of [85]

$$\begin{pmatrix} L & S & \bigg| & J \\ M_L & M_S & \bigg| & M_J \end{pmatrix} = (-1)^{S+L-J} \begin{pmatrix} S & L & \bigg| & J \\ M_S & M_L & \bigg| & M_J \end{pmatrix} ,$$
(B.11)

and

$$Y^*_{LM_L}(-\hat{\vec{q}}) = (-1)^L Y^*_{LM_L}(\hat{\vec{q}}) ,$$
(B.12)

we can easily derive, from Eq. (A.21),

$$|\vec{p}_1, s_1 m_{s_1}, t_1 m_{t_1}; \vec{p}_2, s_2 m_{s_2}, t_2 m_{t_2}) =$$

$$\frac{1}{\sqrt{2}} \sqrt{\frac{2}{\pi}} \sum_{SM_S} \sum_{LM_L} \sum_J \begin{pmatrix} s_1 & s_2 & \bigg| & S \\ m_{s_1} & m_{s_2} & \bigg| & M_S \end{pmatrix} Y^*_{LM_L}(\hat{\vec{q}}) \begin{pmatrix} L & S & \bigg| & J \\ M_L & M_S & \bigg| & M_L + M_S \end{pmatrix}$$

$$\left[|p(LS)JM_J t_1 m_{t_1} t_2 m_{t_2}\rangle - (-1)^{1-S+L} |p(LS)JM_J t_2 m_{t_2} t_1 m_{t_1}\rangle \right] .$$
(B.13)

Now we can make a connection between the expectation value of the potential in the plane-wave basis and in the partial-wave basis as

$$(\vec{p}_1, s_1 m_{s_1}, t_1 m_{t_1}; \vec{p}_2, s_2 m_{s_2}, t_2 m_{t_2} | V | \vec{p}_1, s_1 m_{s_1}, t_1 m_{t_1}; \vec{p}_2, s_2 m_{s_2}, t_2 m_{t_2})$$

$$= \frac{2}{\pi} \sum_{SM_S} \sum_{LM_L} \sum_J \begin{pmatrix} s_1 & s_2 & \bigg| & S \\ m_{s_1} & m_{s_2} & \bigg| & M_S \end{pmatrix}^2 \begin{pmatrix} L & S & \bigg| & J \\ M_L & M_S & \bigg| & M_L + M_S \end{pmatrix}^2$$

$$Y_{LM_L}(\hat{\vec{q}}) Y^*_{LM_L}(\hat{\vec{q}}) \left[\langle q(LS)JM_J t_1 m_{t_1} t_2 m_{t_2} | V | q(LS)JM_J t_1 m_{t_1} t_2 m_{t_2}\rangle \right.$$

$$\left. - (-1)^{1-S+L} \langle q(LS)JM_J t_1 m_{t_1} t_2 m_{t_2} | V | q(LS)JM_J t_2 m_{t_2} t_1 m_{t_1}\rangle \right] .$$
(B.14)

In the end going from the discrete to the continuous basis,

$$\langle q(LS)JM_J t_1 m_{t_1} t_2 m_{t_2} | V | q(LS)JM_J t_1 m_{t_1} t_2 m_{t_2}\rangle = \frac{(2\pi)^3}{\Omega} V^{di}_{(LS)Jt_1 m_{t_1} t_2 m_{t_2}}(q) ,$$
(B.15)

$$\langle q(LS)JM_J t_1 m_{t_1} t_2 m_{t_2} | V | q(LS)JM_J t_2 m_{t_2} t_1 m_{t_1}\rangle = \frac{(2\pi)^3}{\Omega} V^{xc}_{(LS)Jt_1 m_{t_1} t_2 m_{t_2}}(q) ,$$
(B.16)

we get

$$(\vec{p}_1, s_1 m_{s_1}, t_1 m_{t_1}; \vec{p}_2, s_2 m_{s_2}, t_2 m_{t_2} | V | \vec{p}_1, s_1 m_{s_1}, t_1 m_{t_1}; \vec{p}_2, s_2 m_{s_2}, t_2 m_{t_2})$$

$$= \frac{(2\pi)^3}{\Omega} \frac{2}{\pi} \sum_{SM_S} \sum_{LM_L} \sum_J \left(\begin{array}{cc|c} 1/2 & 1/2 & S \\ m_{s_1} & m_{s_2} & M_S \end{array} \right)^2 \left(\begin{array}{cc|c} L & S & J \\ M_L & M_S & M_L + M_S \end{array} \right)^2$$

$$Y_{LM_L}(\hat{\vec{q}}) Y^*_{LM_L}(\hat{\vec{q}}) \left[V^{di}_{(LS)Jt_1 m_{t_1} t_2 m_{t_2}}(q) - (-1)^{1-S+L} V^{xc}_{(LS)Jt_1 m_{t_1} t_2 m_{t_2}}(q) \right] . \quad (B.17)$$

From here, by summing over spins and using

$$Y_{LM_L}(\theta, \phi) = (-1)^{M_L} \sqrt{\frac{2L+1}{4\pi} \frac{(L-M_L)!}{(L+M_L)!}} P_L^{M_L}(\cos\theta) e^{iM_L \phi} , \qquad (B.18)$$

we find,

$$\sum_{s_1 m_{s_1}} \sum_{s_2 m_{s_2}} (\vec{p}_1, s_1 m_{s_1}, t_1 m_{t_1}; \vec{p}_2, s_2 m_{s_2}, t_2 m_{t_2} | V | \vec{p}_1, s_1 m_{s_1}, t_1 m_{t_1}; \vec{p}_2, s_2 m_{s_2}, t_2 m_{t_2})$$

$$= \frac{(2\pi)^3}{\Omega} \frac{2}{\pi} \sum_{SM_S} \sum_{LM_L} \sum_J \left(\begin{array}{cc|c} L & S & J \\ M_L & M_S & M_L + M_S \end{array} \right)^2 \frac{2L+1}{4\pi} \frac{(L-M_L)!}{(L+M_L)!} (P_L^{M_L}(\cos\theta))^2$$

$$\left[V^{di}_{(LS)Jt_1 m_{t_1} t_2 m_{t_2}}(q) - (-1)^{s_1+s_2-S+L} V^{xc}_{(LS)Jt_1 m_{t_1} t_2 m_{t_2}}(q) \right] . \qquad (B.19)$$

Combining Eq. (B.9) and Eq. (B.19), as well as going from summation to integration $\sum \to \Omega/(2\pi)^3 \int$, we obtain

$$\langle V \rangle = \frac{\Omega}{\pi (2\pi)^3} \sum_{t_1 m_{t_1}} \left(\frac{M}{m_1} \right)^3 \sum_{t_2 m_{t_2}} \int d^3 \vec{p}_1 \int d^3 \vec{p}_2 \sum_{SM_S} \sum_{LM_L} \sum_J$$

$$\frac{2L+1}{4\pi} \frac{(L-M_L)!}{(L+M_L)!} \left(\begin{array}{cc|c} L & S & J \\ M_L & M_S & M_L + M_S \end{array} \right)^2 (P_L^{M_L}(\cos\theta))^2$$

$$\left[V^{di}_{(LS)Jt_1 m_{t_1} t_2 m_{t_2}}(q) - (-1)^{s_1+s_2-S+L} V^{xc}_{(LS)Jt_1 m_{t_1} t_2 m_{t_2}}(q) \right] . \qquad (B.20)$$

Finally we go from the integration over the single-particle momentum

$$\int d^3 \vec{p}_1 \int d^3 \vec{p}_2 = \qquad\qquad\qquad\qquad\qquad\qquad\qquad\qquad (B.21)$$

$$\int_0^{p_{F_1}} dp_1 p_1^2 \int_0^\pi d\theta_1 \sin\theta_1 \int_0^{2\pi} d\phi_1 \int_0^{p_{F_2}} dp_2 p_2^2 \int_0^\pi d\theta_2 \sin\theta_2 \int_0^{2\pi} d\phi_2 ,$$

to relative momentum with the transition from (p_2, θ_2, ϕ_2) to (q, θ, ϕ). This choice is arbitrary and we could equivalently have chosen to go from (p_1, θ_1, ϕ_1) to (q, θ, ϕ)

as well. From Eq. (A.15) we get

$$p_2 \cos \theta_2 = \frac{m_1 + m_2}{m_1} q \cos \theta - \frac{m_2}{m_1} p_1 \,, \tag{B.22}$$

$$p_2 \sin \theta_2 = \frac{m_1 + m_2}{m_1} q \sin \theta \,, \tag{B.23}$$

$$\phi_2 = \phi \,, \tag{B.24}$$

and this then gives

$$p_2^2 dp_2 \sin \theta_2 d\theta_2 d\phi_2 = \left(\frac{M}{m_1} \right)^3 q^2 dq \sin \theta d\theta d\phi \,. \tag{B.25}$$

The integrand in Eq. (B.20) is independent of all but one angle so we can perform the integration over θ_1, ϕ_1 and ϕ analytically which yields a factor of $8\pi^2$. Finally

$$\langle V \rangle = \frac{\Omega}{\pi^2} \sum_{t_1 m_{t_1}} \sum_{t_2 m_{t_2}} \int_0^{p_{F_1}} dp_1 p_1^2 \int_{-1}^{1} dt \int_{q_{min}}^{q_{max}} dq q^2 \sum_{SM_S} \sum_{LM_L} \sum_{J}$$

$$\frac{2L+1}{4\pi} \frac{(L - M_L)!}{(L + M_L)!} \left(\begin{array}{cc|c} L & S & J \\ M_L & M_S & M_L + M_S \end{array} \right)^2 (P_L^{M_L}(\cos \theta))^2$$

$$\left[V_{(LS)J t_1 m_{t_1} t_2 m_{t_2}}^{di}(q) - (-1)^{s_1 + s_2 - S + L} V_{(LS)J t_1 m_{t_1} t_2 m_{t_2}}^{xc}(q) \right] \,. \tag{B.26}$$

Limits of integration

The integration limits of relative momentum in Eq. (B.26) are derived from the requirement that the second particle momentum at vanishing temperature is smaller then the corresponding Fermi momentum ($|\vec{p}_2| \leq p_{F_2}$). Then from Eq. (A.15) after some algebra we find:

$$M^2 q^2 + m_2^2 p_1^2 + 2M m_2 q p_1 t - m_1^2 p_{F_2}^2 \leq 0 \,, \tag{B.27}$$

which has the solution for the relative momentum q

$$q^-(p_{F_2}, p_1, t) \leq q \leq q^+(p_{F_2}, p_1, t) \,,$$

with the definitions

$$q^\pm(p_{F_2}, p_1, t) = \frac{m_2}{M} \left[p_1 \cdot t \pm \sqrt{\frac{m_2^2}{m_1^2} p_{F_2}^2 - p_1^2(1 - t^2)} \right] \,. \tag{B.28}$$
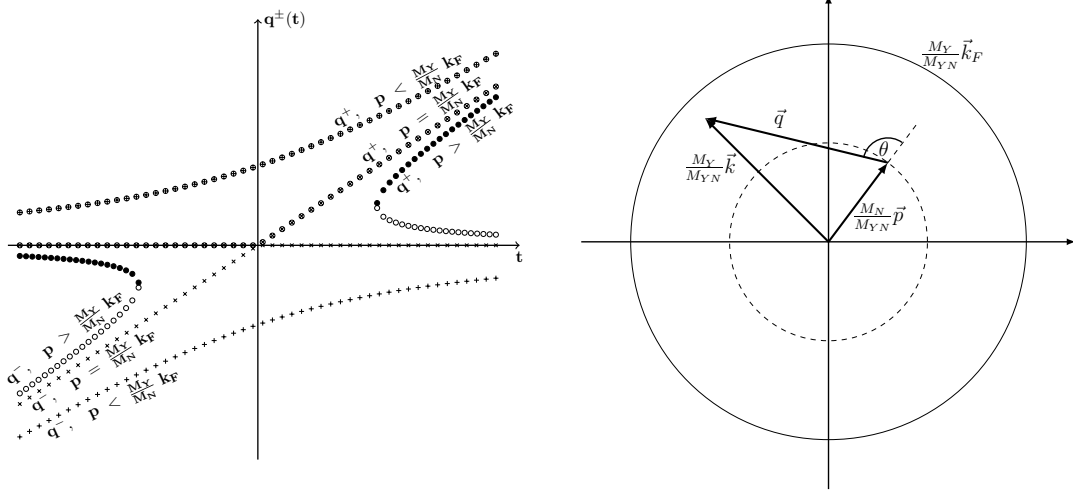
Figure B.1: Left: $q^{\pm}(p_{F_2}, p_1, t)$ as a function of t for different choices of p_1 and fixed p_{F_2}. Right: Schematic representation of the construction of the relative momentum $\vec{q}$ and its limits.

Since the relative momentum q is a real quantity this further constrains the integration variable t to

$$t \geq \sqrt{1 - \left(\frac{m_1}{m_2}\frac{p_{F_2}}{p_1}\right)^2}, \tag{B.29}$$

which is only valid if the hyperon momentum is $p_1 \geq \frac{m_1}{m_2}p_{F_2}$. In this case we finally determine the integration limits to be

$$t_{min} = \sqrt{1 - \left(\frac{m_1}{m_2}\frac{p_{F_2}}{p_1}\right)^2} \qquad ; \quad t_{max} = 1\,;$$
$$q_{min} = q^-(p_{F_2}, p_1, t) \qquad ; \quad q_{max} = q^+(p_{F_2}, p_1, t)\,, \tag{B.30}$$

because the modulus of t is always smaller than or equal to one.

For the case that the hyperon momenta $p_1 \leq \frac{m_1}{m_2}p_{F_2}$, the functions $q^{\pm}(p_{F_2}, p_1, t)$ are always real which then yields the integration limits

$$t_{min} = -1 \qquad ; \quad t_{max} = 1\,,;$$
$$q_{min} = 0 \qquad ; \quad q_{max} = q^+(p_{F_2}, p_1, t)\,. \tag{B.31}$$

In Fig. B.1 the integration limit functions $q^{\pm}$ are shown as functions of t for three different choices of the hyperon momentum $(p_1 < \frac{m_1}{m_2}p_{F_2}, p_1 > \frac{m_1}{m_2}p_{F_2}, p_1 = \frac{m_1}{m_2}p_{F_2})$ and a fixed k_F.

C Appendix C

C.1   Cross section

A cross section is defined by the probability to observe a particle in a given quantum state per unit solid angle if the target is irradiated by a flux of one particle per surface unit. To compute the cross section we need the transition probability.

C.2   Charge current cross section

The transition probability for a charged current process shown on the left of Fig. 5.1 is

$$T_{fi} = \langle \phi_l; \phi_\nu | \, \hat{T} \, | \phi_{B_2}; \phi_{B_4} \rangle \,.$$ (C.1)

The transition matrix consists of the lepton and hadron currents

$$\hat{T} = \hat{j}_\mu(x)\hat{J}^\mu(x) \,,$$ (C.2)

where the lepton current is given by

$$\hat{j}_\mu(k_f, s_f, \, k_i, s_i) = \hat{\bar{\psi}}'(k_f, s_f)\gamma_\mu(1 - \gamma_5)\hat{\psi}(k_i, s_i) \,,$$ (C.3)

and equivalently the hadron current is:

$$\hat{J}^\mu(p_f, S_f, \, p_i, S_i) = \hat{\bar{\Psi}}'(p_f, S_f)\gamma^\mu(V - A\gamma_5)\hat{\Psi}(p_i, S_i) \,.$$ (C.4)

The notation here is somewhat more general than in Chapter 5 because we will later refer to the same equation for the neutral current case.

The wave functions of the fermions are given by

$$\hat{\psi}_i(x) = \sum_{p_i} \hat{\psi}_i(p_i)e^{-ip_i \cdot x} = \sum_{s_i p_i} \left(\frac{m_i}{\Omega E_i} \right)^{1/2} c_{s_i}(p_i)u_{s_i}(p_i)e^{-ip_i \cdot x} \,,$$ (C.5)

where the spin sum results in the spinor completeness relation:

$$\sum_s [u_s(p)]_f [\bar{u}_s(p)]_a = \left(\frac{\not{p} + m}{2m}\right)_{fa}.$$

(C.6)

The calculation of the cross section would than require the calculation of the square of the transition matrix. However in our case it is useful to use the optical theorem instead the directly squaring the transition matrix.

C.2.1   Optical theorem

The optical theorem is a straightforward consequence of the unitarity of the S-matrix: $\hat{S}^\dagger \hat{S} = \hat{S} \hat{S}^\dagger = 1$. Inserting $\hat{S} = 1 + i\hat{T}$ we have

$$-i \left(\hat{T} - \hat{T}^\dagger\right) = \hat{T}T.$$

(C.7)

We use a complete set of states to evaluate the right-hand side:

$$\langle \phi_l; \phi_\nu | \hat{T}T | \phi_l'; \phi_\nu' \rangle = \sum_n \left(\prod_{i=1}^n \sum_{\phi_i}\right) \langle \phi_l; \phi_\nu | \hat{T} | \phi_i \rangle \langle \phi_i | T | \phi_l'; \phi_\nu'; \rangle.$$

(C.8)

For the case of forward scattering the optical theorem than has the form

$$Im\mathcal{M} \left(\phi_l; \phi_\nu \rightarrow \phi_l; \phi_\nu\right) = 2E_{\mathcal{A}} E_{\mathcal{B}} v_{rel} \sigma_{tot} \left(\phi_l; \phi_\nu \rightarrow all\right),$$

(C.9)

where the invariant matrix element $\mathcal{M}$ is defined by

$$\langle \phi_l; \phi_\nu | T | \phi_l'; \phi_\nu' \rangle = (2\pi)^{(4)} \delta^4 (p_l + p_\nu - p_l' - p_\nu') \mathcal{M} \left(\phi_l; \phi_\nu \rightarrow \phi_l'; \phi_\nu'\right).$$

(C.10)

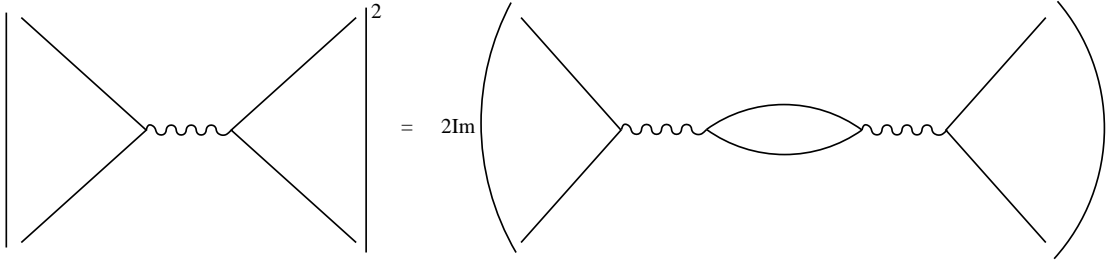The diagrammatical representation of the optical theorem is shown in Fig. C.1.

Figure C.1: Diagrammatical representation of the optical theorem.

C.2.2 Invariant matrix element

Let us now proceed with the calculation of the cross section. The quantity which we first need to calculate is the invariant matrix element of the process shown on the right-hand side of Fig. C.1. The momenta and energies of the particles are given by:

$$\vec{p}_{B_4} = \vec{p}_{B_2} + \vec{q},\qquad\qquad\text{(C.11)}$$

$$\vec{p}_l = \vec{p}_\nu - \vec{q},\qquad\qquad\text{(C.12)}$$

$$\imath\omega_{B_4} = \imath\omega_{B_2} + \imath q_0\,,\qquad\qquad\text{(C.13)}$$

$$\imath\omega_l = \imath\omega_\nu - \imath q_0\,.\qquad\qquad\text{(C.14)}$$

The labeling of the particle momenta and energy is obvious, with $\vec{q}$ the transferred momentum and q_0 the transferred energy.

Using the Feynman rules for momentum space from [33] we can immediately write down:

$$\mathcal{M}\left(\phi_l;\phi_\nu \rightarrow \phi_l;\phi_\nu\right) = -\frac{G_F^2}{2}\frac{m_\nu}{E_\nu}T\sum_{\omega_0(even)}T\sum_{\omega_{B_2}(odd)}\int\frac{d^3\vec{q}}{(2\pi)^3}\int\frac{d^3\vec{p}_{B_2}}{(2\pi)^3}\qquad\text{(C.15)}$$

$$\sum_{s_\nu}\left\{[\bar{u}_{s_\nu}(i\omega_\nu,\vec{p}_\nu)]_\gamma[\gamma_\mu(1-\gamma^5)]_{\gamma\delta}\left[S^l(i\omega_l,\vec{p}_l)\right]_{\delta\epsilon}[\gamma_\lambda(1-\gamma^5)]_{\epsilon\eta}[u_{s_\nu}(i\omega_\nu,\vec{p}_\nu)]_\eta\right\}$$

$$\left\{[\gamma^\mu(V-A\gamma^5)]_{\alpha'\alpha}[S^{B_4}(\imath\omega_{B_4},\vec{p}_{B_4})]_{\alpha\beta}[\gamma^\lambda(V-A\gamma^5)]_{\beta\beta'}[S^{B_2}(\imath\omega_{B_2},\vec{p}_{B_2})]_{\beta'\alpha'}\right\}$$

$$= -\frac{G_F^2}{4}\frac{1}{E_\nu}T\sum_{\omega_0(even)}T\sum_{\omega_{B_2}(odd)}\int\frac{d^3\vec{q}}{(2\pi)^3}\int\frac{d^3\vec{p}_{B_2}}{(2\pi)^3}L_{\mu\lambda}W^{\mu\lambda}\,.\qquad\text{(C.16)}$$

The lepton tensor is

$$L_{\mu\lambda} = \text{Tr}\left[S^l(i\omega_l,\vec{p}_l)\gamma_\mu(1-\gamma_5)\not{p}_\nu\gamma_\lambda(1-\gamma_5)\right]\,,\qquad\text{(C.17)}$$

where we have used the fact that the neutrino masses are practically zero.

If we neglect correlations between the leptons, or later for the neutral current neutrinos, we can use the relativistic propagator

$$S^l(i\omega_l,\vec{p}_l) = \frac{\not{p}_l + m}{p_l^2 - m^2 + i\epsilon}\,,\qquad\text{(C.18)}$$

to evaluate the trace and write the leptonic tensor as:

$$L_{\mu\lambda} = 8\frac{[(p_\nu)_\mu(p_l)_\lambda + (p_l)_\mu(p_\nu)_\lambda - g_{\mu\lambda}(p_l \cdot p_\nu) - i(p_l)_\alpha(p_\nu)_\beta\epsilon_{\alpha\mu\beta\lambda}]}{p_l^2 - m^2 + i\epsilon}\,.\qquad\text{(C.19)}$$

The hadronic tensor is given by

$$W^{\mu\lambda} = \text{Tr}\left[\gamma^\mu(V-A\gamma^5)S^{B_4}(\imath\omega_{B_4},\vec{p}_{B_4})\gamma^\lambda(V-A\gamma^5)S^{B_2}(\imath\omega_{B_2},\vec{p}_{B_2})\right]\,.\qquad\text{(C.20)}$$

From here it is easy to make the nonrelativistic approximation by:

$$[\gamma^\lambda(V - A\gamma^5)]_{\beta\beta'} \sim [g_V\delta_{0\lambda} + g_A\sigma^i\delta_{i\lambda}]_{\beta\beta'} . \qquad (C.21)$$

We note that the indices β and β' on the left side run through the values 1 to 4 while in the nonrelativistic case on the left side they go from 1 to 2.

The integral and the sum over particle B_2 in Eq. (C.16) can than be used to define the vector polarization function

$$\Pi_V^{\mu\lambda}(iq_0, \vec{q}) = T \sum_{\omega_{B_2}(odd)} \int \frac{d^3\vec{p}_{B_2}}{(2\pi)^3} g_V^2 \, \text{Tr}\left[S^{B_4}(\imath\omega_{B_4}, \vec{p}_{B_4}) S^{B_2}(\imath\omega_{B_2}, \vec{p}_{B_2})\right]\delta^{0\mu}\delta^{0\lambda} , \quad (C.22)$$

and the axial polarization function

$$\Pi_A^{\mu\lambda}(iq_0, \vec{q}) = T \sum_{\omega_{B_2}(odd)} \int \frac{d^3\vec{p}_{B_2}}{(2\pi)^3} g_A^2 \, \text{Tr}\left[S^{B_4}(\imath\omega_{B_4}, \vec{p}_{B_4})\sigma^i S^{B_2}(\imath\omega_{B_2}, \vec{p}_{B_2})\sigma^j\right]\delta^{i\mu}\delta^{j\lambda} .$$
$$(C.23)$$

For the the axial polarization function one can show that for spin-symmetric matter it simplifies to

$$\Pi_A^{\mu\lambda}(iq_0, \vec{q}) = T \sum_{\omega_{B_2}(odd)} \int \frac{d^3\vec{p}_{B_2}}{(2\pi)^3} g_A^2 \, \text{Tr}\left[S^{B_4}(\imath\omega_{B_4}, \vec{p}_{B_4}) S^{B_2}(\imath\omega_{B_2}, \vec{p}_{B_2})\right]\delta_{ij}\delta^{i\mu}\delta^{j\lambda} .$$
$$(C.24)$$

We can thus define a polarization function common to both vector and axial polarization functions as:

$$\tilde{\Pi}(iq_0, \vec{q}) = T \sum_{\omega_{B_2}(odd)} \int \frac{d^3\vec{p}_{B_2}}{(2\pi)^3} \text{Tr}\left[S^{B_4}(\imath\omega_{B_4}, \vec{p}_{B_4}) S^{B_2}(\imath\omega_{B_2}, \vec{p}_{B_2})\right] . \qquad (C.25)$$

Combining all of these results and putting them in the invariant matrix element Eq. (C.16) we find:

$$\mathcal{M}(\phi_l; \phi_\nu \to \phi_l; \phi_\nu) = - G_F^2 \int \frac{d^3\vec{q}}{(2\pi)^3} (1 - f_l(E_l)) \left(1 - \exp\left(\frac{-q_0 + \mu_2 - \mu_4}{T}\right)\right)^{-1}$$
$$[(1 + \cos\theta)\Pi_V(iq_0, \vec{q}) + (3 - \cos\theta)\Pi_A(iq_0, \vec{q})] , \qquad (C.26)$$

where we have used the approximation in which we neglect the masses of leptons compared to their momentum

$$(p_\nu)^\mu(p_l)_\mu = E_\nu \, E_l \left(1 - \frac{\vec{p}_\nu \cdot \vec{p}_l}{E_\nu \, E_l}\right) = E_\nu \, E_l(1 - \cos\theta) . \qquad (C.27)$$

With the aid of the conversion factor $(1 - \exp((-q_0 + \mu_2 - \mu_4)/T))^{-1}$ we define the structure function

$$Im\tilde{\Pi}(q_0, q) = -\frac{1}{2}\left(1 - \exp((-q_0 + \mu_2 - \mu_4)/T)\right)S(q_0, q),\qquad \text{(C.28)}$$

and the differential cross section is

$$\frac{1}{\Omega}\frac{d^3\sigma(E_\nu)}{d\Omega^2 dq_0} = \frac{G_F^2}{8\pi^3}E_l^2\left(1 - f_l(E_l)\left[(1 + \cos\theta)S_V^{cc}(q_0, q) + (3 - \cos\theta)S_A^{cc}(q_0, q)\right]\right.$$
$$\text{(C.29)}$$

Finally, the total cross section is defined by

$$\frac{\sigma(E_1)}{\Omega} = \int d\Omega^2 q_0^2 dq_0 \frac{1}{\Omega}\frac{d^3\sigma(E_\nu)}{d\Omega^2 dq_0}.\qquad \text{(C.30)}$$

C.2.3 Neutral current cross section

The case for the neutral current is somewhat simpler since the incoming and outgoing particles are the same. The transition matrix element is then given by

$$T_{fi} = \langle\phi_\nu; \phi_{\nu'}|\hat{T}|\phi_B; \phi_{B'}\rangle,\qquad \text{(C.31)}$$

Using the Feynman rules again we get:

$$\mathcal{M}\left(\phi_\nu; \phi_\nu \to \phi_\nu; \phi_\nu\right) = -\frac{G_F^2}{2}\frac{m_\nu}{E_\nu}T\sum_{\omega_0(even)}T\sum_{\omega_{B_2}(odd)}\int\frac{d^3\vec{q}}{(2\pi)^3}\int\frac{d^3\vec{p}_{B_2}}{(2\pi)^3}\qquad \text{(C.32)}$$

$$\sum_{s_\nu}\left\{[\bar{u}_{s_\nu}(i\omega_\nu, \vec{p}_\nu)]_\gamma[\gamma_\mu(1 - \gamma^5)]_{\gamma\delta}\left[S^l(i\omega_l, \vec{p}_l)\right]_{\delta\epsilon}[\gamma_\lambda(1 - \gamma^5)]_{\epsilon\eta}[u_{s_\nu}(i\omega_\nu, \vec{p}_\nu)]_\eta\right\}$$

$$\left\{[\gamma^\mu(V - A\gamma^5)]_{\alpha'\alpha}[S^{B_4}(i\omega_{B_4}, \vec{p}_{B_4})]_{\alpha\beta}[\gamma^\lambda(V - A\gamma^5)]_{\beta\beta'}[S^{B_2}(i\omega_{B_2}, \vec{p}_{B_2})]_{\beta'\alpha'}\right\}$$

$$= -\frac{G_F^2}{4}\frac{1}{E_\nu}T\sum_{\omega_0(even)}T\sum_{\omega_{B_2}(odd)}\int\frac{d^3\vec{q}}{(2\pi)^3}\int\frac{d^3\vec{p}_{B_2}}{(2\pi)^3}L_{\mu\lambda}W^{\mu\lambda},\qquad \text{(C.33)}$$

with the polarization function:

$$\tilde{\Pi}(iq_0, \vec{q}) = T\sum_{\omega_B(odd)}\int\frac{d^3\vec{p}_B}{(2\pi)^3}\text{Tr}\left[S^B(i\omega_B, \vec{p}_B)S^{B'}(i\omega_{B'}, \vec{p}_{B'})\right].\qquad \text{(C.34)}$$

The differential cross section is than defined as

$$\frac{1}{\Omega}\frac{d^3\sigma(E_\nu)}{d\Omega^2 dq_0} = \frac{G_F^2}{8\pi^3}E_l^2\left(1 - f_l(E_l)\left[(1 + \cos\theta)S_V^{nc}(q_0, q) + (3 - \cos\theta)S_A^{nc}(q_0, q)\right]\right.$$
$$\text{(C.35)}$$

C.3   Structure function in the Hartree-Fock approximation

In the Hartree-Fock approximation the baryonic propagator S^b is

$$\left[S^b(\imath\omega_b, \vec{p})\right]_{\alpha\beta} = \frac{\delta_{\alpha\beta}}{\imath\omega_n + \mu - E_b(p)} \,, \qquad (\text{C.36})$$

where the energy is

$$E_b(p) = M_b + \frac{p^2}{2M_b^*} + \tilde{U}_b \,. \qquad (\text{C.37})$$

As noted in Sec. 2.2 this is the quadratic approximation for the single-particle spectrum. Thus, we have the polarization function for two different nonrelativistic interacting baryons:

$$\tilde{\Pi}^0(iq_0, \vec{q}) = T \sum_{\omega_{B_2}(odd)} \int \frac{d^3\vec{p}_{B_2}}{(2\pi)^3} 2 \left[\frac{1}{\imath\omega_{B_2} + \mu_{B_2} - E_{B_2}(p_{B_2})} \frac{1}{\imath\omega_{B_4} + \mu_{B_4} - E_{B_4}(p_{B_4})} \right] \,,$$
$$(\text{C.38})$$

which we now label with a zero since this is the zeroth-order Lindhard function [33].

The connection established earlier with the structure function Eq. (C.28) gives us

$$S^0(q_0, q) = \frac{1}{2\pi^2} \int d^3p_2 \delta(q_0 + E_2 - E_4) f_2(E_2)(1 - f_4(E_4)) \,. \qquad (\text{C.39})$$

where $E_4 = M_4 + (\vec{p}_2 + \vec{q})^2 / 2M_4^* + U_4$.

We rewrite the energy delta function in terms of the angle between $\vec{p}_2$ and $\vec{q}$ as:

$$\delta(q_0 + E_2 - E_4) = \frac{M_4^*}{p_2 q} \delta(\cos\theta - \cos\theta_0)\Theta(E_2 - e_-)\Theta(e_+ - E_2) \,, \qquad (\text{C.40})$$

where

$$\cos\theta_0 = \frac{M_4^*}{p_2 q}\left(c - \frac{\chi p_2^2}{2M_4^*}\right) \,,\ p_\pm^2 = \frac{2q^2}{\chi^2}\left[\left(1 + \frac{\chi M_4^* c}{q^2}\right) \pm \sqrt{1 + \frac{2\chi M_4^* c}{q^2}}\right] \,, \quad (\text{C.41})$$

$$e_\pm = \frac{p_\pm^2}{2M_2^*}; \ \frac{(\vec{p}_2 + \vec{q})^2}{2M_4^*} = \frac{p_2^2}{2M_2^*} + q_0 + M_2 - M_4 + U_2 - U_4 \,, \quad (\text{C.42})$$

with

$$\chi = 1 - \frac{M_4^*}{M_2^*}; \qquad c = q_0 + M_2 - M_4 + U_2 - U_4 - \frac{q^2}{2M_4^*}. \qquad (C.43)$$

The factors $M_2 - M_4$ and $U_2 - U_4$ are the conversion energy gained due to the difference in mass and potential. Substituting these results into Eq.(C.39) and performing the angular integrals we obtain

$$S^0(q_0, q) = \frac{M_4^*}{\pi q} \int p_2 dp_2 f_2(E_2)(1 - f_4(E_4)). \qquad (C.44)$$

With the substitution $E_2 = M_2 + \frac{p_2^2}{2M_2^*} + U_2$ we get

$$S^0(q_0, q) = \frac{M_2^* M_4^*}{\pi q} \int_{e_-}^{e_+} dE_2 f(E_2)(1 - f(E_2 + q_0)) \qquad (C.45)$$

$$= \frac{M_2^* M_4^*}{\pi q} \int_{e_-}^{e_+} dE_2 \frac{1}{1 + \exp\left(\frac{E_2 - \mu_2}{T}\right)} \frac{\exp\left(\frac{E_2 + q_0 - \mu_4}{T}\right)}{1 + \exp\left(\frac{E_2 + q_0 - \mu_4}{T}\right)}. \qquad (C.46)$$

By using

$$\int \frac{dx}{1 + \exp(x)} \frac{1}{1 + \exp(-x - z)} = -\frac{1}{1 - \exp(-z)} \ln\frac{1 + \exp(x)}{1 + \exp(x + z)}, \qquad (C.47)$$

we have

$$S(q_0, q) = \frac{M_2^* M_4^* T}{\pi q} \frac{\xi_- - \xi_+}{1 - \exp(-z)}, \qquad (C.48)$$

where

$$z = \frac{q_0 + \mu_2 - \mu_4}{T}, \qquad (C.49)$$

$$\xi_\pm = \ln\left[\frac{1 + \exp\frac{e_\pm - \mu_2 + M_2 + U_2}{T}}{1 + \exp\frac{e_\pm + q_0 - \mu_4 + M_2 + U_2}{T}}\right]. \qquad (C.50)$$

The most general case, which we have presented so far, will also apply to the case of a charged current. For neutral currents, since the initial and final state particles are identical for both leptons and baryons, we have the simplifications

$$M_2 = M_4, \ \mu_2 = \mu_4, \ M_2^* = M_4^*, \ U_2 = U_4, \qquad (C.51)$$

$$z = \frac{q_0}{T}, \qquad e_- = \frac{M_2^*}{2q^2}\left(q_0 - \frac{q^2}{2M_2^*}\right)^2, \qquad e_+ = \infty. \qquad (C.52)$$

Thus, $\xi_+ = -z$, and one finds the following result for the neutral current structure function:

$$S^0(q_0, q) = \frac{M_2^{*2}T}{\pi q}\left[\frac{z}{1-\exp(-z)}\left(1+\frac{\xi_-}{z}\right)\right].\qquad(\text{C}.53)$$

For the case of a free gas all one has to do is to replace all effective masses with bare masses and take all single-particle potentials to be equal to zero.

C.4   Structure functions in the RPA

If we consider the full form of the baryonic neutral current in the presence of both nucleons and hyperons we can write it in the following way [1]

$$J_n^\mu = \sum_{f=p,n,\Lambda,\Sigma^-,...}\bar{f}\gamma_\mu(g_V^{ff}-c_A^{ff})f + \bar{\Lambda}\gamma_\mu(g_V^{\Lambda\Sigma^0}-c_A^{\Lambda\Sigma^0})\Sigma^0.\qquad(\text{C}.54)$$

From this form of the current it is obvious that we need to expand our notation to include the isospin indices. This in combination with the aim to study the influence of matter on the polarization functions of the RPA leads to the introduction of the full polarization matrix, $\tilde{\Pi}_{\lambda\mu;\alpha\beta}(q_0, \vec{q})$. Additionally at this point we relax our restriction to spin unpolarized matter and consider also the spin indices. In general the full polarization function is given by [33]:

$$\tilde{\Pi}_{\lambda\mu;\alpha\beta}(q_0,\vec{q}) = \tilde{\Pi}^0_{\lambda\mu;\alpha\beta}(q_0,\vec{q}) + \sum_{\eta\nu\rho\sigma}\tilde{\Pi}^0_{\lambda\mu;\rho\nu}(q_0,\vec{q})K_{\rho\nu;\eta\sigma}(q_0,\vec{q})\tilde{\Pi}_{\eta\sigma;\alpha\beta}(q_0,\vec{q}).\qquad(\text{C}.55)$$

The indices here should not be confused with Lorentz indices of the γ-matrices since these indices are from the spin and flavor space. Schematically this can be represented as in Fig. C.2.
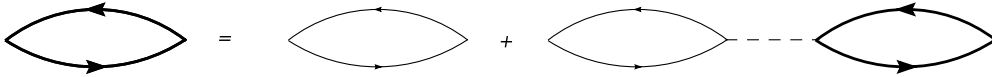

Figure C.2: Salpether equation in RPA.

The kernel K allows the calculation of polarization function to all orders. It is simple to see that in the lowest order case where there is no interaction, K would be zero and we would immediately recover the Hartree-Fock approximation. The first-order approximation is then:

$$K_{\rho\nu;\eta\sigma}(q_0,\vec{q}) = -\langle\rho\,\sigma\mid V\mid\eta\,\nu\rangle + \langle\sigma\,\rho\mid V\mid\eta\,\nu\rangle,\qquad(\text{C}.56)$$

---

[1]The weak neutral current has no strangeness changing components.

which is exactly the RPA approximation.

The zeroth-order polarization function Π^0 is diagonal so we can write:

$$\tilde{\Pi}^0_{\lambda\mu;\alpha\beta}(q_0, \vec{q}) = \delta_{\lambda\alpha}\delta_{\mu\beta}\tilde{\Pi}^0_{\lambda\mu}(q_0, \vec{q}) \,. \tag{C.57}$$

Note that there is no integral in equation Eq. (C.55) thus making the equation just a system of algebraic equations. Thus Eq. (C.55) becomes a matrix equation (further on we suppress $(q_0, \vec{q})$ but it is always implied):

$$\mathbf{\Pi} = \mathbf{\Pi^0} + \mathbf{\Pi^0 K \Pi} \,. \tag{C.58}$$

The solution of this matrix equation is then

$$\mathbf{\Pi} = (\mathbf{1} - \mathbf{\Pi^0 K})^{-1}\mathbf{\Pi^0} \,. \tag{C.59}$$

C.4.1   Single-particle case

Let us first consider the case of single component matter containing only particle i, where we have only the spin indices. In this case the $\mathbf{\Pi}^0$-matrix is a unit-matrix multiplied with the polarization function $\tilde{\Pi}^0$. As for the kernel $\mathbf{K}$ in spin space we can, with the aid of Eq. (4.25), write:

$$\mathbf{K}_{ii} = \begin{bmatrix} f_{ii} + g_{ii} & 0 & 0 & f_{ii} - g_{ii} \\ 0 & 2g_{ii} & 0 & 0 \\ 0 & 0 & 2g_{ii} & 0 \\ f_{ii} - g_{ii} & 0 & 0 & f_{ii} + g_{ii} \end{bmatrix} \,, \tag{C.60}$$

where the $(1,1)$ element of the matrix is $<\uparrow\uparrow |V| \uparrow\uparrow>$ and the $(4,4)$ element is $<\downarrow\downarrow |V| \downarrow\downarrow>$. The $\mathbf{K}$-matrix can be diagonalized and we get:

$$\mathbb{K}_{ii} = \begin{bmatrix} 2f_{ii} & 0 & 0 & 0 \\ 0 & 2g_{ii} & 0 & 0 \\ 0 & 0 & 2g_{ii} & 0 \\ 0 & 0 & 0 & 2g_{ii} \end{bmatrix} \,. \tag{C.61}$$

If we now use this in Eq. (C.59). Keeping in mind the unitary matrix used to diagonalize $\mathbf{K}$ we find

$$\tilde{\Pi}_{11_{ii}} = \tilde{\Pi}_{V_{ii}} = \frac{\tilde{\Pi}^0_{ii}}{1 - f_{ii}\tilde{\Pi}^0_{ii}} \tag{C.62}$$

$$\tilde{\Pi}_{22_{ii}} = \tilde{\Pi}_{33_{ii}} = \tilde{\Pi}_{44_{ii}} = \tilde{\Pi}_{A_{ii}} = \frac{\tilde{\Pi}^0_{ii}}{1 - g_{ii}\tilde{\Pi}^0_{ii}} \,. \tag{C.63}$$

The imaginary part of the polarization function is then

$$Im\tilde{\Pi}_{V_{ii}} = \frac{Im\tilde{\Pi}_{ii}^0}{(1 - f_{ii}Re\tilde{\Pi}_{ii}^0)^2 + (f_{ii}Im\tilde{\Pi}_{ii}^0)^2} \, . \tag{C.64}$$

If the denominator is larger than one then the medium's response is suppressed, while if it is smaller it is enhanced.

We note that we will always use the diagonalized version of the kernel, because that way the vector and axial part can be solved separately.

C.4.2   Neutral current case

For the case of the neutral current we can write the vector coupling constants as

$$(c_V^{NC})^\dagger = \left(\begin{array}{ccccccc} c_V^{pp} & c_V^{nn} & c_V^{\Lambda\Lambda} & c_V^{\Sigma^-\Sigma^-} & c_V^{\Sigma^0\Sigma^0} & c_V^{\Sigma^+\Sigma^+} & c_V^{\Lambda\Sigma^0} \end{array} \right) \, , \tag{C.65}$$

whose values can be found in Tab. 5.2. Then with the knowledge of the RPA polarization matrix from Eq. (C.55) we obtain the polarization function

$$\tilde{\Pi}_V^{NC} = (c_V^{NC})^\dagger \mathbf{\Pi}_V^{NC}(c_V^{NC}) \, . \tag{C.66}$$

For the calculation of the neutral current RPA polarization matrix $\mathbf{\Pi}_V^{NC}$ we need the zeroth order polarization matrix:

$$\mathbf{\Pi}_{NC}^0 = \begin{bmatrix} \tilde{\Pi}_{pp}^0 & 0 & 0 & 0 & 0 & 0 & 0 \\ 0 & \tilde{\Pi}_{nn}^0 & 0 & 0 & 0 & 0 & 0 \\ 0 & 0 & \tilde{\Pi}_{\Lambda\Lambda}^0 & 0 & 0 & 0 & 0 \\ 0 & 0 & 0 & \tilde{\Pi}_{\Sigma^-\Sigma^-}^0 & 0 & 0 & 0 \\ 0 & 0 & 0 & 0 & \tilde{\Pi}_{\Sigma^0\Sigma^0}^0 & 0 & 0 \\ 0 & 0 & 0 & 0 & 0 & \tilde{\Pi}_{\Sigma^+\Sigma^+}^0 & 0 \\ 0 & 0 & 0 & 0 & 0 & 0 & \tilde{\Pi}_{\Lambda\Sigma^0}^0 \end{bmatrix} \, , \tag{C.67}$$

and the appropriate kernel:

$$\mathbb{K}_{NC}^V = \begin{bmatrix} f_{pp} & f_{pn} & f_{p\Lambda} & f_{p\Sigma^-} & f_{p\Sigma^0} & f_{p\Sigma^+} & f_{pp\Lambda\Sigma^0} \\ f_{pn} & f_{nn} & f_{n\Lambda} & f_{n\Sigma^-} & f_{n\Sigma^0} & f_{n\Sigma^+} & f_{nn\Lambda\Sigma^0} \\ f_{p\Lambda} & f_{n\Lambda} & 0 & 0 & 0 & 0 & 0 \\ f_{p\Sigma^-} & f_{n\Sigma^-} & 0 & 0 & 0 & 0 & 0 \\ f_{p\Sigma^0} & f_{n\Sigma^0} & 0 & 0 & 0 & 0 & 0 \\ f_{p\Sigma^+} & f_{n\Sigma^+} & 0 & 0 & 0 & 0 & 0 \\ f_{pp\Lambda\Sigma^0} & f_{nn\Lambda\Sigma^0} & 0 & 0 & 0 & 0 & 0 \end{bmatrix} \, . \tag{C.68}$$

From this point on the calculation is straightforward matrix multiplication. Thus, and because of its size and complexity, we do not show the complete polarization

function $\tilde{\Pi}_V^{NC}$ or any of the matrix elements of $\mathbf{\Pi}_V^{NC}$. However for the sake of illustration and comparison we show this for the case of matter composed only of nucleons. In this case the matrix elements of the polarization function are:

$$\tilde{\Pi}_{V_{pp}} = \tilde{\Pi}_{pp}^0 \left(1 - f_{nn}\tilde{\Pi}_{nn}^0 \right) / D_{NC}^V \,, \tag{C.69}$$

$$\tilde{\Pi}_{V_{pn}} = f_{pn}\tilde{\Pi}_{nn}^0 \tilde{\Pi}_{pp}^0 / D_{NC}^V \,, \tag{C.70}$$

$$\tilde{\Pi}_{V_{nn}} = \tilde{\Pi}_{nn}^0 \left(1 - f_{pp}\tilde{\Pi}_{pp}^0 \right) / D_{NC}^V \,, \tag{C.71}$$

where

$$D_{NC}^V = 1 - \tilde{\Pi}_{pp}^0 f_{pp} - \tilde{\Pi}_{nn}^0 f_{nn} + \tilde{\Pi}_{pp}^0 \tilde{\Pi}_{nn}^0 \left(f_{nn}f_{pp} - f_{pn}^2 \right) \,, \tag{C.72}$$

which when combined with the coupling constants gives the vector polarization function as:

$$\tilde{\Pi}_V^{NC} = \left[(c_{pp}^V)^2 \tilde{\Pi}_{pp}^0 \left(1 - f_{nn}\tilde{\Pi}_{nn}^0 \right) + 2c_{pp}^V c_{nn}^V f_{pn}\tilde{\Pi}_{nn}^0 \tilde{\Pi}_{pp}^0 \right.$$
$$\left. + (c_{nn}^V)^2 \tilde{\Pi}_{nn}^0 \left(1 - f_{pp}\tilde{\Pi}_{pp}^0 \right) \right] / D_{NC}^V \,, \tag{C.73}$$

which is identical to the result from [5].

The same result can be found for the axial polarization function if we replace the coupling constants and make the following substitution $f \to g$ in the kernel.

C.4.3 Charge current case

For the charged current we have the following coupling constants

$$(g_V)^\dagger = \left(\begin{array}{cccccccc} g_V^{pn} & g_V^{p\Lambda} & g_V^{n\Sigma^-} & g_V^{p\Sigma^0} & g_V^{\Lambda\Sigma^-} & g_V^{\Lambda\Sigma^+} & g_V^{\Sigma^-\Sigma^0} & g_V^{\Sigma^0\Sigma^+} \end{array} \right) \,, \tag{C.74}$$

whose values can be found in Tab. 5.1. However, due to the conservation laws some of the processes are forbidden such that the polarization matrix decouples into two parts. Thus we separate the coupling constants into two parts

$$(g_V')^\dagger = \left(\begin{array}{ccccc} g_V^{pn} & g_V^{\Lambda\Sigma^-} & g_V^{\Lambda\Sigma^+} & g_V^{\Sigma^-\Sigma^0} & g_V^{\Sigma^0\Sigma^+} \end{array} \right) \,, \tag{C.75}$$

$$(g_V'')^\dagger = \left(\begin{array}{ccc} g_V^{p\Lambda} & g_V^{n\Sigma^-} & g_V^{p\Sigma^0} \end{array} \right) \,. \tag{C.76}$$

The charged current RPA polarization function is then

$$\tilde{\Pi}_V^{CC} = (g_V')^\dagger \mathbf{\Pi}_{CC}^{V'}(g_V') + (g_V'')^\dagger \mathbf{\Pi}_{CC}^{V''}(g_V'') \,. \tag{C.77}$$

We now have to calculate two polarization matrices $\mathbf{\Pi}_{CC}^{V'}$ and $\mathbf{\Pi}_{CC}^{V''}$. We will also need two zero-order polarization matrices

$$\mathbf{\Pi}_{CC}^{0'} = \begin{bmatrix} \tilde{\Pi}_{pn}^0 & 0 & 0 & 0 & 0 \\ 0 & \tilde{\Pi}_{\Lambda\Sigma^-}^0 & 0 & 0 & 0 \\ 0 & 0 & \tilde{\Pi}_{\Sigma^+\Lambda}^0 & 0 & 0 \\ 0 & 0 & 0 & \tilde{\Pi}_{\Sigma^0\Sigma^-}^0 & 0 \\ 0 & 0 & 0 & 0 & \tilde{\Pi}_{\Sigma^+\Sigma^0}^0 \end{bmatrix}, \tag{C.78}$$

and

$$\mathbf{\Pi}_{CC}^{0''} = \begin{bmatrix} \tilde{\Pi}_{p\Lambda}^0 & 0 & 0 \\ 0 & \tilde{\Pi}_{n\Sigma^-}^0 & 0 \\ 0 & 0 & \tilde{\Pi}_{p\Sigma^0}^0 \end{bmatrix}. \tag{C.79}$$

Obviously two kernels are also required

$$\mathbb{K}_{CC}^{V'} = \begin{bmatrix} f_{pnpn} & f_{pn\Lambda\Sigma^-} & f_{pn\Sigma^+\Lambda} & f_{pn\Sigma^0\Sigma^-} & f_{pn\Sigma^+\Sigma^0} \\ f_{pn\Lambda\Sigma^-} & 0 & 0 & 0 & 0 \\ f_{pn\Sigma^+\Lambda} & 0 & 0 & 0 & 0 \\ f_{pn\Sigma^0\Sigma^-} & 0 & 0 & 0 & 0 \\ f_{pn\Sigma^+\Sigma^0} & 0 & 0 & 0 & 0 \end{bmatrix}, \tag{C.80}$$

and

$$\mathbb{K}_{CC}^{V''} = \begin{bmatrix} \tilde{K}_{p\Lambda p\Lambda}^V & \tilde{K}_{p\Lambda n\Sigma^-}^V & \tilde{K}_{p\Lambda p\Sigma^0}^V \\ \tilde{K}_{n\Sigma^- p\Lambda}^V & \tilde{K}_{n\Sigma^- n\Sigma^-}^V & \tilde{K}_{n\Sigma^- p\Sigma^0}^V \\ \tilde{K}_{p\Sigma^0 p\Lambda}^V & \tilde{K}_{p\Sigma^0 n\Sigma^-}^V & \tilde{K}_{p\Sigma^0 p\Sigma^0}^V \end{bmatrix}. \tag{C.81}$$

Here for the kernel elements we have adopted a similar notation as for the case of the Landau-Migdal parameters although we have used Eq. (C.56) to define them.

Bibliography

[1] H.-T. Janka, K. Langanke, A. Marek, G. Martinez-Pinedo, and B. Mueller, Phys. Rept. **442**, 38 (2007), `astro-ph/0612072`.

[2] A. Burrows and T. A. Thompson (2002), `astro-ph/0211404`.

[3] N. Iwamoto and C. J. Pethick, Phys. Rev. **D25**, 313 (1982).

[4] A. Burrows and R. F. Sawyer, Phys. Rev. **C59**, 510 (1999), `astro-ph/9804264`.

[5] S. Reddy, M. Prakash, J. M. Lattimer, and J. A. Pons, Phys. Rev. **C59**, 2888 (1999), `astro-ph/9811294`.

[6] H. Heiselberg and M. Hjorth-Jensen, Phys. Rept. **328**, 237 (2000), `nucl-th/9902033`.

[7] S. K. Bogner, T. T. S. Kuo, A. Schwenk, D. R. Entem, and R. Machleidt, Phys. Lett. **B576**, 265 (2003a), `nucl-th/0108041`.

[8] S. R. Beane et al. (NPLQCD), Nucl. Phys. **A794**, 62 (2007), `hep-lat/0612026`.

[9] S. K. Bogner, T. T. S. Kuo, and A. Schwenk, Phys. Rept. **386**, 1 (2003b), `nucl-th/0305035`.

[10] K. Suzuki and S. Y. Lee, Prog. Theor. Phys. **64**, 2091 (1980a).

[11] K. Suzuki and S. Y. Lee, Phys. Lett. **B91**, 173 (1980b).

[12] F. Andreozzi, Phys. Rev. **C54**, 684 (1996).

[13] B.-J. Schaefer, M. Wagner, J. Wambach, T. T. S. Kuo, and G. E. Brown, Phys. Rev. **C73**, 011001 (R) (2006).

[14] M. Wagner, B.-J. Schaefer, J. Wambach, T. T. S. Kuo, and G. E. Brown, Phys. Rev. **C74**, 054003 (2006).

[15] P. M. M. Maessen, T. A. Rijken, and J. J. de Swart, Phys. Rev. **C40**, 2226 (1989).

[16] T. A. Rijken, V. G. J. Stoks, and Y. Yamamoto, Phys. Rev. **C59**, 21 (1999).

[17] J. Haidenbauer and U.-G. Meißner, Phys. Rev. **C72**, 044005 (2005).

[18] B. Holzenkamp, K. Holinde, and J. Speth, Nucl. Phys. **A500**, 485 (1989).

[19] A. Reuber, K. Holinde, and J. Speth, Nucl. Phys. **A570**, 543 (1994).

[20] T. A. Rijken and Y. Yamamoto (2006a), `nucl-th/0608074`.

[21] T. A. Rijken and Y. Yamamoto, Phys. Rev. **C73**, 044008 (2006b), `nucl-th/0603042`.

[22] L. Micu, Nucl. Phys. **B10**, 521 (1969).

[23] P. F. Bedaque and U. van Kolck, Ann. Rev. Nucl. Part. Sci. **52**, 339 (2002), `nucl-th/0203055`.

[24] E. Epelbaum, Prog. Part. Nucl. Phys. **57**, 654 (2006), `nucl-th/0509032`.

[25] R. J. Furnstahl, G. Rupak, and T. Schaefer (2008), `arXiv:0801.0729 [nucl-th]`.

[26] S. Weinberg, Phys. Lett. **B251**, 288 (1990).

[27] S. Weinberg, Nucl. Phys. **B363**, 3 (1991).

[28] E. Epelbaum, W. Glöckle, and U.-G. Meißner, Nucl. Phys. **A747**, 362 (2005), `nucl-th/0405048`.

[29] H. Polinder, J. Haidenbauer, and U.-G. Meißner, Nucl. Phys. **A779**, 244 (2006).

[30] C. L. Korpa, A. E. L. Dieperink, and R. G. E. Timmermans, Phys. Rev. **C65**, 015208 (2002), `nucl-th/0109072`.

[31] J. Haidenbauer, U.-G. Meißner, A. Nogga, and H. Polinder, Lect. Notes Phys. **724**, 113 (2007), `nucl-th/0702015`.

[32] D. B. Kaplan, M. J. Savage, and M. B. Wise, Nucl. Phys. **B534**, 329 (1998).

[33] A. L. Fetter and J. D. Walecka, *Quantum Theory Of Many-particle Systems* (McGraw-Hill, Inc., 1971).

[34] H. Đapo, B.-J. Schaefer, and J. Wambach, Eur. Phys. J. **A36**, 101 (2008a), `0802.2646`.

[35] P. Saha et al., Phys. Rev. **C70**, 044613 (2004).

[36] H.-J. Schulze, M. Baldo, U. Lombardo, J. Cugon, and A. Lejeune, Phys. Rev. **C57**, 704 (1998).

[37] I. Vidana, A. Polls, A. Ramos, and H.-J. Schulze, Phys. Rev. **C64**, 044301 (2001).

[38] I. Vidana, I. Bombaci, A. Polls, and A. Ramos, Astron. Astrophys. **399**, 687 (2003).

[39] N. Kaiser and W. Weise, Phys. Rev. **C71**, 015203 (2005).

[40] H. Polinder, Ph.D. thesis, Nijmegen (2004).

[41] N. Kaiser, Phys. Rev. **C71**, 068201 (2005).

[42] M. Kohno, Y. Fujiwara, Y. Watanabe, K. Ogata, and M. Kawai, Phys. Rev. **C74**, 064613 (2006), `nucl-th/0611080`.

[43] H. Maekawa, K. Tsubakihara, and A. Ohnishi (2007), `nucl-th/0701066`.

[44] T. Nagae et al., Phys. Rev. Lett. **80**, 1605 (1998).

[45] F. Sammarruca (2008), `arXiv:0801.0879 [nucl-th]`.

[46] F. Coester, S. Cohen, B. Day, and C. M. Vincent, Phys. Rev. **C1**, 769 (1970).

[47] S. K. Bogner, A. Schwenk, R. J. Furnstahl, and A. Nogga, Nucl. Phys. **A763**, 59 (2005), `nucl-th/0504043`.

[48] A. Nogga, S. K. Bogner, and A. Schwenk, Phys. Rev. **C70**, 061002 (2004).

[49] A. Akmal, V. R. Pandharipande, and D. G. Ravenhall, Phys. Rev. **C58**, 1804 (1998), `nucl-th/9804027`.

[50] R. Roth, H. Hergert, P. Papakonstantinou, T. Neff, and H. Feldmeier, Phys. Rev. **C72**, 034002 (2005), `nucl-th/0505080`.

[51] S. L. Shapiro and S. Teukolsky, *Black Holes, White Dwarfs, and Neutron stars: The Physics of Compact Objects* (Wiley, New York, 1983).

[52] N. K. Glendenning, *Compact Stars* (Springer, New York, 1997).

[53] J. M. Lattimer and M. Prakash, Phys. Rept. **442**, 109 (2007), `astro-ph/0612440`.

[54] M. Prakash et al., Phys. Rept. **280**, 1 (1997), `nucl-th/9603042`.

[55] H. Đapo, B.-J. Schaefer, and J. Wambach (2008b), `0811.2939`.

[56] M. Baldo, G. F. Burgio, and H. J. Schulze, Phys. Rev. **C58**, 3688 (1998).

[57] J. R. Oppenheimer and G. M. Volkoff, Phys. Rev. **55**, 374 (1939).

[58] G. Baym, C. Pethick, and P. Sutherland, Astrophys. J. **170**, 299 (1971).

[59] J. W. Negele and D. Vautherin, Nucl. Phys. **A207**, 298 (1973).

[60] C. J. Pethick and D. G. Ravenhall, Ann. Rev. Nucl. Part. Sci. **45**, 429 (1995).

[61] P. Haensel, in *Physics of neutron star interiors*, edited by D. Blaschke, N. K. Glendenning, and A. Sedrakian (Springer-Verlag,Heidelberg, 2001), vol. 578 of *Lecture Notes in Physics*, p. 127.

[62] S. B. Ruester, M. Hempel, and J. Schaffner-Bielich, Phys. Rev. **C73**, 035804 (2006), `astro-ph/0509325`.

[63] J. M. Weisberg and J. H. Taylor (2004), `astro-ph/0407149`.

[64] I. Vidana, A. Polls, A. Ramos, L. Engvik, and M. Hjorth-Jensen, Phys. Rev. **C62**, 035801 (2000), `nucl-th/0004031`.

[65] J. Schaffner-Bielich, M. Hanauske, H. Stöcker, and W. Greiner, Phys. Rev. Lett. **89**, 171101 (2002).

[66] J. Schaffner-Bielich, S. Schramm, and H. Stöcker (2007), `0711.2639`.

[67] L. Mornas, Eur. Phys. J. **A24**, 293 (2005), `nucl-th/0407083`.

[68] M. Bender, J. Dobaczewski, J. Engel, and W. Nazarewicz, Phys. Rev. **C65**, 054322 (2002), `nucl-th/0112056`.

[69] O. Sjoberg, Nucl. Phys. **A265**, 511 (1976).

[70] A. B. Migdal, *Theory of Finite Fermi System and Aplication to Atomic Nuclei* (Inter-science, New York, 1962).

[71] K. Nakayama and W. G. Love, Phys. Rev. **C38**, 51 (1988).

[72] H. Đapo, Diploma thesis, Sarajevo (2004).

[73] H. Nakada, Phys. Rev. **C68**, 014316 (2003), `nucl-th/0304021`.

[74] S. Yamada and H. Toki, Phys. Rev. **C61**, 015803 (2000), `astro-ph/9907044`.

[75] E. D. Commings and P. H. Bucksbaum, *Weak interaction of leptons and quarks* (Cambridge University press, New York, 1983).

[76] M. Kobayashi and T. Maskawa, Prog. Theor. Phys. **49**, 652 (1973).

[77] S. Reddy, M. Prakash, and J. M. Lattimer, Phys. Rev. **D58**, 013009 (1998), `astro-ph/9710115`.

[78] J. M. Gaillard and G. Sauvage, Ann. Rev. Nucl. Part. Sci. **34**, 351 (1984).

[79] M. J. Savage and J. Walden, Phys. Rev. **D55**, 5376 (1997), `hep-ph/9611210`.

[80] K. Strobel, C. Schaab, and M. K. Weigel, Astron. Astrophys. **350**, 497 (1999), `astro-ph/9908132`.

[81] J. J. Sakurai, *Modern Quantum Mechanics* (Addison-Wesley, 1985).

[82] M. I. Haftel and F. Tabakin, Nuclear Physics A **158**, 1 (1970).

[83] B. H. Bransden, C. J. Noble, and R. N. Hewitt, Journal of Physics B Atomic Molecular Physics **26**, 2487 (1993).

[84] W. H. Dickhoff and D. Van Neck, *Many-Body Theory Exposed* (World Scientific, Singapore, 2005).

[85] K. L. G. Heyde, *The Nuclear Shell Model* (Springer-Verlag, 1994).

Acknowledgments

Curriculum Vitae

Personal data:

Name:	Haris Đapo
Date of birth:	14. July. 1979
Place of Birth:	Trebinje, Bosnia and Hercegovina
Citizenship:	Bosnian and Hercegovinan
Parents:	Mujo Đapo
	Senija Đapo, b.Jusufović
Marital status:	single

Education

09/1994-06/1998	Attended high school: "Druga Gimnazija, Sarajevo, B&H"
06/1998	Grade point average: 4.7 (high:5, low:1)
10/1998-10/2002	Undergraduate study in Physics at University of Sarajevo, B&H
10/1998-02/2004	Grade point average: 8.9 (high:10, low:5)
01/2003-09/2003	Diploma thesis work at TU Darmstadt, Germany *"Neutrino mean free paths in proto neutron stars"*
01/2004	Graduation, Sarajevo, Grade:10
01/2004-06/2004	Military service
08/2004-present	Graduate study in Physics at TU Darmstadt, Germany